Application of Laser-based Diagnostics to a Prototype Gas Turbine Burner at Selected Pressures

Whiddon, Ronald

2014

Application of Laser-based Diagnostics to a Prototype Gas Turbine Burner at Selected Pressures

Ronald Whiddon

Academic thesis, which by due permission of the Faculty of Engineering at Lund University, will be publicly defended on Wednesday, May 7, 2014 at 10:15 a.m. in the lecture hall Sal A, Department of Physics, Professorgatan 1, Lund, for the degree of Doctor of Philosophy in Engineering.

Faculty Opponent: Professor Frédérik Grisch, CORIA, INSA de Rouen, Université de Rouen, France

Organization LUND UNIVERSITY	Document name DOCTORAL DISSERTATION
Faculty of Engineering Department of Physics	Date of issue April 2014
Division of Combustion Physics	
Author(s) Ronald Whiddon	Sponsoring organization

Title and subtitle

Application of Laser-based Diagnostics to a Prototype Gas Turbine Burner at Selected Pressures

Abstract

The matured laser-diagnostic techniques of planar laser-induced fluorescence (PLIF) and particle image velocimetry (PIV) were applied to a prototype gas turbine burner operating on various fuels. The work was performed to provide verification of computational fluid dynamic (CFD) models of the combustion of atypical fuels in a gas turbine combustor. The burner was operated using methane and three synthesized fuels of interest- one with hydrogen as the principle component and two with a low heating value (15 MJ/m^3). Experiments were performed at pressures from 1 to 9 bar, with the fuel/air mixture at both ambient (~ 300 K) and elevated temperature.

The burner, which was supplied by Siemens Industrial Turbomachinery, is a down-scaled prototype of that used in the SGT-750 gas turbine. It is composed of three individual sectors that are arranged concentrically, a centermost pilot sector, intermediate sector and main sector. Each sector contributes a premixed fuel/air flow, while swirl elements in each sector promote flame stabilization and recirculation in the combustion region. There are dedicated fuel feeds allowing for localized setting of fuel/air mixture at each of the sectors. The central pilot sector of the burner was separable from the full burner assembly and was examined in detail.

Information was generated regarding the use of syngas to fuel the burner. This information is intended to be used for the validation of CFD models of the experiments, including optimization of reduced chemical kinetic mechanisms for the specific fuels. Laminar flame speed measurements were made for several syngas fuel candidates from which the high-hydrogen syngas fuel was selected. Burner performance at the lean stability limit was examined using the fuels of interest. It was found that increasing the fuel/air ratio in the central pilot sector improved the lean limit onset of flame extinction up to the point that the central pilot extinguished. Optimization of the burner nitrogen oxides (NO$_x$) emission by fuel partitioning among the three sectors was performed. The response in emission level with fuel/air ratio was not universal among the fuels tested.

The largest portion of work in this thesis is the visualization of the burner combustion field by laser diagnostic methods. The flame shape was imaged by the PLIF of the OH radical distribution. PLIF imaging of the central pilot sector was recorded for atmospheric and elevated pressure for iterations of inlet air temperature, fuel type and equivalence ratio. When comparing the OH-LIF distribution for various fuels and pressures it was found that equivalence ratio had the greatest effect on the distribution of OH signal from the exit of the central pilot sector. Lean equivalence ratios showed a diffuse signal typical of the post combustion region. Near stoichiometric equivalence ratios yielded a distribution having a clearly defined inner edge indicating combustion occuring outside of the pilot sector. At rich equivalence ratios the OH signal was lifted away from the pilot burner exit. Comparison of OH-PLIF and chemiluminescence signal for methane combustion supported the characterization that the pilot sector efflux varied from post combustion to attached and then lifted flame in conjunction with the increase in equivalence ratio from lean to rich. OH-PLIF imaging was collected for staging of fuel to all three sectors of the burner at atmospheric pressure. The flow field in the combustion region produced by the full burner was visualized using PIV for each of fuels of interest, illustrating the recirculation zone. Finally the OH-LIF distribution was imaged for the combustion region of the entire burner at elevated pressure during operation at a single equivalence ratio with various dilutions of natural gas. There was little discernible change in flame shape as the pressure was changed from 3, 4.5 and 6 bar and energy content was changed from 30, 40 and 45 MJ/m^3 Wobbe index.

Key words

Combustion, Gas Turbine, NOx, DLE, Syngas, Elevated Pressure, Laser Diagnostics, OH, PIV, PLIF, Pilot, SGT-750

Classification system and/or index terms (if any)

Supplementary bibliographical information		Language English
-		

Distribution by (name and address)
Ronald Whiddon, Division of Combustion Physics, Department of Physics, Lund University, Box 118, 22100 Lund, Sweden
I, the undersigned, being the copyright owner of the abstract of the above-mentioned dissertation, hereby grant to all reference sources permission to publish and disseminate the abstract of the above-mentioned dissertation.

Signature _Ronald Whiddon_   Date ___2014-04-01___

Application of Laser-based Diagnostics to a Prototype Gas Turbine Burner at Selected Pressures

DOCTORAL THESIS

Ronald Whiddon

Division of Combustion Physics

Department of Physics

LUND 2014

LUND
UNIVERSITY

Ronald Whiddon
Division of Combustion Physics
Department of Physics
Lund University
P.O. Box 118
SE-221 00, Lund, Sweden

Now don't try to kid me, mancub
I made a deal with you
What I desire is man's red fire
To make my dream come true
Give me the secret, mancub
Clue me what to do
Give me the power of man's red flower
So I can be like you
I Wanna Be Like You (The Monkey Song), 1967

Popular Summary

There is a natural tendency to take advantage of the most convenient energy source available. In this usage, convenient may mean most abundant, easiest to harvest or simplest to handle. Convenient will also correspond to cheapest in many instances. However, some consider it a responsibility to think of the long term costs of the energy we use. No form of energy is free from environmental impact. The question is, are we getting enough value from the energy we use and are we properly evaluating the secondary penalties we pay for that energy?

Combustion is universally linked to human cultural development. For the last one hundred and fifty years coal, natural gas and liquid petroleum products-the big three fossil fuels, have been the power behind progress. These fuels are burned for heating, transportation and to generate electricity; they function quite well in the intended role. But not all energy sources are equal. For instance, coal which is cheap and abundant, is considerably dirtier when burnt than natural gas.

Together with the ideal combustion products which are water, CO_2 and energy, combustion produces unintended pollutants. Some of these are resultant from a presence in the fuel, such as heavy metals or sulphur compounds in coal and oil. Other pollutants are formed by the process of high temperature combustion, specifically nitrogen oxides (NO_x), or by incomplete combustion such as carbon monoxide and soot. Research into reduction of these pollutants has progressed for several decades. Attention is increasingly directed to the importance of the combustion product CO_2, as there is concern that elevating CO_2 levels in the atmosphere will affect the environment adversely. In response, there is a drive to find reduced impact and CO_2 neutral alternatives to the energy sources that permit the current standard of living.

It would be impossible to completely replace combustion based energy conversion in the short term, and so efforts are underway to create cleaner, more efficient combustion systems. A good example is the area of gas turbine engines for electrical generation. Companies like Siemens, General Electric, Alstom and others have met the increasingly strict regulation of pollutive emissions. New design strategies that ensure better blending of fuel and air, and operation at lower combustion temperatures are developing. Simultaneously, there is interest in learning to operate these cleaner burning engines on fuels other than natural gas, e.g, carbon neutral fuels synthesized from biomass, coal gasification and low energy content gases.

How are laser diagnostics involved in this development cycle? New ideas in

burner designs are being combined with alternative fuels that may not burn in the exactly the same way as natural gas. To understand how these interact it is useful to measure various aspects of the flame. Some laser-based measurements are aimed at recording a value, such as an amount of soot, the concentration of a certain chemical at a point in the flame, or a temperature. Laser-based techniques can measure these values without interfering with the local flame conditions as could a conventional probe. As a result, the measured value should be more representative of the true conditions. Laser-based techniques also enable measurements in harsh environments that are incompatible with direct sampling. One of the more useful applications of lasers in combustion research is for taking images.

Combustion in an engine is turbulent featuring a constant fluctuation of the flame edge. An image from a traditional camera will show the edge of the flame blurred by the amount of time that the camera was collecting emission, and the range of depths in the flame. If a two dimensional sheet of laser light of a selected wavelength passes through the flame, chemicals in the flame can give off photons, known as fluorescence. The image of this laser-induced fluorescence shows a slice through the flame frozen in time with no blurring. Depending on how these images are formed, certain qualities of the flame may be found: where the combustion reaction occurs, how quickly the flame edge fluctuates, how well the fuel mixes with the air before burning and so on.

The greater strength of laser-induced fluorescence imaging is realized when it is combined with computer modeling of the combustion process. By comparing the real images of the combustion region with the computer model predictions, the quality of the model can be verified and improved as needed. These more accurate models may then influence the design of next generation combustion machinery. It is for this reason that the thesis work was undertaken: to generate a set of data for a prototype burner operating at defined conditions while burning several fuels that typify renewable or reduced carbon deficit fuels. The burner was operated at several pressures from atmospheric pressure up to nine atmospheres. The result is a wealth of data describing the flame shape as characterized by laser-induced fluorescence, information regarding fuel combustion properties, burner temperatures and emissions data for documented operating conditions.

Abstract

The matured laser-diagnostic techniques of planar laser-induced fluorescence (PLIF) and particle image velocimetry (PIV) were applied to a prototype gas turbine burner operating on various fuels. The work was performed to provide verification of computational fluid dynamic (CFD) models of the combustion of atypical fuels in a gas turbine combustor. The burner was operated using methane and three synthesized fuels of interest- one with hydrogen as the principle component and two with a low heating value (15 MJ/m^3). Experiments were performed at pressures from 1 to 9 bar, with the fuel/air mixture at both ambient ($\approx$ 300 K) and elevated temperature.

The burner, which was supplied by Siemens Industrial Turbomachinery, is a down-scaled prototype of that used in the SGT-750 gas turbine. It is composed of three individual sectors that are arranged concentrically, a centermost pilot sector, intermediate sector and main sector. Each sector contributes a premixed fuel/air flow, while swirl elements in each sector promote flame stabilization and recirculation in the combustion region. There are dedicated fuel feeds allowing for localized setting of fuel/air mixture at each of the sectors. The central pilot sector of the burner was separable from the full burner assembly and was examined in detail.

Information was generated regarding the use of syngas to fuel the burner. This information is intended to be used for the validation of CFD models of the experiments, including optimization of reduced chemical kinetic mechanisms for the specific fuels. Laminar flame speed measurements were made for several syngas fuel candidates from which the high-hydrogen syngas fuel was selected. Burner performance at the lean stability limit was examined using the fuels of interest. It was found that increasing the fuel/air ratio in the central pilot sector improved the lean limit onset of flame extinction up to the point that the central pilot extinguished. Optimization of the burner nitrogen oxides (NO$_x$) emission by fuel partitioning among the three sectors was performed. The response in emission level with fuel/air ratio was not universal among the fuels tested.

The largest portion of work in this thesis is the visualization of the burner combustion field by laser diagnostic methods. The flame shape was imaged by the PLIF OH radical distribution. PLIF imaging of the central pilot sector was recorded for atmospheric and elevated pressure for iterations of inlet air temperature, fuel type and equivalence ratio. When comparing the OH-LIF distribution for various fuels and pressures it was found that equivalence ratio had the greatest effect on the distribution of OH signal from the exit of the

central pilot sector. Lean equivalence ratios showed a diffuse signal typical of the post combustion region. Near stoichiometric equivalence ratios yielded a distribution having a clearly defined inner edge indicating combustion occuring outside of the pilot sector. At rich equivalence ratios the OH signal was lifted away from the pilot burner exit. Comparison of OH-PLIF and chemiluminescence signal for methane combustion supported the characterization that the pilot sector efflux varied from post combustion to attached and then lifted flame in conjunction with the increase in equivalence ratio from lean to rich. OH-PLIF imaging was collected for staging of fuel to all three sectors of the burner at atmospheric pressure. The flow field in the combustion region produced by the full burner was visualized using PIV for each of fuels of interest, illustrating the recirculation zone. Finally the OH-LIF distribution was imaged for the combustion region of the entire burner at elevated pressure during operation at a single equivalence ratio with various dilutions of natural gas. There was little discernible change in flame shape as the pressure was changed from 3, 4.5 and 6 bar and energy content was changed from 30, 40 and 45 MJ/m^3 Wobbe index.

List of Papers

I Whiddon, R., Sigfrid, I. R., Collin, R. and Klingmann, J. "Investigation of a Premixed Gas Turbine Central Body Burner using OH Planar Laser Induced Fluorescence at Elevated Pressures",
In Proceedings of the ASME Turbo Expo 2013, Vol. 1A: Combustion, Fuels and Emissions, Parts A and B GT2013-94443

II Sigfrid, I. R., Whiddon, R., Aldén, M. and Klingmann, J. "Experimental Investigation of Lean Stability of a Prototype Syngas Burner for Low Calorific Value Gases",
In Proceedings of the ASME Turbo Expo 2011, Vol. 2: Combustion, Fuels and Emissions, Parts A and B GT2011-45694

III Sigfrid, I. R., Whiddon, R., Aldén, M. and Klingmann, J. "Parametric Study of Emissions from Low Calorific Syngas Combustion, with Variation of Fuel Distribution, in a Prototype Three Sector Burner",
In Proceedings of the ASME Turbo Expo 2011, Vol. 2: Combustion, Fuels and Emissions, Parts A and B GT2011-45689

IV Sigfrid, I. R., Whiddon, R., Collin, R., Klingmann, J. "Experimental Investigation of Laminar Flame Speeds for Medium Calorific Gas with Various amounts of Hydrogen and Carbon Monoxide Content at Gas Turbine Temperatures",
In Proceedings of the ASME Turbo Expo 2010, Vol. 2: Combustion, Fuels and Emissions, Parts A and B GT2010-22275

V Whiddon, R., Zhou, B. Borggren, J. and Li, Z. S. "Trimethylindium as an Indium Source for Combustion Experiments"
manuscript in preparation

VI Whiddon, R., Kundu, A., Subash, A. A., Collin, R., Aldén, M. and Klingmann, J. "Laser-induced Fluorescence Imaging of Gas Turbine Pilot Burner Combustion with Variation of Equivalence Ratio, Residence Time and Cooling Flow Temperature."
manuscript in preparation

Other Publications

A Sigfrid, I. R., Whiddon, R., Abou-Taouk, A., Collin, R. and Klingmann, J. "Experimental Investigation of an Industrial Lean Premixed Gas Turbine

Combustor with High Swirling Flow."
In Proceedings ASME Gas Turbine India Conference GTINDIA2012-9681

B Abou-Taouk, A., Sigfrid, I., Whiddon, R., Eriksson, L-E. "Four-step Global Reaction Mechanism for CFD Simulations of Flexi-fuel Burner for Gas Turbines"
In Proceedings of The International Symposium on Turbulence, Heat and Mass Transfer 2012 , Vol. 7

C Sigfrid, I. R., Whiddon, R., Collin, R. and Klingmann, J. "Experimental and Reactor Network Study of Nitrogen Dilution Effects on NOx Formation for Natural Gas and Syngas at Elevated Pressures"
In Proceedings of the ASME Turbo Expo 2013, Vol. 1A, Combustion, Fuels and Emissions GT2013-94355

D Sigfrid, I. R., Whiddon, R., Collin, R., Klingmann, J. "Influence of Reactive Species on the Lean Blowout Limit of an Industrial DLE Gas Turbine Burner"
2013 *Combustion and Flame* **161** (5), 1365–1373

E He, Y., Wang, Z., Yang, L., Whiddon, R. Li, Z. S., Zhou, J. and Cen, K. "Investigation of Laminar Flame Speeds of Typical Syngas using Laser Bunsen Method and Kinetic Simulation"
2012, *Fuel* **95** , 206-213

F Wang, Z.„ Chen, Y., Zhou, C., Whiddon, R., Zhang, Y., Zhou, J. and Cen, K. "Decomposition of Hydrogen Iodide via Wood-based Activated Carbon Catalysts for Hydrogen Production" 2011 *Int. J. of Hydrogen Energy.* **36** (1) 216-223

Nomenclature

E	photon energy
ν	frequency
h	Plank constant
λ	wavelength
c	vacuum velocity of light
v	vibrational level
$\bar{\omega}_e$	equilibrium oscillator frequency
χ_e	anharmonicity constant
B	rotational constant
J	rotational sub-level
b	excitation efficiency
N	number density of a state
B_{12}	stimulated excitation coefficient
$I(\nu)$	excitation intensity
g	absorption profile
C	instrument collection efficiency
V_l	laser probe volume
A_{21}	spontaneous emission coefficient
Q	non-emission relaxation coefficient
F	fluorescence intensity
P	dissociation coefficient
ϵ	transition energy
k	Boltzmann constant
$sigma$	scattering coefficient
S	detected signal
n_s	analytical signal
n_B	background signal
n_d	dark signal
W	Wobbe index
ϕ	equivalence ratio

Abbreviations

DLE	Dry Low Emission
LIF	Laser Induced Fluorescence
PLIF	Planar LIF

RET	Rotational Energy Transfer
VET	Vibrational Energy Transfer
IR	Infrared
UV	Ultraviolet
CFD	Computational Fluid Dynamics
PIV	Particle Image Velocimetry
CARS	Coherent Anti-Stokes Raman Scattering
KDP	potassium dihydrogen phosphate
CCD	Charge-Coupled Device
CMOS	Complementary Metal-Oxide Semiconductor
MCP	Multi-Channel Plate
LBO	Lean Blowout
ICCD	Intensified CCD

Contents

CONTENTS

List of Figures

INTRODUCTION

"[C]ulture develops when the amount of energy harnessed by man per capita per year is increased; or as the efficiency of the technological means of putting this energy to work is increased; or, as both factors are simultaneously increased."

Leslie White,
Energy and the Evolution of Culture [1]

There is little doubt that combustion has had, and will continue to have, a great influence in the development of human culture. Combustion is involved in more or less every aspect of life: heating, transportation, electricity generation and other applications. As of 2010, 88.8% of the global energy consumption centers around combustion, 80.6% of which is from fossil fuels [2].

Yet combustion is not without negative aspects as well. The polluting byproducts of combustion: soot, NO_x, SO_x, metals, and other components may represent immediate risks to human health and the environment. Naturally occurring financial incentives and strict regulation may provide the impetus for reduction of combustion byproducts; but, it is through better understanding of combustion, especially in practical applications, that solutions to the problems of combustion are developed.

Lately, the perceived climactic impact of elevated atmospheric CO_2 levels is leading to the restriction of production [3, 4]. Since combustion is a component of the human generated CO_2, its application will likely see controls as well. There is currently no comprehensive replacement for combustion based energy, but reducing some of the possible environmental impact of combustion systems can be accomplished by using CO_2 neutral fuels. This is also wise in light of the finite nature of fossil fuels and the possibility that substitute fuels may already be in abundance.

In this thesis, laser based diagnostics are used to aide research into the operation of a modern dry low emission (DLE) gas turbine burner on fossil fuel alternatives. The burner is a prototype that was designed for low NO_x emission while operating with approved fuels. The burner creates a premixed flame at lean equivalence ratio in order to reduce flame temperatures and the associated thermally generated NO_x. As premixed flames are sensitive to combustion instabilities [5] trying to operate the burner on a different fuel than designated fuel, e.g., natural gas, has the potential to induce instabilities.

In the experiments which form the basis of this thesis, the burner was operated on fuels that had various component blends and heating values. The burner per-

formance was evaluated for the fuels by establishing the lean stability limits and emission levels of CO and NO$_x$ for a variety of operating conditions. Then the combustion region was imaged using planar laser induced fluorescence (PLIF) for a number of configurations of the burner, equivalence ratios, pressures and fuels. The data generated from these experiments is useful for the validation of computation fluid dynamics models of the burner operation on these syngas fuels.

1.1   Thesis Organization

The thesis is organized into chapters in the following manner:

Chapter 1 Introduction.

Chapter 2 A review of light and matter interactions that make possible species specific optical diagnostics.

Chapter 3 Survey of diagnostic techniques central to the authors publications. This will include the basis of techniques, relevant instrumentation and data processing considerations.

Chapter 4 Mechanical description of a prototype industrial gas turbine burner and the fuels on which it was operated.

Chapter 5 Description of the atmospheric pressure test setup and findings from the experiments that were performed.

Chapter 6 Description of the elevated pressure test rig and the experiments that were performed.

Chapter 7 Summary of the work done and suggestions for future investigation.

Light and Matter

Spectroscopy is equally a function of the nature of light and of the construction of matter; these two subjects often overlap in content. In this chapter an overview of the electronic structure of atoms and molecules is presented as it is this nature that results in the processes of absorption and emission that make possible, various laser diagnostic techniques. More specific treatment of laser induced fluorescence (LIF), the dominant laser based diagnostic tool employed in this work, will be presented in chapter 3. If greater depth is desired, various textbooks can be referred to: for emphasis on the nature of light, *Light* by Ditchburn [6] and *Optical Physics* by Garbuny [7]; for the discussion of the foundations of atomic and molecular spectroscopy refer to Svanberg, Banwell and McCash, and Ekberth, [8–10].

2.1 Light

Light is collection of individual energy quanta- photons which are a force existing as an electromagnetic wave. The energy (E) of a photon is equated to the wave frequency (ν) times the Plank energy constant (h).

$$E = h\nu \tag{2.1}$$

Calculation of the wavelength(λ) is the division of the velocity of light in vacuum (c) by the frequency of fluctuation of the electromagnetic field.

$$\lambda = c/\nu \tag{2.2}$$

Note that the photon wavelength is dependent on the speed of light which is in turn dependent on the medium through which the photon travels. Consequently, the wavelength is not consistent, making it an ambiguous measurement of energy without also specifying the medium in which the light is found. As a general rule, wavelength is used when spatial phenomena such as grating orders are considered; frequency is used for applications where amount of energy is key, e.g., photofragmentation.

2.2 Atomic Spectroscopy

Atoms contain energy. A portion of this energy is contained as translational motion, a portion is held by the electrons which orbit the nucleus and a portion

is bound in the nucleus itself. The total energy of an atom can be increased by adding energy from an external source; depending on the amount of energy, different components of the atom are affected. Thermal energy addition increases the translational motion of the atom. Higher energy levels, including fast collisions or photons of visible and ultraviolet wavelength, deposit energy in the valence electrons, moving them to higher energy orbits or ionizing the atom.

Energy exchanges which involve electrons are analytically useful because only discrete energy values can be added to the electron, and these energy quanta are specific to the type of matter, due to the quantized nature of the electronic orbits. A quanta of energy exactly equal to the difference in the initial and final state electronic energy level can trigger an electron to change orbit. This energy gap is largely determined by the nucleus of the atom, so that even isotopes of the same atom show slightly shifted energy for the electronic orbitals. If a spectrum is made for the energy, i.e, photon frequencies, that are absorbed by a sample, it can be used to determine what elements are contained in that sample and in what concentration. Energy can also be released, allowing an electron that is excited to fall to a lower energy state. This is done through emission or collisional de-excitation.

Several electronic energy levels of an atom are shown in the left portion of figure 2.1. In the right portion of the figure, a general excitation and relaxation sequence is shown. First, energy equal to the difference between the third excited state and ground electronic states can be absorbed by the atom, a process called stimulated absorption. If a photon of equivalent energy to the gap between the upper and lower electronic levels interacts with an excited atom, it can induce relaxation of the excited electron to the lower level in a process that emits a photon- termed stimulated emission. There is also a likelihood that an electron occupying an upper energy level can fall back down to a lower energy level without external stimulation, this process labelled spontaneous emission. Each of the three transitions has an associated Einstein transition coefficient that describes the likelihood that an electron will undergo a transition. For the two stimulated processes the Einstein transition coefficient is the probability that an electron will successfully undergo a transition in the presence of an appropriate photon, while for spontaneous emission, it is the lifetime of the electron in the higher energy state. Additionally, the atom may collide with a second body resulting in energy being transferred to the colliding body, relaxing the excited electron to a lower energy state. This process is called collisional energy transfer.

2.3 Molecular Spectroscopy

The electronic energy levels of molecules are complicated by the presence of vibrational and rotational energy sub-levels associated with the electronic levels. This is shown in the energy diagram of a typical diatomic molecule, figure 2.2

The distance between the nuclei are not fixed but physically vibrate along the

axis defined by neighboring nuclei. This vibration affects the electronic orbits and consequently the energy level of those orbits. Possible vibrational energies are limited to discrete energy levels for a given electronic orbital. These energy intervals are described by the equation:

$$\epsilon_{vibration} = \bar{\omega}_e(\text{v} + 1/2) + \chi_e * \bar{\omega}_e(\text{v} + 1/2)^2 \qquad (2.3)$$

Where v is the vibrational level which has a positive integer value; all other constants are specific to the molecule: $\bar{\omega}_e$ the equilibrium oscillator frequency and χ_e the anharmonicity constant. The energy difference between vibrational levels is about three orders smaller than that between electronic energy levels.

Rotational energy sub-levels arise from the tendency of a molecule to rotate in space. This movement will effect the electronic orbit and thus the energy level that is sustained by that orbit. As in the electronic and vibrational levels, there are specific discrete rotational energy levels that are described by the equation:

$$\epsilon_{rotation} = \text{BJ}(\text{J} + 1) \qquad (2.4)$$

Where B is the rotational constant and J is the rotation sub-level which has a value greater than zero. The difference in energy between the rotational levels are approximately six orders of magnitude smaller than that between electronic states.

As both the vibrational and rotational distortions of the electronic energy level are present, the value of a specific electronic state for a molecule is the sum of the three discrete values. According to the Born-Oppenheimer approximation, each of these energy levels can be treated as independent contributions to the total energy level:

$$E_{total} = E_{electronic} + E_{vibration} + E_{rotation} \qquad (2.5)$$

The presence of the multitudinous energy sub-levels in the electron orbits creates some difference in the spectroscopic features of a molecule versus an atom. The abundance of closely coordinated energy levels increases the number of ways that energy can be collisionally redistributed. There are many more close lying energy levels that are absent from the atomic system whereby an electron can fall back to a lower energy state upon collision, either by the process of rotational energy transfer (RET) or vibrational energy transfer (VET). The frequency of energy loss via these pathways changes with the temperature and pressure of the local environment and the presence or suitable energy levels in the colliding body. Because of the ease of transition between energy levels, the spectrum of a molecule is more highly structured than that of an atom. In addition to being a signal loss pathway that quenches fluorescent signal, collisional energy transfer populates numerous excited states that have potential for fluorescence emission through spontaneous relaxation. This produces the clusters of closely spaced transitions of the molecular spectrum rather than sparsely distributed transitions seen in atomic spectra.
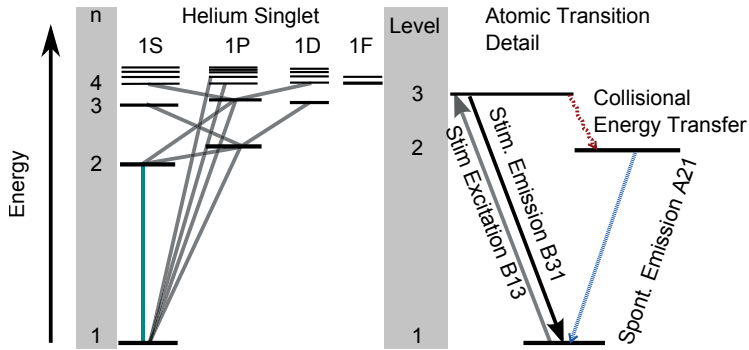
Figure 2.1: Energy level diagram for helium showing the relative energy level of the specific electronic states, adapted from Herzberg [11]. At left, selected allowed transitions shown in gray, forbidden transition in turquoise. At right suggested pathway for excitation and relaxation in an atom.
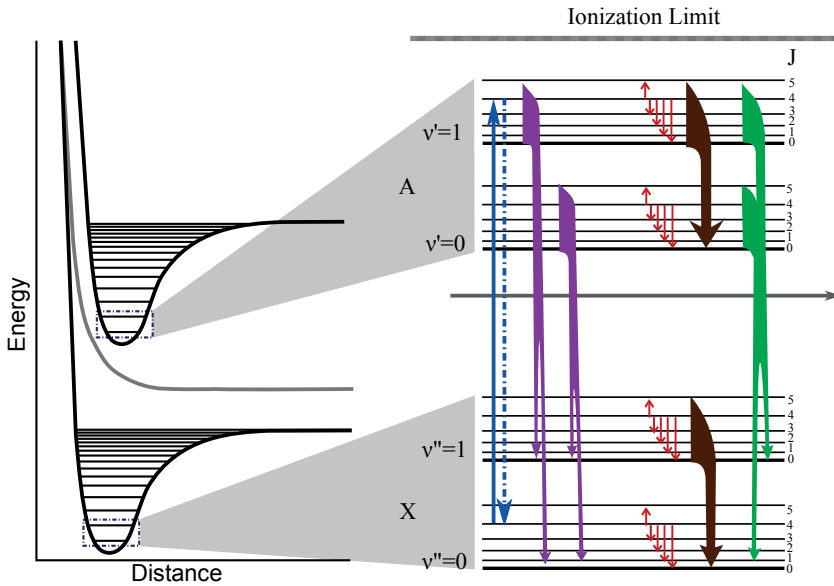
Figure 2.2: General molecular energy diagram illustrating excitation pathways. Solid blue line is stimulated absorption, dashed blue line stimulated emission, purple arrows indicate broadband spontaneous emission. Collisional energy transfers are shown in red for rotational energy transfer, brown for vibrational energy transfers and green for electronic relaxations. Grey line indicates a predissociative state.

Other molecular transitions that can occur are *ionization*, where the electron is freed from the nucleus and *predissociation*, where the excitation cause destabilization of the molecule which subsequently breaks into smaller constituents. These are single-ended electronic transitions as they deplete the population of the target molecule.

2.4 Laser Physics

LASER is the acronym for Light Amplification by Stimulated Emission of Radiation. The laser was developed from the principles found with the MASER which operates at microwave wavelengths [12]; lasers operate in the wavelength region from infrared(IR) to the ultraviolet (UV). A simple laser is composed of a cavity defined by two reflecting surfaces, a lasing gain medium, and an energy pumping system for the gain medium. The gain medium can be a semiconductor, crystalline solid, gas or liquid. Energy is applied to the gain medium by electron bombardment, electron hole recombination, flash lamps or diode arrays. Multiple stages of pumped gain media can be linked serially to the first stage(oscillator) to amplify the laser power. Lasing wavelength is determined by the gain medium, then by the cavity dimensions and may be refined by the inclusion of gratings or etalons in the oscillator to favor a wavelength. Some pulsed lasers may include an optical obstruction in the oscillator which alters the quality of the cavity. This allows the build up of energy in the gain medium during the pumping stage and a sudden release of stimulated emission over a short time period.

The physical processes which result in lasing can be realized from the discussion of molecular energy levels in section 2.3, as it derives from the stimulated relaxation from an excited energy state. Recall that stimulated relaxation will generate an additional photon for a single stimulating photon. This photon is a copy of the photon that induced the emission. In order to achieve amplification, the number of electrons in the upper level must be greater than those in the lower energy level, a condition called population inversion. Without population inversion, stimulated absorption events would outweigh stimulated transmission events. Thus, a laser gain medium needs three or more electronic levels. The energy diagrams for a three level Ruby laser, which was the first functioning laser, and the four level Nd:YAG laser are shown in 2.3 [13, 14].

The lasing process begins with the application of energy to the gain medium in order to excite electrons to a non equilibrium state. Then, the electron is moved to a different energy level which has a weak spontaneous transition probability to the lower state, called the meta-stable state. In the three level system, the population of this upper state builds until it is greater than the ground energy level, at which point a photon at the energy of the meta-stable to ground transition triggers a stimulated transition between these levels. There is a resulting cascade of photons as stimulated emission is triggered from many emitting species in the gain medium. Four level systems have the benefit of not

needing to establish a population inversion between the meta-stable and ground electronic levels. Rather, the population inversion is set up between the meta-stable and a lower lying short lived energy level. Due to the exact replication of the stimulating photon, a laser beam consists of photon energy limited to a narrow distribution of wavelengths.
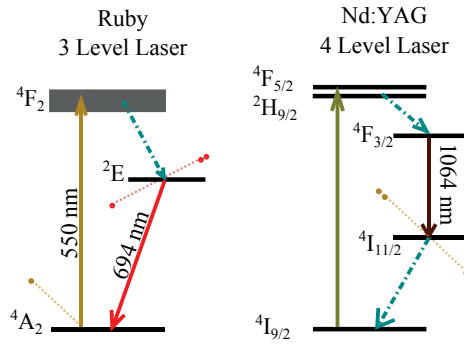

Figure 2.3: Energy level diagrams for Ruby (left) and Nd:YAG (right) lasers, demonstrating three and four level laser systems.

Diagnostics

"I suppose it is tempting, if the only tool you have is a hammer, to treat everything as if it were a nail."   Abraham Maslow
The Psychology of Science, 1966 [15]

The field of laser-based diagnostics covers a number of different strategies for the measurement of species concentration, species distribution, temperature and fluid motion, which may be useful in gaining insight to various aspects of combustion [16]. The choice of technique is directed by the suitability for the measurement environment and the desired type of information: quantitative or qualitative, spatial extent, time resolution, etc. As the purpose of this work was the validation of CFD models, two dimensional measurements would be the most appropriate, thus LIF and PIV were used. Certain traditional combustion diagnostics were also used.

3.1   Emission Measurements

In the experiments that were the basis of papers II and III, no optical diagnostics were applied, rather the product emissions from combustion were measured at various burner operating conditions. Samples were collected using a sample probe placed downstream of the combustion region for both the atmospheric and elevated pressure combustion chambers.

In early experiments, namely those in papers II and III, the detectors were an Eco Physics model 700 EL-ht nitric oxide detector, Rosemount Analytical Oxynos 100 detector for oxygen and Rosemount Analytical Binos 100 detector for CO and CO_2. The later experiments, which are used in papers I and C [17], used an Eco Physics model CLD-822Mhr nitric oxide detector, MBE PAROX 1200 oxygen detector, Fuji ZKJ CO and CO_2 detector, and a JUM 3-300 A un-burnt hydrocarbon detector.

3.2   Optical Diagnostics

3.2.1   Chemiluminescence

Chemiluminescence is the emission of radiation from atoms and molecules in which electrons were first raised to an excited state via chemical reactions. In

a flame, there are several species that are noted chemiluminescent molecules, most apparent are CH and C_2 which give a flame the blue-green coloring. If a UV sensitive imaging device is used there will also be signal from the OH radical.

As chemiluminescence occurs in the reactive regions of the flame it is a suitable indicator of flame position. However, being a line of site technique, images that are collected are averaged along the perspective line of the camera lens. There have been developments in the analytical application of flame chemiluminescence [18, 19]; but, it was used with this work to visualize the flame at high speed to observe temporal fluctuations in the flame.

3.2.2   Particle Imaging Velocimetry

In turbulent premixed combustion the fluid motion is as important to the stabilization and propagation of the flame as the chemical reaction process [20]. A complete picture of combustion should include flow fields in addition to chemical markers. Particle image velocimetry is a means of visualizing the flow by finding the displacement of small particles that have been seeded into the flow. The measurement process is illustrated in figure 3.2. A region of interest is illuminated by sequential laser pulses. A camera, which is triggered by the laser pulses, records Mie scattering from the particles. The distance that the particles travel between the two shots divided by the time separation gives the velocity of the particles.

PIV does not track individual particle motions, but rather is an averaged velocity for particles in a spatial subset of regions of the image. An image set is divided into regions which are then compared between the image pair to find the greatest agreement between displacements. The resulting velocity field yields one velocity vector per region. A detailed discussion of the PIV measurement technique is found in [21].

3.2.3   Fluorescence

Fluorescence is the spontaneous emission of a photon upon relaxation of an electron from an excited state to a lower energy level, the electron having been first excited by absorption of a photon. The observation of fluorescence in combustion was first reported by Nichols and Howes in 1923 for emissions from calcium and strontium in a hydrogen flame [22, 23]. Winefordner and Vickers introduce the usefulness of fluorescence as a diagnostic technique from the improvement in sensitivity of over chemical and thermal excitation in atomic spectrometry as the ground state population is detected, meaning the signal is less dependent on flame reactions or temperature [24]. Alkemade gave a radiometric analysis of atomic fluorescence efficiency, considering fluorescence excitation by both continuum sources and narrow line sources [25], which suggest performance improvements for limited spectral range of excitation.

Fluorescence Targets in Combustion

Fluorescence targets in the combustion environment may be naturally occurring or seeded into the combustion system. Fluorescence measurements may be used to indicate the location of flame structures, e.g., the flame front, burnt and un-burnt fraction; or, when quantitative measurements are made, can indicate chemical production rates or local temperature. Examples of naturally occurring species are the hydroxyl radical (OH), nitric oxide, carbon monoxide, the methyl radical and formaldehyde. Commonly seeded fluorescence targets are acetone, toluene, nitric oxide, indium, thallium lead, etc [26–29].

The OH radical is an oft-used fluorescence target for LIF diagnostics in combustion. OH signal appears just after the highly reactive flame front and extends into the post combustion regions of the flame. Fluorescence originates from an electron excited from the v"=0 vibrational level of the ground electronic state to the v'=1 first vibrational level of the first excited state. The transition is shown in figure 3.1. Fluorescence signal is filtered to remove the scatter from the excitation beam. The measured signal is primarily from the numerous rotational transitions of the lowest vibrational level upper electronic state to the lowest vibrational level of the ground electronic state a wavelength region around 308 nm. The OH radical was the primary target of LIF measurements that were used in producing the papers associated with this work.

Acetone (C_3H_6O) is a fluorescing hydrocarbon which can be added to the fuel or air for laser induced fluorescence imaging of the pre-combustion region. It is often used to determine the degree of mixing and equivalence ratios of the combustion mixture [30, 31]. Acetone fluorescence may be excited by the same wavelength as the OH molecule, and, as it is consumed with the fuel at the flame front, it can be used when measured simultaneously with OH to image the burnt and un-burnt regions of the combustion volume [32]. The primary use of acetone in the works associated with this thesis was in imaging the laser power distribution directly in the measurement volume for correction of laser energy distribution.

Indium is one of several atoms that are seeded into a flame for the purpose of temperature measurements [26, 27]. Temperature of the combustion region is determined by measuring the populations of indium in ground state ($5^2P_{1/2}$) and slightly elevated energy state state ($5^2P_{3/2}$) which are separated by ≈ 0.275 eV [33]. The energy separation makes indium a good temperature marker for combustion in the temperature region of 700–3000 K [29, 34]. While it was not used in connection to this work for determination of temperature, paper V features the development of an improved seeding system with application to temperature measurement of the combustion gases.

3.2.4   Laser Induced Fluorescence

The application of laser-based diagnostics to combustion is thoroughly documented by Kohse-Höinghaus [35], and particular application of LIF in combus-
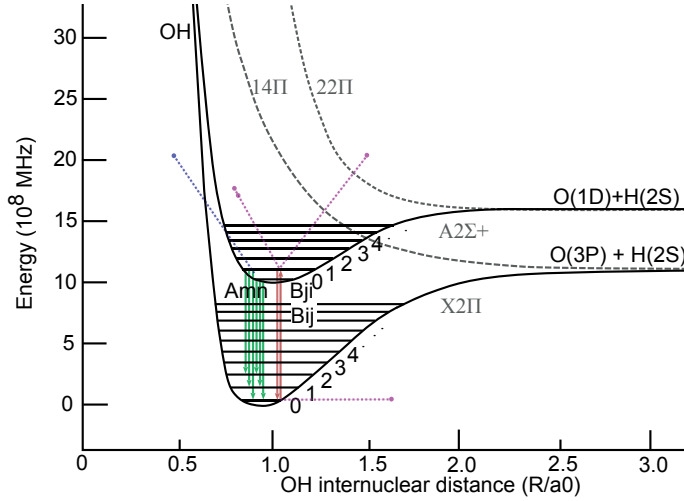
Figure 3.1: Selected potential energy curves for the OH molecule showing electronic and vibrational energy levels. Stable electronic levels are solid black lines, pre-dissociative levels in dashed gray. Transition pathways in red show stimulated pathways while green are spontaneous pathways.
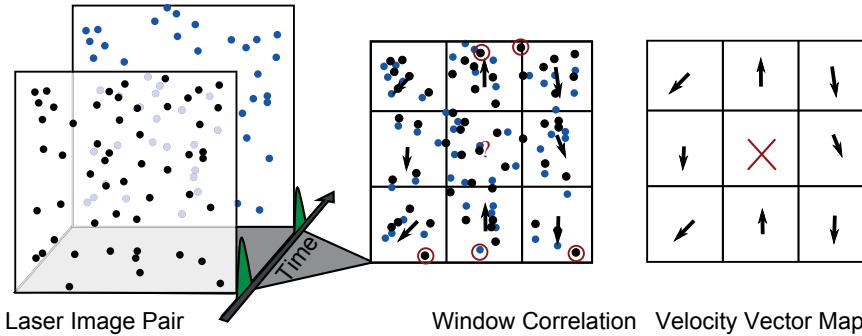
Figure 3.2: Diagram of two shot PIV sequence. Left- time delayed images are differentiated by particle color. Middle- images are split into interrogation windows and correlated to find likely displacement, particles that leave the imaging field are circled in red. Right- resulting velocity vector field.

tion diagnostics may be found in Daily or Stepowski [36, 37]. A strong motivation for the use of laser diagnostics is the quality of the detection methods due to high energy deposition and selectivity from spectral overlap of the source frequency range and target transition wavelength range.

The excitation efficiency (b) of an fluorescence excitation source is given by the ground state population (N_1) multiplied by the stimulated excitation coefficient (B) and the intensity of the excitation source (I) over the absorption profile (g).

$$b_{12} = \frac{B_{12}}{c} \int_\nu I(\nu)g(\nu)(d\nu) \tag{3.1}$$

In the simplest approximation, with constant overlap of excitation wavelength and the absorption line profile, fluorescence intensity would be directly proportional to the excitation intensity multiplied by the number density as calculated using equation 3.2.

$$F = C \ V_l \ N_1 \ b_{12} \ \frac{A_{21}}{A_{21} + Q} \tag{3.2}$$

With C being the instrument collection efficiency, V_l the probe volume, A the Einstein transition coefficients for spontaneous emission. The Stern-Volmer fraction, $A_{21}/(A_{21} + Q)$, expresses the fluorescence quantum yield. All non-emissive relaxation, which includes stimulated emission (for orthogonal image collection), collisional quenching, dissociation and any other loss mechanisms, are included in Q.

It should be noted that this equation infers that only the fluorescence from one excited state is observed. In fact, collisional energy transfer will populate other fluorescing states, a mechanism that allows the exclusion of the excitation wavelength with optical filters. With this approach, equation 3.2 would need to be adjusted to reflect a global fluorescence quantum yield.

Quenching Independent LIF

Quenching is an unwelcome complication of quantitative LIF measurements as it may be non-uniform due to variation in the measurement environment, e.g., temperature or chemical composition. However, by changing aspects of the excitation process quenching can be exploited so that a single loss mechanism is dominant. This simplifies the calculation of the fluorescence quantum yield to solvable values.

In the LIF saturation regime, the frequency of stimulated processes is greater than spontaneous processes, effectively removing the contribution of quenching from the fluorescence signal [38]. Onset of saturation ($I_{saturation}$) is thus defined by equation 3.3.

$$I_{saturation} = \frac{(A_{21} + Q_{21})c}{(B_{12} + B_{21})} \tag{3.3}$$

The fluorescence quantum yield is no longer determined by quenching but rather the ratio of stimulated excitation to stimulated emission.

$$F_{saturation} = CV_l N_1 \frac{B_{12}}{B_{12}B_{21}} \cdot \frac{A_{21}}{1 + \frac{I_\nu(sat)}{I_\nu}} \quad (3.4)$$

An additional benefit of operation in the saturated regime is that the fluorescence signal shows very little influence of the laser intensity provided it remains above the saturation threshold. It should be noted that, even when the total pulse energy is sufficient for saturation, low fluence at the beam edges and at the start and end of the pulse will contribute LIF signal at non-saturated conditions.

Some transitions in molecules will excite the molecule such that it is in an unstable electronic configuration that causes the cleavage of a bond. This "predissociated" state has a probability of fluorescing to a lower energy state but the only likely loss factor is dissociation, as these states are short lived. In this strategy the fluorescence quantum yield is the ratio of spontaneous emission to dissociation, A_{21}/P providing $A_{21} << P$. The downside of using this strategy is that LIF signal levels may be low because of the short lifetime of the predissociated state, this may be a problem in low signal-to-noise measurements.

Fluorescence Based Flame Temperature

Temperature is one of the most desired environmental variables in combustion modeling, but the gas turbine combustion environment is not amenable to this measurement due to wide temperature ranges and a highly turbulent flow [39]. While thermocouples have been used to measure flame temperatures, the physical intrusion into the measurement volume introduces error by disrupting the naturally occurring flow structures. This is especially problematic when measurements are made in the turbulent combustion environment of gas turbine which uses recirculating fluid motion to stabilize combustion in the primary combustion zone. Optical measurements do not adversely effect the fluid motion, and while the adaptation of combustion systems to permit optical access will alter environmental parameters, e.g, heat loss or geometric configuration, the measurement environment should not change with the presence or absence of the probe.

Coherent anti-stokes Raman spectroscopy (CARS) and Rayleigh scattering are the laser-based techniques most often associated with thermometry in 1 and 2 dimensions, respectively, however it is also possible to compute temperature from fluorescence measurements. The population of an energy state in an atom or molecule is not restricted to a single energy level; but rather, is distributed over all possible energy levels following the Boltzmann distribution. The ratio of populations (N) between any two states is given by difference in energy (ϵ) of the two states:

$$\frac{N_i}{N_j} = \exp[-(\epsilon_i - \epsilon_j)/kT] \quad (3.5)$$

and the absolute number density of a specific energy state can be determined by:

$$N_i = N \cdot \frac{\exp[-\delta\epsilon_i/kT]}{\sum_j \exp[-\delta\epsilon_j/kT]} \qquad (3.6)$$

Practically, only energy separations that are less than several kT above ground state are considerably populated. Fluorescence thermometry techniques are based on measuring the population of energy levels by equating the laser induced fluorescence intensity to the number density of the specific energy level probed.

There are two fluorescence thermometry techniques with sufficiently high time resolution for instantaneous temperature measurement in turbulent combustion applications. The most well know is the two line fluorescence method. The ratio of broadband fluorescence signals, F_1 and F_2, resulting from exciting the ground state and excited state corresponds to the respective number densities of the two initial states and their transition coefficients. Assuming that both excitations elevate the fluorescence target to the same upper state, the intensity ratio using equation 3.2 is:

$$\frac{F_2}{F_1} = \frac{I_{23}}{I_{13}} \cdot \frac{b_{23}}{b_{13}} \cdot \frac{N_2}{N_1} \qquad (3.7)$$

By inclusion of equation 3.5, temperature can be calculated thus:

$$\frac{F_2}{F_1} = \frac{I_{23}}{I_{13}} \cdot \frac{b_{23}}{b_{13}} \cdot \exp[\epsilon_2 - \epsilon_1)/kT] \qquad (3.8)$$

The application of this temperature measurement technique to the combustion environment has been progressing since initial discussion by Omenetto [40]. Catollica presented the use of flame generated OH as a thermometric target, mentioning the suitability for single shot, turbulent combustion measurements [41]. Demonstrations of two line fluorescence temperature measurements in flame have been performed using indium, OH and NO [28, 42, 43].

By using a fluorescence target that does not have an appreciable change in concentration throughout the measurement region, it is possible to generate a relative temperature map from a single fluorescence signal. This has been accomplished by the Hanson group using NO seeded into the combustion region [44, 45]. Additionally, they describe a method of self calibration possible when using a non monotonic transition.

Planar Laser Induced Fluorescence

LIF is frequently used to produce a two dimensional distribution of the fluorescence target in a combustion environment. The various fluorescence examples presented thus far have considered the measurement of fluorescence in a single point; extending these techniques to multidimensional measurements adds several additional variables to the fluorescence signal computation [46].

$$F = \left[I(x,y)e^{-(b_{12}+\sigma)\int N_1(x,y)dx}\right]\left[b_{12}(\nu)N_1(x,y)\right]\left[\frac{A_{21}}{A_{21}+Q}\right] \qquad (3.9)$$

The three components of equation 3.9 define, from left to right: the vertical energy distribution of the excitation pulse as a function of absorption and scattering (σ) along the laser path, the absorption by the local population of the fluorescence target at (x,y), and the fluorescence quantum efficiency. For equation 3.9 to be accurate, it is necessary that the laser is operating purely in the non-saturated regime and that quenching is constant throughout the measurement region.

Correction of fluorescence measurements for the variation in laser energy distribution across a measurement region requires knowledge of the initial intensity of the laser sheet and the amount of energy lost as the beam traverses the region. For a single shot correction, the beam can be imaged together with the LIF signal [28, 47]. Energy losses along the path of the laser can be determined by correlating the absorption at a certain height in the laser sheet to the fluorescence signal along the laser path at that height. In the case of a symmetrical flame, loss in the laser sheet energy may be inferred from the intensity change at the edges of the measurement region.

3.3   Instruments

3.3.1   Laser Systems

Nd:YAG Laser

The Nd:YAG laser is a workhorse of laser-based combustion measurement techniques. This is a solid-state laser which uses a crystalline rod of yttrium aluminum garnet doped with neodynium as the gain medium. The gain medium is typically pumped by broad emission flash lamps or alternatively pumped with AlGaAs semiconductor lasers tuned to specific neodynium transitions. The fundamental lasing wavelength most commonly used is at 1064 nm, through the $^4F_{3/2} \rightarrow^4 I_{11/2}$ transition. The Nd:YAG laser is particularly useful in laser-based research as it can produce large amounts of energy in pulsed mode, for example 1600 mJ from a Quantel YG980 or 850 mJ from the portable brilliant-B at 1064 nm. Because of the high power, it is reasonable to use Nd:YAG lasers even where significant optical losses are incurred. Often the fundamental wavelength of 1064 nm is upconverted to second, third and fourth harmonics (532, 355, 256 nm) using various non-linear crystals. By these conversions it is possible use the laser directly for fluorescence measurements such as LIF of formaldehyde at 355 nm, despite low fluorescence efficiency at this pumping wavelength [48, 49]. Another common use of Nd:YAG lasers is to pump dye lasers to produce tunable laser radiation. A shortcoming of the high power Nd:YAG laser is that the heat produced limits the pulse rate, which is typically 10 Hz, with higher repetition rates achievable at the expense of pulse energy.
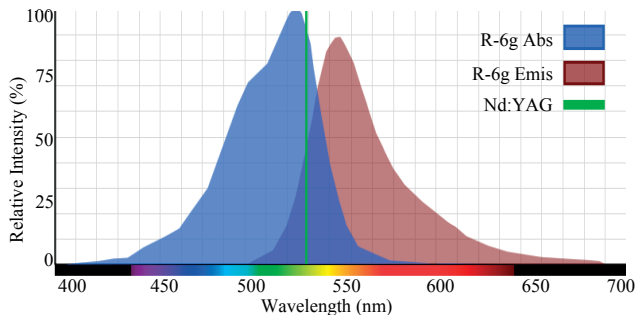
Figure 3.3: Spectral profile for rhodamine 6G. Shown for reference is the laser excitation wavelength. Data from Life Technologies [52]

Dye Laser

Dye lasers use an organic dye molecule solvated in an organic solvent as the gain medium. Laser dyes feature broad and smooth absorption and fluorescence profiles which arise from the multitude of closely lying energy states. While they can be pumped using flashlamps, the greatest efficiency comes from pumping with laser light due to the deposition of energy in the absorbing profile of the dye [50]. An example excitation and emission spectrum for rhodamine 6G is shown in figure 3.3. Laser dyes are available for the entire wavelength range of the visible spectrum and extending slightly into the infra-red. In all activities connected to this thesis dye lasers used rhodamine 6G dye in ethanol, pumped with frequency doubled Nd:YAG lasers. The dye laser wavelength is tuned to 576 nm and doubled in frequency using a KDP crystal in order to stimulate OH transitions from the $X^2\Pi(V_0) \rightarrow A^2\Sigma^+(V_1)$ energy levels. Dye lasers are prone to mode hopping whereby the wavelength changes from shot to shot [51]. This can be a significant source of error in quantitative measurements using the dye laser as the overlap between the laser line and molecule will shift during measurements.

Laser Sheet Optics

Sheet optics were universally applied in the laser based measurements that were undertaken, both PIV and PLIF. Two sheet arrangements are commonly used, a collimated laser sheet and an expanding sheet. The collimated sheet offers many advantages: beam correction can be accomplished more simply, beam alignment is simpler and beam power can be more symmetrically distributed in the sheet. The benefit of the expanding sheet obviously is that a much larger area can be probed. However, beam correction is complicated by the expansion and care must be taken to avoid reflections. In the experiments upon which this thesis is based, the collimated laser sheet form was used only in experiments performed

at elevated pressure where the optical access limited the sheet width. LIF and PIV experiments in the atmospheric rig all used expanding sheet configurations in order to probe as much of the combustion region as feasible.

3.3.2   Camera Systems

Digital imaging has opened up the field of two dimensional measurements as now repetitive measurements can be made very easily. There are two types of digital camera technology commonly used- the charged coupled device (CCD) and complimentary metal-oxide semiconductor device (CMOS). Both technologies use the same principle for photon capture, but the signal is extracted from the individual pixels in different ways [53]. The pixel is defined by a MOS structure composed of a source, sink and gate electrode. Photons impinging on a semiconductor material create an electron-hole pair that is trapped in a pixel by an electric field created by the voltages applied to the gate electrode.

CCD

In the CCD imaging sensor, read out occurs by shifting the charges along one dimension of the imaging array by varying the potentials that isolate neighboring pixels [54]. A complete review of CCD imaging principles as well as considerations for analytical measurements is found in [55]. At each iteration of the read out process, the first row of the CCD dumps into a non-photo active shift register- the readout register. The readout register is ejected one charge packet at a time through a current to voltage converter. A special implementation of a CCD is called an interline transfer or frame transfer CCD. It is designed for high temporal resolution imaging of two consecutive images. To do this, a portion of the CCD pixels are masked to make them non photosensitive. The first image is collected and then shifted rapidly to the non photo-active region. Then a second image is collected in the photo-active region. The CCD is read out and the two images reconstructed. This is the technology that is used in many PIV systems. The CCD sensor design is too slow in reading out a measurement which prohibits application of single sensor CCD imagers to high frequency measurements. Regardless, this has been the dominant digital imaging system in scientific research since its invention in 1970.

CMOS

In the CMOS image sensor, the charge is converted to a voltage at each pixel, and readout is addressed to each pixel by column and row addressing. This avoids the time consuming readout process that is done in the CCD imager. Also the row and column addressing means that imaging can be restricted to an area of interest with consequent gains in image collection speed. CMOS imaging systems have been less frequently used in quantitative imaging as pixel signal can be less uniform than CCD imaging systems. This has been improved with the

development the CMOS active pixel sensor which allows on pixel amplification and correction of pixel response [56]. Some semiconductor material of a CMOS imager is devoted to the charge conversion and pixel addressing circuitry which reduces the photo-active area of the sensor. While the lower sensitivity of the imaging chip may be a problem in low intensity conditions, the per-pixel voltage conversion can give lower readout noise and thermal noise than CCD imagers, as the data spends less time on the semiconductor before being digitized.

Image Intensifier

An intensifier is an electronic device that converts photons to electrons which are multiplied many times and then converted back to photons for recording by an imaging device. A thorough description of operating principles and characteristics of the image intensifier is found in [57]. At the entrance of the device photons strike the surface of the photocathode which has applied to it a high voltage. Electrons produced by the photocathode are repelled by the electric field and enter the multi-channel plate (MCP) amplifier section which is held at a lower voltage than the photocathode. The electrons impact the walls of the MCP whereupon they generate a packet of secondary electrons. This electron impact and multiplication process cascades down the length of the channel. At the end of the the MCP the electrons strike a phosphor coated plate which converts the electrons back into photons. The photons are directed toward an imaging sensor either by use of a fiber optic bundle or lenses. The primary motivation for using an image intensifier is for the amplification of the photon signal; as added benefit, the intensifier allows for time gating the signal collection, this reduces spurious noise sources. When an appropriate intensifier is used the response range of the imaging device can be extended to the UV region. This is important for capturing rapidly changing systems in a time interval that reduces spatial blurring of the image.

3.3.3   Image Correction

Quantitative Imaging

Ideally a two dimensional measurement will show a correlation between quantity of a target at a position in the probe volume and the intensity recorded on an imaging device resulting from that volume. This is the basis of a quantitative measurement. In practice, the reported signal (S) includes, in addition to the analytical signal (n_s), the spurious signal in the measurement volume, called background signal (n_B), and counts that are created in the imaging device, called dark signal (n_d) [58].

$$S = n_s + n_B + n_d \tag{3.10}$$

Associated with these signals is a variance, σ, of a given signal component relative to the absolute value. It is this variation in signal levels that set the

limit of detection for a measurement [59].

Each pixel of a CCD can be considered an individual sensor [60], which has a unique dark signal component and responsivity in addition to the false component of the signal from background emission and inconsistency in the analytical response. In LIF, background comes from chemiluminescence, laser scattering and contaminating fluorescence. In the abscence of proper optical filtering, laser scattering (Mie and Rayleigh) will be present in all pixels imaging the measurement region, with an intensity varying from the local density and scattering cross-section. Contaminating fluorescence is fluorescent signal from non-analyte fluorescence targets in the measurement region. Both scattering and contaminating fluorescence are a function of laser energy and will fluctuate with the pulse power. Nonlinearity in the analytical signal has been addressed in section 3.2.4.

Dark signal can be reduced by cooling the image sensor, as much of this signal is due to the thermal generation of electron-hole pairs in the image sensor. The level of dark signal can be evaluated by covering the objective and recording the image intensity. This two dimensional dark signal array should be subtracted from further measurements.

Correction for the sensitivity of individual pixels is done by collecting a signal of a uniformly illuminated sensor. This two dimensional response is corrected for dark signal and then each pixel is normalized by the average pixel response [55]. Dividing a dark subtracted image by this value will remove distortion arising from the electronics.

Background signal can be reduced by the use of temporal and spectral filters. Limiting the exposure to ≈ 100 ns allows collection of the fluorescence signal while reducing chemiluminescent signal to a few counts per pixel. The use of optical filters will block most laser scattering and some contaminating fluorescence. If background reduction is insufficient, it may be possible to image the background signal without the analytical signal, by taking a blank image. For LIF measurements this is done by moving the laser wavelength away from the analyte excitation wavelength. The blank image would thus contain any contaminating fluorescence, laser scattering or other emission.

Qualitative Imaging

It is often unnecessary to correct an image to quantitative accuracy [61] provided that there is sufficient understanding of what conclusions may be drawn from a non-quantitative image. Also, applying a few corrections may increase the value of the image data. A raw planar-LIF image will show the areas of the measurement region where the fluorescence target combined with the laser energy produce a fluorescent signal greater than the detection threshold of the imaging system. This is used as a basic indication of the presence or absence of the analyte. Subtracting a blank image is assurance that the signal seen is indeed from the fluorescence target, though this may be unnecessary depend-

ing on fuel and operating conditions. Correcting the raw data for the laser intensity distribution permits comparison of relative concentrations of the fluorescence target between areas of the flame, provided that the entire fluorescence measurement is non-saturated.

Gas Turbine Combustion

Combustion engines convert the chemical energy contained in *typically* hydrocarbon fuels into heat which is used to create mechanical motion. This is either done through applying heat to a working fluid, as is done in steam engines, or containing the hot expanding combustion gases as in internal combustion engines. Internal combustion can be further split into piston and gas turbine, although this distinction is perhaps more accurately a split between a batch reaction or continuous reaction engine. Piston engines see greatest usage in applications where wide load range and good part load efficiency is desired, such as in automobiles. Gas turbines are used in constant load systems such as power production.

This chapter opens with a brief consideration of the design goals that have directed the evolution of gas turbine combustors. Following this, the prototype gas turbine burner is described.

4.1 The Gas Turbine Combustor

From the combustion diagnostics perspective, the combustor is the most important component of the gas turbine. The compressor provides the air for combustion at a pressure above ambient level and the turbine converts the energy of the exhaust gas into power for driving the compressor and other attached devices. But it is in the combustor that the energy contained in the fuel is released for driving the engine and attached devices.

All gas turbines share some common design requirements in order to achieve efficient and stable combustion. A diagram of a generic gas turbine combustor is shown in figure 4.1. At the exit of the compressor the air flow is slowed by expansion which reduces pressure loss from combustion. Fuel is supplied to the primary combustion region which is stabilized in the recirculation zone produced by a swirl element in the primary air path. Air is provided in a manner that the flame is not cooled too quickly, but complete combustion is still possible. Cooling air is provided at various places along the combustor liner to protect the surfaces from excessive temperatures. At the combustor exit, dilution air is added to create a temperature distribution in the combustor exhaust that is compatible with the material tolerances of the turbine and turbine inlet guide vanes.

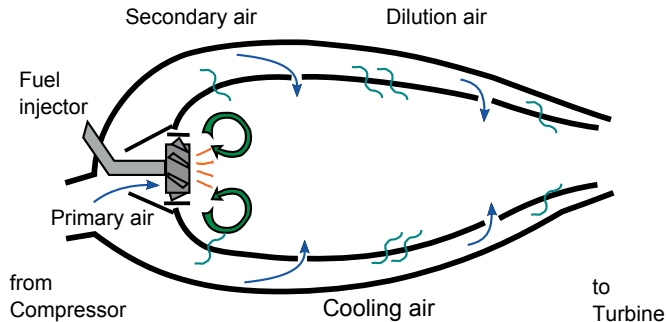Much of the early developments of the gas turbine combustor dealt directly

Figure 4.1: General layout of a gas turbine combustion chamber.

with combustion stability and material properties. Injection systems were developed that overcame problems of corrosion, coking, improved fuel vaporization and spray uniformity. Development of temperature tolerant materials, surface cooling and combustion chamber design allowed for increases in turbine inlet temperatures for greater efficiency and lower specific fuel consumption [62]. As a result of optimization of the combustion chamber and burner design, gas turbine combustion efficiency is near unity for natural gas combustion at the design point [5].

4.2 Gas Turbine Emissions Considerations

After 1970, gas turbine combustor designs began to address secondary problems of combustion due to the increasing visibility of combustion induced urban smog and acid rain [63, 64]. Significant amounts of soot, sulfur oxides (SO_x), nitrogen oxides (NO_x), and carbon monoxide (CO) were associated with the early generations of gas turbines. Many of these pollutants were reduced in conjunction with other combustion problems, e.g., removing sulfur from fuels reduced corrosion of combustor components as well as eliminating SO_x. Sooting and CO which are the product of poor combustion have been effectively eliminated by improved injection and fuel mixing in the burner. Reduction of other pollutants, specifically NO_x is more complicated.

NO_x is produced by combustion in the presence of nitrogen, as when air is used as the source of oxygen. There are four dominant chemical pathways to NO_x production in gas turbine conditions: prompt NO_x, nitrous oxide and thermal-NO_x pathways for typical gas turbine fuels, and the NNH pathway for some high hydrogen fuels [65, 66]. The greatest production of NO_x is via the thermal NO_x pathway, when fuels burn close to the stoichiometric equivalence ratio. Increasing the combustion temperatures for producing higher turbine inlet temperatures that are associated with improved engine efficiency can translate to higher NO_x production. However, lowering the temperature of combustion may be associated with an increase in CO emission as fuel oxidation may not proceed

to completion.

To force the reduction of NO_x emissions from combustion, incrementally tightening regulations were established regarding permissible NO_x levels [67, 68]. To meet these emissions goals, gas turbine designs began to include in-combustor or post combustion NO_x reduction approaches. In-combustor NO_x production rates were reduced first by the implementation of water injection systems [69] and then by development of the premixed and staged combustors to achieve dry, low emissions (DLE). DLE burners may incorporate premixing of the fuel and air so that a uniform equivalence ratio is achieved in the combustor, eliminating the stoichiometric, high temperature regions found in non-premixed combustion.

Conventionally, CO_2 was not considered a pollutant, as it is an end product of complete combustion. However, concern over the role of CO_2 in the atmospheric energy cycle has brought attention to human contributions to atmospheric CO_2. As gas turbine combustion efficiency is near unity, the only change to the combustion chamber that will lead to reduced CO_2 production per unit of power is the use of CO_2 neutral or reduced impact fuels. Coupling environmental altruism to the financial incentives of burning available, under-utilized alternative fuels, there is interest in the gas turbine community to use natural gas substitutes as an energy supply.

4.3   Syngas Fuel

The composition of alternative fuels varies based on the source of fuel or process by which it is produced. Examples of these alternative or "synthesized" fuels (syngas) are process gas, associated gas and biomass sources [70–72]. Process gas is combustible gas that is generated from industrial processes such as coke production or blast furnace operation. Process gas may have high hydrogen content as well as inert components. Associated gas is the fuel that is burnt by flaring in the refining of petrochemicals. It can have a significant fraction of longer hydrocarbons. Biomass is converted to fuel by gasification or biodigestion, both methods may include large proportions of inert gases. Additionally, blends of natural gas with other fuels may be considered as syngas.

Syngas fuels are seeing increased utilization in the gas turbine sector with much of the earliest implementation in non-premixed gas turbines [73]. This may be attributed, in part, to the absence of combustion phenomena like flashback in non-premixed combustion making the variability of syngas fuel combustion properties less vital to stable combustion. Premixed combustion is sensitive to perturbations, with potential for damage to occur should combustion progress into the premixing regions of the burner, so greater consideration must be made for the way in which the fuels burn. For instance, hydrogen has a fast burning velocity, but a low energy content by volume. Heavier hydrocarbons in contrast have a very high energy content by volume. Inert gases lower the energy content in the fuel and also reduce the flame speed [74, 75].

Table 4.1: Gas composition for investigated fuels.

Fuels	Gas Compositions vol.%				W [MJ/m³] †	LHV [MJ/kg]
	CH$_4$	H$_2$	CO	N$_2$		
Methane	100	0	0	0	55.30	50.01
Diluted Methane	33.5	0	0	66.5	15.00	11.19
Syngas	10	67.5	22.5	0	27.70	33.14
Diluted Syngas	6.9	46.56	15.52	31.02	15.00	14.05

†W: Wobbe calculated from higher heating value at 1 Atm and 273.15 K

The experiments associated with the presented works featured four fuels. The chemical composition and heating value of these test fuels are shown in table 4.1. Methane was chosen as a surrogate for natural gas as it is the primary component of natural gas. The sygnas composition is similar to the composition found for coke oven gases. Both methane and sygnas were diluted with nitrogen to a Wobbe index of 15 mJ/m³ which is comparable to process gases. Measurement of the laminar flame speed for the syngas is presented in paper IV. At 300 K the burning velocity was measured at $\approx$ 140 cm/s [76], with preheating of the combustion mixture to $\approx$ 550 K the burning velocity increased to $\approx$ 250 cm/s though this value is suspect as there were problems with flashback for these measurements.

4.4 Prototype DLE Burner

A prototype industrial burner, which shares similar design concepts with the burner implemented in the Siemens SGT-750 gas turbine, was the object of testing for this thesis work. The burner unit was sized to be suitable for laboratory scale facilities. It is a dry-low emission (DLE) combustor concept, the fourth generation in the Siemens DLE design lineage. The burner was conceived with the potential of being a flexi-fuel burner, which was investigated by including three fuels of various chemical makeup. To reach dry low-NO$_x$ emission levels the burner mixes the air and fuel in fuel lean ratios prior to combustion. In this way the near-stoichiometric high temperature regions, which occur in partially premixed flames, are avoided. The burner has three discrete combustion sectors, a central partially enclosed pilot burner, an intermediate combustion and a main combustion sector[1]. An illustration of the burner is shown in figure 4.2

The three burner sectors support discrete control of the local combustion mixture. Individual mass flow controllers were used to modulate the fuel flow to each sector, thus the equivalence ratio in each sector could be varied independently. The main and intermediate sectors share a common air supply, with 79% of the air flow passing to the main sector and 21% going to the intermediate sector. As a result, while it is possible to control the equivalence ratio

---

[1]In the associated publications main, intermediate and pilot sectors were labeled main, pilot and RPL. The assignments used in this thesis are more fitting for the observed role of the various sectors during experiments.
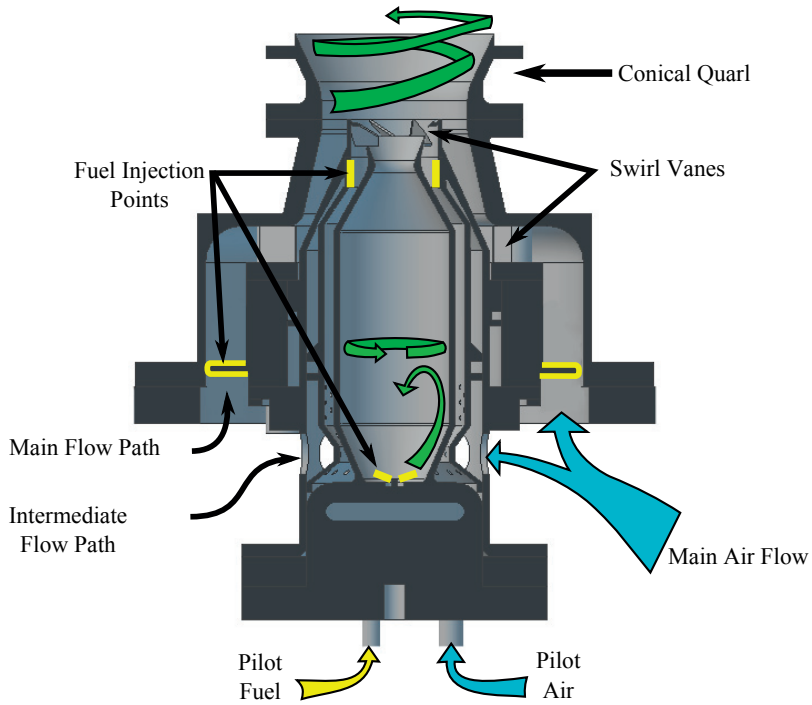
Figure 4.2: Siemens prototype DLE burner full assembly. Fuel injection points are highlighted with yellow. Air supplies are depicted with blue arrows. The anticipated swirl and recirculation are illustrated with green arrows.
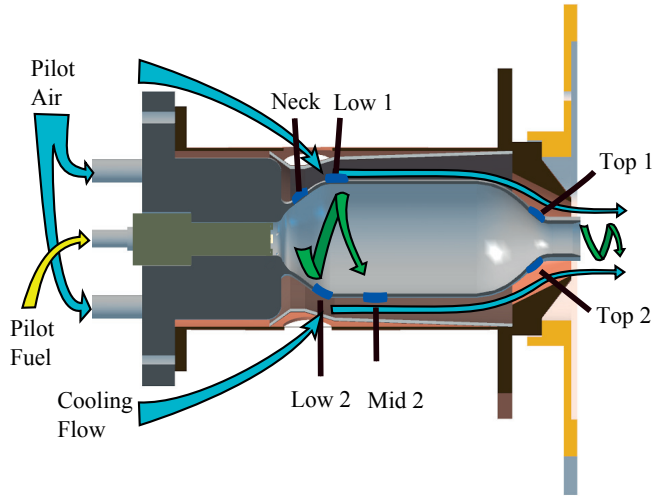
Figure 4.3: Mounting adapter housing the pilot burner sector. Locations of affixed thermocouples are shown by blue patches. Green arrows indicate anticipated swirling flow induced by injection ports at the base of the pilot sector.

in each of these two sectors separately, it was not possible to change the mass flows individually. The pilot sector has an air supply path that is isolated from the other two sectors making it possible to control both the equivalence ratio and the loading irrespective of the intermediate and main sectors.

At the heart of the larger burner assembly, the pilot sector is in effect a self contained, partially enclosed burner. Air and fuel injection ports in the base of the pilot sector create a swirling combustion mixture that expands along the wall of the pilot combustion chamber, recirculates and exits the pilot combustion chamber. [77, 78] The effluent of the pilot sector then blends into the intermediate and main combustion flows. In testing the pilot sector was operated over a range of lean and rich equivalence ratios, and by extension a range of burning velocities.

Because of the importance of the pilot sector in stabilizing combustion it was studied in detail. An adapter was made to allow mounting of the pilot sector in test rigs and provide cooling to the outer wall of the pilot, replacing the action of the intermediate flow path in the complete burner assembly. The adapter does not provide any swirl to the flow surrounding the pilot effluent. An illustration of the pilot sector and mounting adapter is shown in figure 4.3. The figure also highlights the location of the six thermocouples affixed to the outside surface of the pilot combustion chamber.

Atmospheric Pressure Combustion

Atmospheric pressure experiments were used for the bulk of the publications associated with this thesis. While those experiments obviously lack the high pressure environment that is associated with gas turbine combustion, there are benefits to working at atmospheric pressure. The absence of significant pressure in the combustion chamber allows greater flexibility in the design of the combustion liner; for example, the inclusion of large windows at the height of the reaction zone or optical diagnostics. Fuel provision is simpler at atmospheric pressure because the mass flow increases with pressure if the volume flow is to be held constant. The low mass flows needed mean that fuel can be sourced from bottles rather than high flow mixing stations. Some experiments are not feasible at elevated pressure facilities because risk of damaging facility components, e.g., PIV particles clogging sensors and valves, and so these experiment are more suitable for the atmospheric pressure facility.

5.1 Atmospheric Pressure Facility

A schematic of the atmospheric facility, as configured for laser based measurements, is shown in figure 5.1. The support rig provides up to 100 g/s airflow with heating up to 900 K and includes computer control and monitoring of various experimental parameters. Air is supplied by two blowers set in parallel. The mass flow rate is monitored by thermal mass flow controllers that are located between the blower and heater. The mass flow is controlled by varying the blower speed with a variable frequency AC power supply. The flow rate is set and monitored using an in house computer control program (see Appendix 1). Electrical heaters, which were located after the mass flow meters, were used to raise the bulk air temperature. Experiments were typically performed either at room temperature (300 K) or a gas turbine relevant temperature between 500 and 650 K. After passing the heaters, the parallel air paths are combined before entering a vertically oriented burner mounting section. The base of the burner mounting section features a pair of laminar flow elements that disrupt any strong flow features induced by the bent tubing and four PIV seeding ports. A temperature probe is located just before the burner mounting position. After passing through the burner and combustion liner air and exhaust is extracted with a high volume exhaust system.

The combustion chamber is the volume where the fuel and air provided by the burner undergo reaction. It is composed of a quarl, a combustion liner
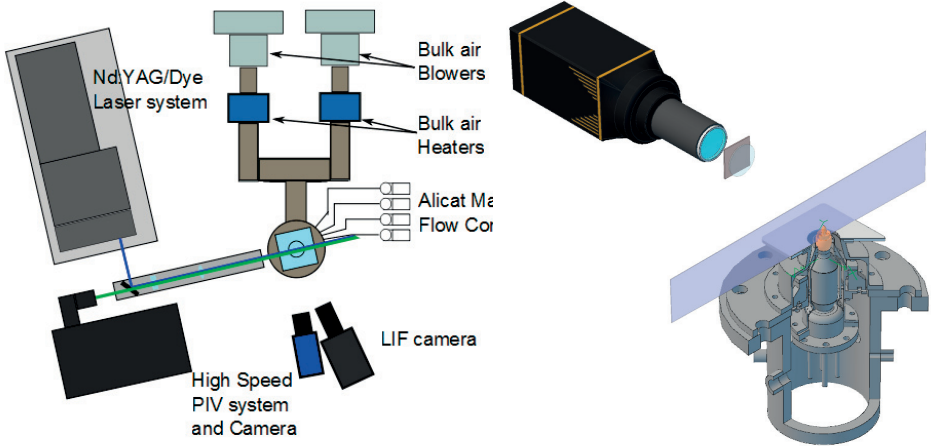
Figure 5.1: Schematic of the Atmospheric Test platform. Set-up depicts common assembly for emission, PIV and planar LIF measurements

and a exhaust contraction. The quarl attaches the burner to the combustion chamber and supports the combustion liner. The connection between the quarl and burner, termed the burner *throat*, was used as the reference point for gas velocities in experiments. There are three configurations for the quarl, which are shown in figure 5.2. In practical applications the quarl features a conical expansion that supports the swirling flow created by the burner; a flat plate was used when access to the burner exit was desired. Circular and square cross sections were used depending on the desired combustion liner geometry. The combustion liners were either of a circular cross-section of 87 mm or a square cross-section with 105 mm side length. For optical access, the combustion liners had a lower section made of quartz that was 30 cm long for the circular and 26 cm long for the square liner. These quartz sections were followed by a 40 cm steel liner section. At the end of the combustion liner was a steel conical attachment that contracted to a 57 mm diameter by 20 cm long exhaust tube. An emission measurement probe was located at the midsection of this exhaust tube. The combustion chambers assemblies are shown in figure 5.3.

The combustion chamber of the SGT-750 is radially symmetric, which would promote the use of a circular combustion chamber. However, in laser measurements where the probe wavelength cannot be filtered out, i.e., scattering methods, the circular chamber can suffer from excessive reflections. A square cross-section combustion chamber usually limits reflections to the windows through which the laser passes. The dimensions of the square cross-section liner are the same as the dimensions of combustion liner used in the elevated pressure facility, allowing some comparison between the atmospheric and elevated pressure measurements.

Figure 5.2: Quarl designs. From left to right, flat plate, circular conical expansion and square conical expansion.

Figure 5.3: Three burner confinements used in atmospheric testing. Burner attaches from the left with quarl, which interfaces to the combustion liner. Liners terminate at right with a contraction and exhaust tube where the emission sampling port is located.

5.2   Burner Lean Blowout Limit

Burner lean blowout limit (LBO) was investigated for the test fuels with variation of the pilot sector equivalence ratio. The lean blowout limit signifies the point at which a fuel/air mixture is unable to sustain combustion and the flame extinguishes. This is linked to the ability of a fuel to be ignited by recirculated hot combustion products, thus fuel heating value and laminar flame speed will have a significant role in LBO onset. Testing the various fuels in this burner was done to build an understanding both of the role of the pilot burner sector in stabilizing combustion over the full burner and the variation in stability for operation with different fuels.

The LBO was specified as the total equivalence ratio at which the burner CO emission passed 200 ppm. From an initial, stable operating point, the combustion mixture was changed to increasingly lean total equivalence ratio by stepwise reduction of the equivalence ratio for the intermediate and main sectors, leaving the pilot sector equivalence ratio unaltered. The testing was performed using methane, syngas and dilute syngas, and iterations were done for a range of pilot sector equivalence ratios. A complete description of experiment and results may be found in paper II.

There was a universal trend of greater stability as the equivalence ratio of the pilot sector was increased. This was seen in both the LBO occurring at lower total equivalence ratios and a reduced fluctuation in the CO measurement. When burning methane, the LBO was reduced from $\phi \approx 0.45$ to $\phi \approx 0.42$ for an increase in the pilot sector equivalence ratio from 1.00 to 1.80. The greatest reduction in LBO was seen for the pilot sector $\phi = 1.60$. Surprisingly, at the pilot sector $\phi = 0.80$ operating point, the stable combustion transitioned directly to LBO without a sharp increase in CO level. With syngas it was possible to operate the burner without combustion in the pilot sector. Increasing the pilot equivalence ratio from $\phi = 0.0$ to 1.44 lowered LBO from $\phi = 0.272$ to $\phi = 0.24$. The 15 MJ/m^3 dilute syngas was operated over an equivalence ratio range of $\phi = 0.32$ to 1.44, which resulted in a lowering of the LBO from total $\phi = 0.258$ to 0.247. The decrease in LBO was abrupt for dilute syngas, with little change seen when increasing the pilot equivalence ratio above $\phi = 0.96$.

5.3   Burner NO$_x$ Emission with Fuel Staging

NO$_x$ emission was measured as a function of the fuel partitioning among the three burner sectors. The intermediate and main sectors were evaluated simultaneously by biasing the flow of fuel from one sector to the other but keeping the same total burner equivalence ratio. During this phase the pilot sector equivalence ratio was set to $\phi = 0.80$ in the case of methane or $\phi = 0.64$ for syngas and dilute syngas. The maximum possible equivalence ratio that could be achieved by the intermediate sector was $\phi = 1.75$ for methane, $\phi = 0.50$ for syngas and $\phi = 0.72$ for diluted syngas. The NO$_x$ contribution from the pilot sector was

evaluated by setting the equivalence ratio in the intermediate and main sectors to a specific value and then changing only the pilot sector equivalence ratio. The full presentation of this experiment is found in paper III.

Partitioning fuel between the intermediate and main burner sectors shows a geometric growth in the NO_x level when fuel is biased to the intermediate sector. The 4:1 main to intermediate flow ratio causes, in part, the more rapid increase in equivalence ratio as fuel is directed to the intermediate sector. However, it was found that the intermediate zone produced higher emissions at a given equivalence ratio than the main sector for the same equivalence ratio. It was determined by CFD that the intermediate flow path was not fully premixed, causing inhomogeneity in the local equivalence ratio and slightly elevated NO_x levels. Testing of the NO_x generation in the pilot sector showed that it was the largest contributor to NO_x of all three sectors, despite only 2.4 % of the total fluid flow passing through this sector. NO_x level normalized against a specific NO_x value is shown in figure 5.4. The emission trends for Syngas and dilute syngas are similar, with peak emissions occurring when the equivalence ratio is near stoichiometric, while methane peaks at a much higher equivalence ratio of $\phi = 1.6$. The lack of a decrease in the NO_x at rich equivalence ratios would suggest that methane combustion is somehow non-premixed. This would be the case if combustion is occurring outside of the pilot sector upon mixing with the relatively oxygen rich intermediate flow.
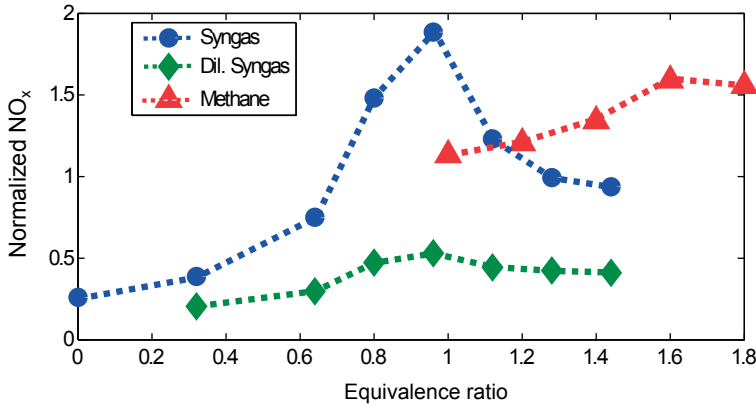

Figure 5.4: Normalized NO_x emission values for methane, syngas and dilute syngas as a function of the pilot sector equivalence ratio.

5.4 Laser-based Imaging

5.4.1 Pilot Sector Imaging

The strong NO_x emission seen in the pilot sector prompted isolation of that sector to see if the flame structure may give understanding of the NO_x emission. These tests are being used as the subject of paper VI. The pilot sector was mounted in the atmospheric pressure rig using the cooling adapter and square cross-section liner which are described in section 5.1. Measurements were made at operating conditions similar to those used during the emissions testing: pilot air preheated to 650 Kelvin, 27.5 ms residence time in the pilot body and equivalence ratio ranging from $\phi = 0.80$–1.80.

Chemiluminescence and OH-LIF signal at the exit of the pilot sector for three equivalence ratios is shown in figure 5.5. At lean equivalence ratios there is little flame chemiluminescence but a broad OH-LIF signal beginning at the lip of the pilot sector. As more fuel is added, bringing the equivalence ratios near stoichiometry, the chemiluminescence and OH-LIF signal appear alike in shape: a v-shaped flame brush extending from the pilot sector. Once into rich equivalence ratios, the OH emission appears lifted from the burner exit while the chemiluminescence is attached, though the shapes are very similar.

Flame shape, as imaged by the chemiluminescent and OH-LIF signal distribution, provides a possible explanation of the NO_x emission profile for methane shown in figure 5.4. When the pilot sector is operated below stoichiometry, combustion is contained mostly within the body of the pilot sector. Chemiluminescence signal is missing as the reaction zone is not in the measurement region. The diffuse OH signal arises from OH which has been produced in the reaction zone mixing uniformly before exiting pilot sector. As the equivalence ratio is increased above stoichiometry, combustion within the pilot sector body is increasingly incomplete, resulting in the flame transiting the pilot sector exit where mixing with more oxygen finishes the combustion of the excess fuel. At excessively high equivalence ratios, the combustion may in fact quench inside the pilot sector, resulting in a non-premixed like flame stabilizing at the rim of the pilot sector. This progression is also supported by the temperature profiles noted in the pilot sector walls which show a temperature drop at equivalence ratios greater than $\phi = 1.40$ (paper VI, figure 4).

5.4.2 Pilot and Intermediate Imaging

A series of imaging experiments were performed to see the how the pilot, intermediate and main sectors interact with one another. The full burner was mounted in the atmospheric pressure rig and the flat plate used in place of the conical quarl. This was done so that OH-LIF measurements could be made near the onset of combustion, though the exit of the pilot sector is about 1.5 diameters upstream of the imaging area. Each fuel from table 4.1 was tested
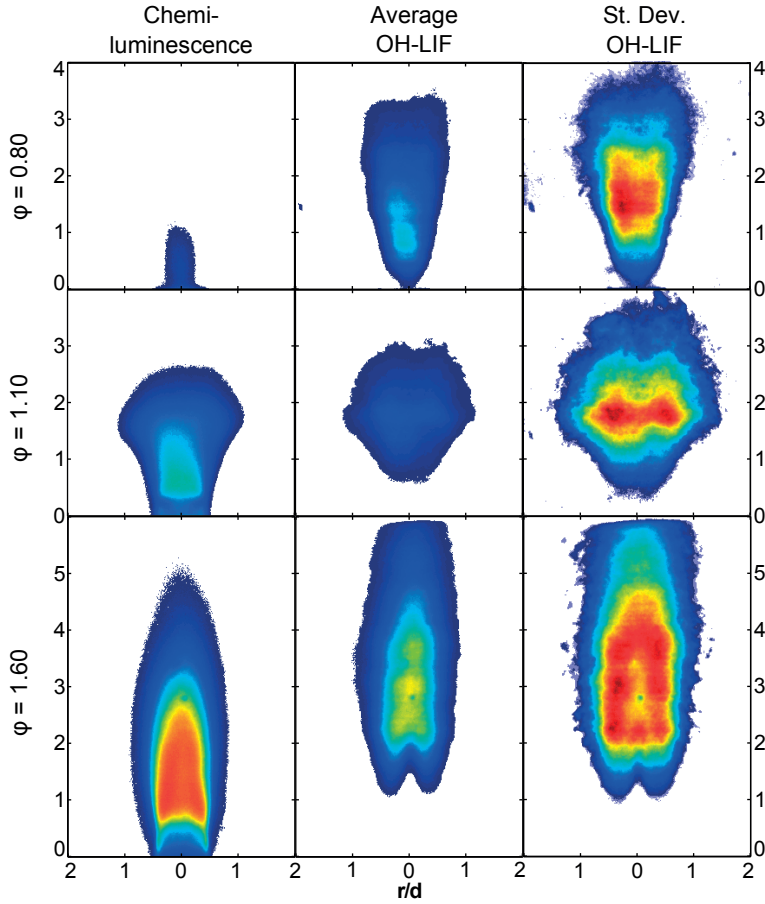
Figure 5.5: Chemiluminesce and OH-LIF signal for methane combustion in pilot sector. Three typical flame distributions shown.

using similar conditions to those which were used in the prior experiments. Observations were made with fuel supplied only to the pilot sector, and fuel to both the pilot and intermediate sectors. Combustion in the main sector was only successful for the syngas fuel; it is not considered here. The results of this experiment were used in paper D [17].

The sequence of images in figure 5.6 shows the OH-LIF signal for flame from the pilot sector and intermediate sector. The pilot sector operated at equivalence ratios of $\phi = 0.80$ for methane and dilute methane, $\phi = 0.64$ for syngas and dilute syngas. The equivalence ratio of the intermediate sector was chosen such that the adiabatic flame temperature would be uniform across all fuels; but, due to a mis-calibration of the syngas and dilute syngas fuels there was a lower equivalence ratio and flame temperature for those fuels in comparison to the methane and dilute methane fuel. When the burner is operated with fuel provided only to the pilot sector there is a diffuse OH-LIF distribution for each of the fuels tested, similar to the case seen in figure 5.5 for $\phi = 0.80$. With the addition of a swirling co-flow (the pilot sector mounting did not feature swirl) the OH-LIF distribution is expanded radially, intermixing with pilot sector. Dilute methane shows a stronger signal than the other fuels, suggesting that combustion is occurring closer to the measurement zone than the other fuels. The width of the OH-LIF distribution and the high intensity found in the outer edge suggests that the swirling surround draws the flow from the pilot sector outwards. When fuel is added to the intermediate zone the OH-LIF signal is much more intense, as combustion is producing OH in the laser measurement region. Methane and dilute methane do not burn to the full diameter of the intermediate sector, whereas syngas and dilute syngas both show OH-LIF signal extending out to the full diameter of the intermediate sector. High intensity regions seen in the upper portions of the pilot plus intermediate sector combustion are demonstrative of partial LIF saturation in the laser sheet.

5.4.3   Confinement Geometry

A series of experiments were performed to discern possible differences in flame distribution between the round and square combustion liner cross-sections. A round configuration is preferred as it is more typical of a conventional combustion liner; however, PIV measurements are made possible by the square cross-section as the parallel windows reduce scatter. Planar OH-LIF measurements were taken in both the square cross section and circular cross-section combustion liner. The settings are equal with regards to flow rates and temperatures: 60 m/s velocity through the burner throat, and 650 K at the burner inlet. The difference in cross-sectional areas of the two combustion liners results in a 48% higher average axial flow velocity in the circular cross-section liner as compared to the square cross-section liner.

Single shot measurements of methane and dilute syngas combustion are shown in figure 5.7. For both liner cross-section geometries the methane and dilute methane fuels did not burn as closely to the wall as the syngas and dilute
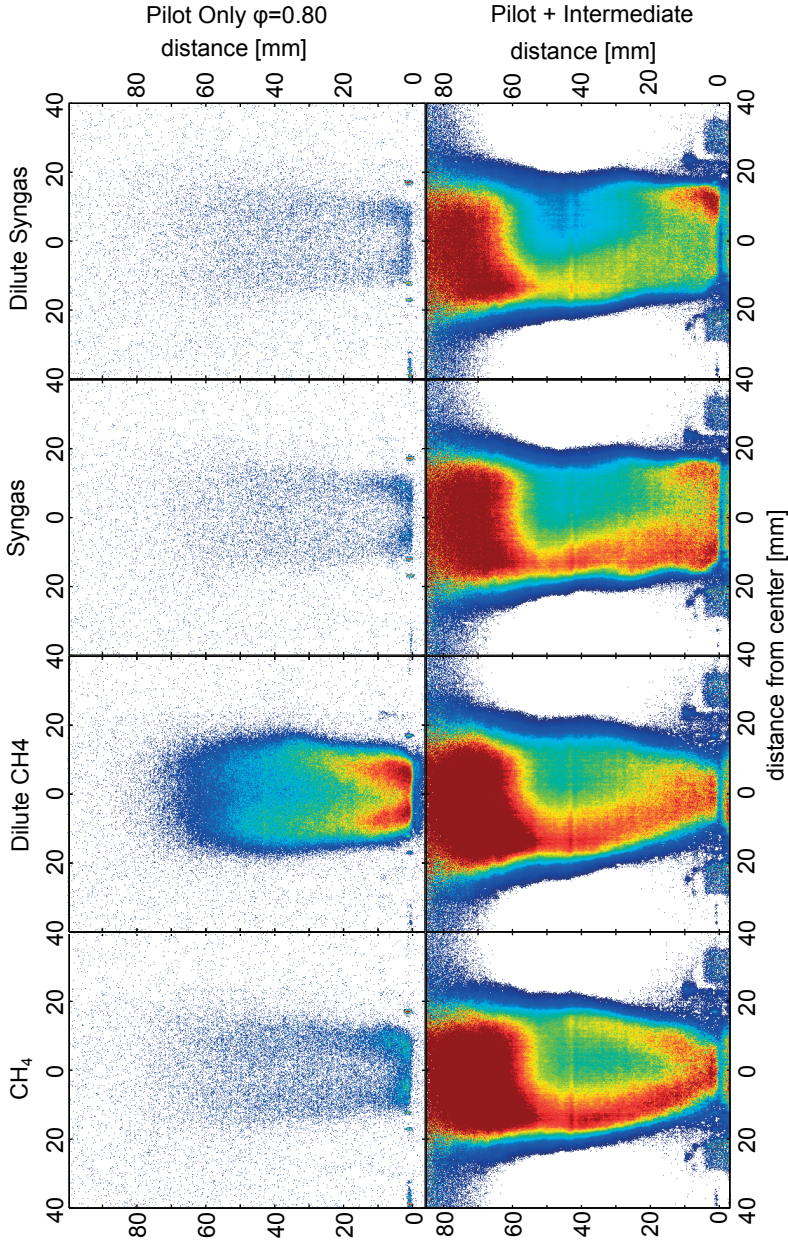
Figure 5.6: OH-PLIF for fuel supplied to pilot (upper) and pilot + intermediate sectors (lower). Pilot equivalence ratios are $\phi = 0.80$ for methane and $\phi = 0.64$ for syngas, intermediate equivalence ratios varied by fuel. Intense regions in the pilot + intermediate may be caused by over-correction of the laser sheet profile.
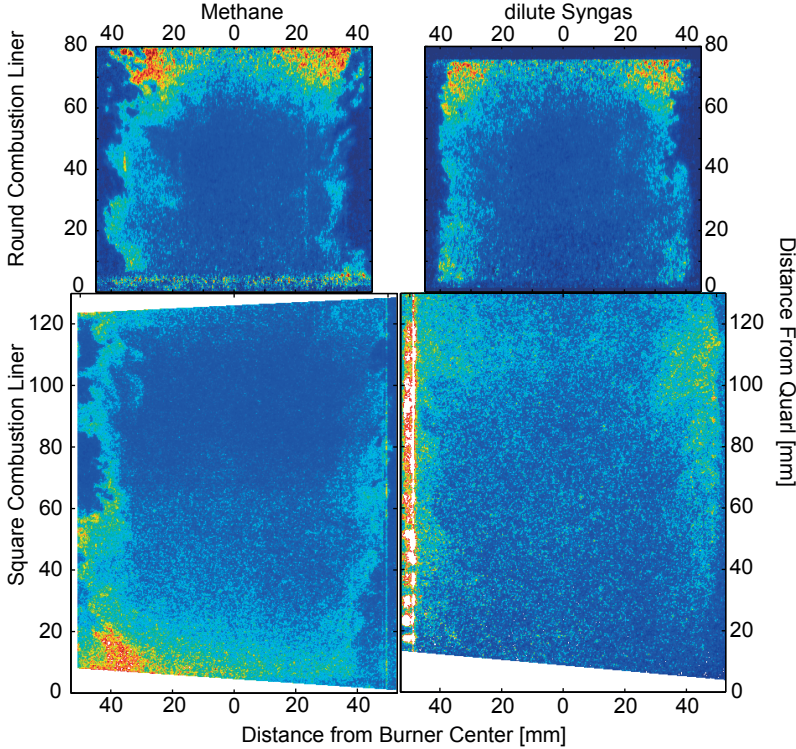
Figure 5.7: OH-LIF imaging of combustion from round and square cross-section liners. Methane combustion shown at left dilute syngas combustion shown at right.

syngas fuel. In the square liner the flame penetrates closer to the edge of the combustion chamber, most clearly exhibited by the dilute syngas flame when comparing the two liner geometries. The tendency of the square combustion chamber to burn closer to the walls may be due both to the slower axial velocity and the presence of corner vortices that induce the central rotating flow to deform [79]. Nevertheless, the fuel specific behavior does not change with cross-section geometry.

5.4.4   Full Burner Imaging

The culmination of atmospheric pressure measurements was the visualization of combustion in the full burner for the complement of fuels. The square cross-section quarl and combustion liner were attached to the burner. As above, the burner throat velocity and combustor inlet temperature were 60 m/s and 650 K respectively. The flow field was imaged with PIV for combusting cases, and OH-PLIF images were collected separately for equivalent operating points. The results, shown in figure 5.8, depict the velocity field of the left half of the

combustion liner abutted to the average OH-PLIF image for the right half of the combustion liner. The color-bars shown to the side of the images give the velocity value, while the arrows show the direction of flow. Intensity for the OH-PLIF measurement is arbitrary, low OH signal shown in blue to highest signal in red. The measurements are taken approximately 10 mm from the transition of the quarl to the square combustion liner. The OH-PLIF images have been corrected for laser sheet energy distribution. The measurements for dilute methane, syngas and dilute syngas had poor signal-to-noise ratios toward the bottom of the measurement region due to low laser energy. The results of this experiment have been used in papers A and B [80, 81].

In turbulent combustion the recirculation of the hot combustion products into the oncoming gas flow provides ignition for the unburnt charge of fuel and air. Combustion stabilizes at positions where the incoming fuel has slowed and heated sufficiently for combustion. The flame front and much of the recirculation zone are blocked from visual access by the quarl, what is seen here is the upper end of the recirculation zone. As a result, both the velocity field and the OH-LIF signal appear to continue downwards past the limit of the measurement region. The PIV measurements illustrate the expected flow regions of a recirculating combustion region: a high forward velocity along the outer wall, a central recirculation zone and the stagnation plane at the interface of these two. Though all test conditions featured the same throat velocity, the peak velocities recorded for the non diluted case are somewhat slower than that of the two nitrogen diluted fuels. OH-PLIF distribution is reasonable in consideration of the flow contours; OH signal is lacking in the highest velocity regions at the lower corner of the combustion chamber, and the signal decreases at the center of the recirculation zone which is far from the production regions at the stagnation plane.
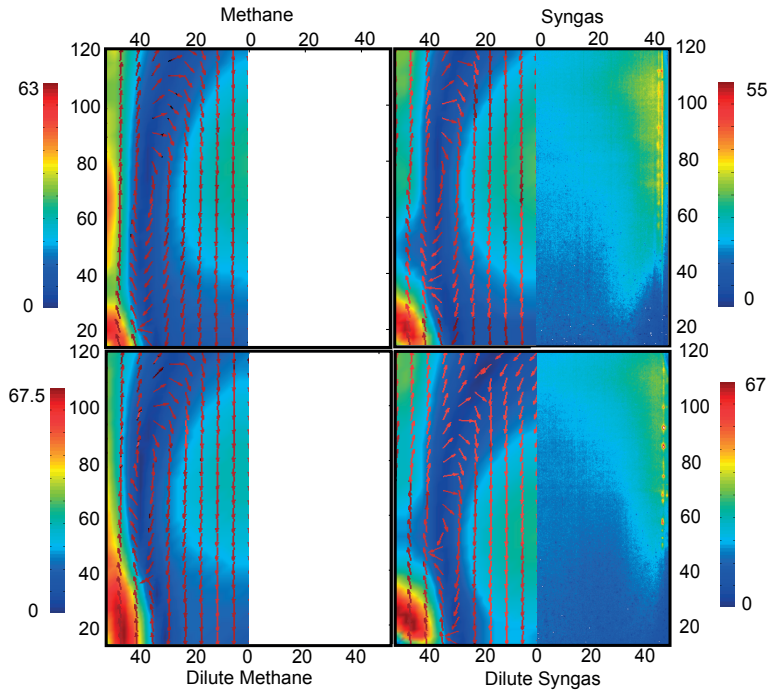
Figure 5.8: Full burner combustion for 4 fuels; flow field in left half of image and OH-LIF in right. Vectors indicate direction of flow, velocity is indicated respective to colorbars in m/s.

ELEVATED PRESSURE COMBUSTION

Many arguments are possible for the use of atmospheric pressure over elevated pressure experiments; however, none of these arguments can eliminate the fact that many practical combustion systems operate at elevated pressure. There are changes to the combustion characteristics- density, heat loss, flame thickness, etc., the effects of which will only be exhibited by testing under pressure.

6.1 Elevated Pressure Facility

The high pressure facility at Lund University Combustion Center allows for testing of gas turbine components at relevant conditions with regard to mass flow and pressure. The facility has capacity for 1 MW power output, 16 bar pressure and 1.3 kg/s air flow and 1100 K combustor inlet temperature. A probe is situated at the exit of the combustion chamber providing sampling of the combustion emissions.

A prominent feature of the elevated pressure rig is the optical access afforded to the combustor. A cutaway image, illustrating the mounting of the pilot sector and various optical components used for measurements, is shown in figure 6.1. The combustion chamber is 60 cm in length and has a 100 cm^2 cross section. The first 150 mm section of the combustion chamber has quartz windows set into three of the four faces in order to allow laser measurements of the combustion region. The windows in the inner shell of the combustion chamber are 40 mm x 100 mm while the outer shell uses windows that are 100 mm square. The left and right sides of the combustion chamber, through which the laser was passed, feature one window per side with long axis parallel to the flow axis of the chamber. The top face holds two windows side by side so that the 40 mm axis lies parallel to the flow. In total an approximately 50 mm wide portion of the combustion region was visible through these windows.

6.2 Laser Diagnostics at Elevated Pressure

6.2.1 Pilot Sector Operation on Syngas Fuels

The pilot sector was mounted in the elevated pressure facility using the mounting adapter shown in figure 4.3. This was done to generate a better understanding of the role of the pilot sector in stabilizing combustion in the intermediate
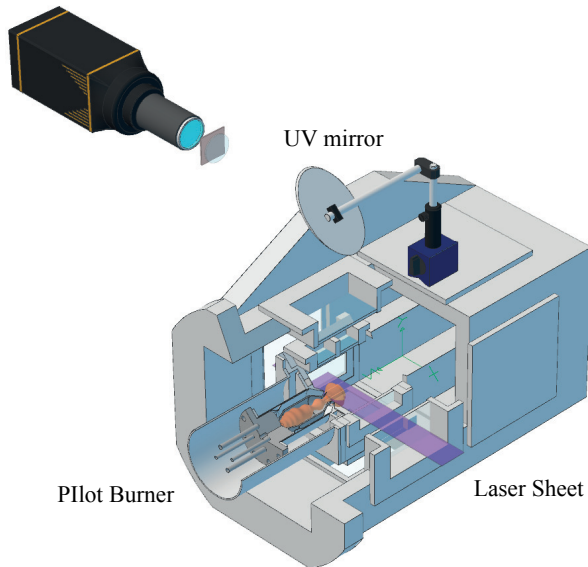
UV mirror

PIlot Burner

Laser Sheet

Figure 6.1: Elevated pressure combustion chamber with pilot burner in place. The 50 mm laser sheet enters from the right of the image, passing by the dump plane of the burner. OH-LIF signal passes out the top windows of the combustion chamber and outer liner, reflecting off an angled mirror and imaged by a Princeton Instruments ICCD camera.

and main burner sectors, as well as the effects of fuel and pressure on the pilot sector combustion. Imaging of OH-PLIF was performed while operating the burner on the four selected fuels at pressures of 3, 6 and 9 bar. The pilot sector residence time, inlet temperature and surrounding flow velocity was the same as used in the atmospheric measurement of the pilot sector for methane, section 5.4.1. The full presentation of the experiment is found in paper I, and results were used in paper C [82].

Examples of three distinct OH-LIF distributions were observed, shown in figure 6.2. These distributions were labeled diffuse-attached, diffuse-detached, and hollow-attached after there general appearance. The occurrence of these characteristic OH LIF distributions was found to be linked to the fuel type and the equivalence ratio. At lean equivalence ratios the diffuse-attached distribution was present for all fuels and at all pressures. The diffuse-detached distribution is only found for syngas fuels at rich equivalence ratios. Attached-hollow OH-LIF distribution occurs at rich equivalence ratios of methane and possibly at the very highest equivalence ratio for syngas.

The explanation for the diffuse-attached OH-PLIF distribution is likely the same as for the lean measurements taken for methane combustion in the pilot sector, section 5.4.1. The OH molecule is produced by a flame that is fully inside the pilot sector. Thus the OH becomes evenly distributed in the post combustion products before being carried out of the pilot. In the diffuse-detached and hollow-attached forms, which are both present at rich equivalence ratios, it is probable that combustion occurs both to some extent within the body of the pilot sector and outside. In the case of the diffuse-detached OH-LIF conformation the pilot sector does not support flame attachment, so combustion begins some distance downstream, after air has diffused into the partially reacted fuel. If this is indeed the case, it would be similar to the stoichiometric mixture for the atmospheric experiments, where combustion crossed through the pilot sec-
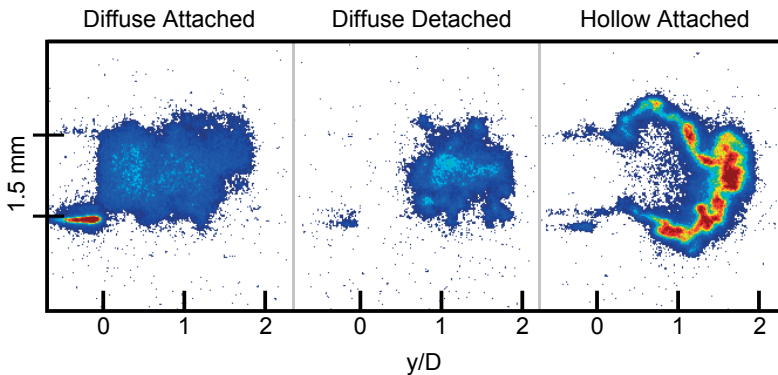

Figure 6.2: Single shot images of the three characteristic OH-LIF distributions from the pilot sector. Flow from left to right, laser enters from the bottom. Scale is uniform for all images, with blue being the lowest intensity, red the highest.

tor exit giving a v shaped flame brush. However, it would appear that due to the pressure, or the type of fuel, the flame quenches before transiting the pilot sector exit and reignites as a sort of lifted flame after the burner exit. The hollow-attached OH distribution, which is present for rich methane mixtures, is similar to the same fuel and equivalence ratio in section 5.4.1, where excess fuel establishes a non-premixed flame at the lip of the pilot sector exit.

There are several general observations that can be made from elevated pressure testing of the pilot sector. The pressure did not have a great effect on the conformation of the OH-PLIF distribution, other than diminishing the width of the distribution and diminishing the signal. The combustible components again appeared to have more effect on the signal shape than the actual energy content. The equivalence ratio had the greatest effect on the OH-signal distribution.

6.2.2 Full Burner Operation with Nitrogen Diluted Natural Gas

The final experiment performed with the prototype burner was OH-PLIF imaging of combustion using variations of natural gas diluted with nitrogen to Wobbe indices of 45, 40 and 30 MJ/m^3 (45 MJ/m^3 being normal natural gas). Fuels with some component of inert gas are of interest to gas turbine users that may have access to air blown gasification gas or process gas. The burner was operated at 3, 4.5 and 6 bar pressures. Fuel flow rates were chosen to produce an adiabatic flame temperature of 1800 K, with air flow preheated to 650 K. The intermediate sector equivalence ratio was maintained at 1.3 times the main sector equivalence ratio as this helped to stabilize combustion. A portion of these measurements were used in paper C [82].

Results of the experiment are shown in figure 6.3. The measurement region is located just after the quarl, similar to the atmospheric measurements in section 5.4.4. The OH-LIF distribution is similar to atmospheric measurements, showing low intensity in the corners of the combustion chamber closest to the burner and signal continuing into the quarl. The images show little variation in the OH signal distribution between the three fuels. This is not unexpected, as the flame temperature was the same for all fuels, which requires increases in the fuel flow as the energy content decreases. Increasing pressure does not show a large influence on the average of the OH-LIF distribution either, other than the expected decrease in intensity as the pressure increases.
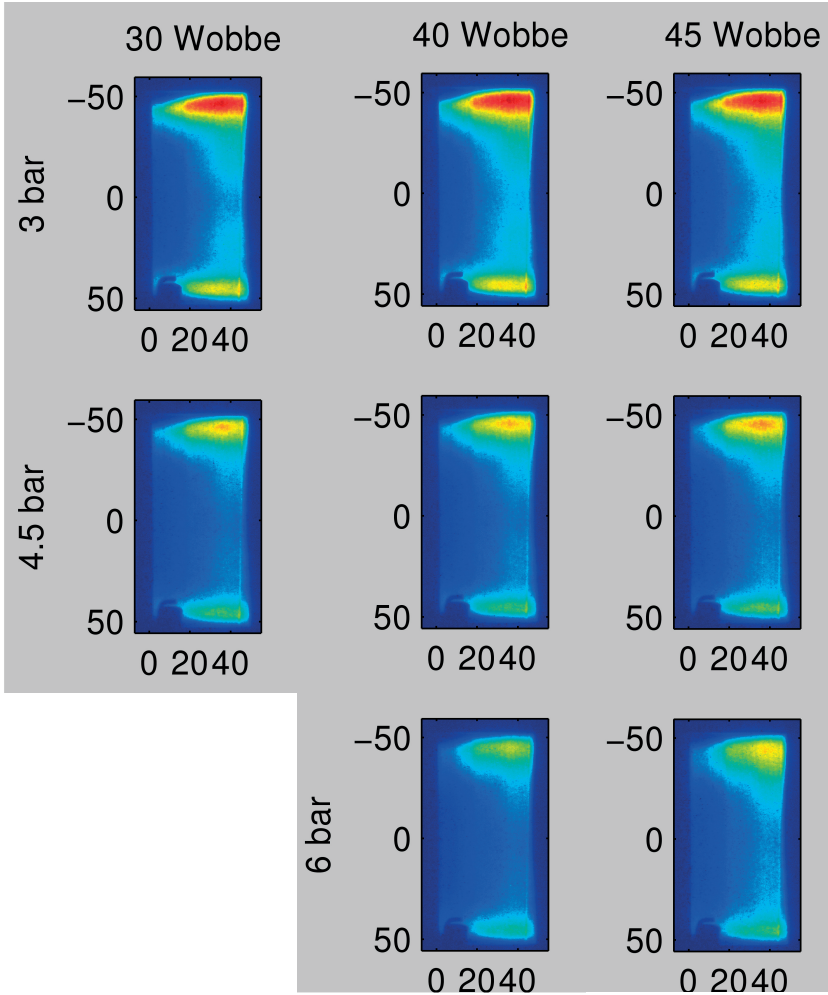
Figure 6.3: Elevated pressure testing of DLE burner using natural gas of various energy content after dilution with nitrogen. Burner is at left of the image region, laser sheet enters from the bottom. Scale is uniform for all images, with blue being the lowest intensity, red the highest.

SUMMARY

This thesis presented the integration of an industrial prototype gas turbine DLE burner in atmospheric and elevated pressure experimental facilities for the purpose of investigating the burner while using syngas fuels. The overarching goal of research was the collection of data regarding the combustion of syngas fuels in the burner for comparison with CFD generated models. Work was performed at atmospheric and elevated pressure and measurements were made at 300 K and gas turbine relevant temperatures, 500–650 K. The following results were generated:

- Laminar flame speeds of syngas fuels were evaluated at gas turbine relevant temperatures. This gave a practical understanding of the dissimilar combustion characteristics of the fuels and provided data for validation of reaction mechanisms used by modelers.

- The effect of burner staging on emissions levels was evaluated for several fuels. It was found that the largest contribution to NOx emission was the burner pilot sector which operated near stoichiometric equivalence ratios.

- Combustion from the pilot sector was investigated directly by imaging the flame chemiluminescence and OH-PLIF at 1, 3, 6 and 9 bar pressure. Signal distributions were found to be influenced by equivalence ratio and type of fuel. It was proffered that the ability to sustain combustion inside the pilot chamber determined the OH distribution observed from the pilot sector.

- The effect of combustion chamber configuration on flame location was investigated. Flame in the circular cross-section combustion chamber was found to be more limited to the center of the chamber and feature more inclusions in the flame edge than for equivalent operating conditions in the square cross-section combustion chamber. The trends between the different fuels were the same however, with syngas burning more closely to the chamber wall with smaller inclusions than methane.

- Flow structures in the combustion chamber were visualized with PIV during combustion at atmospheric pressure for four fuels. OH-PLIF imaging of the combustion region was collected at the equivalent operating conditions.

- The OH-PLIF signal was imaged while operating the DLE burner with 30, 40 and 45 MJ/m^3 methane fuels at 3, 4.5 and 6 bar pressure.

7.1 Future Considerations

Establishing the gas turbine burner in the atmospheric and elevated pressure facilities was a monumental undertaking. The published work limited by what we were able to do rather than what we would like to have done. There are some things that should be improved in the measurement approach: laser beam quality was not good, which resulted in low signal-to-noise in portions of the OH-LIF images. An ignition system needs to be fit to the atmospheric facility both for safer operation and for consistent location of laser reflections. Adding pressure and temperature transducers could add value to the measurements. From an experiment standpoint, if I were able to begin at this point and move forward I would like to investigate the following things:

- Optical access to the flame front is obstructed by the conical expansion. While this is necessary to support the swirling flow of the burner it also blocks access to the regions which would show greatest variability. Laser access to this region could be enabled by cutting a slit in the conical expansion.

- Greater height of the laser sheet is needed to illuminate the full combustion region. The distance from the onset of combustion, if access to the quarl were possible, to the top of the recirculation zone would require a laser sheet approximately 200 mm in height. To create such a laser sheet, with even energy distribution, would require a high power laser system. Alternatively it would be possible to arrange stacked laser sheets by using the multi-YAG system with a series of dye lasers.

- As it is possible to perform LIF measurements in a circular cross-section combustion liner it would be worthwhile to investigate a liner with an aspect ratio more similar to a true gas turbine combustor. While direct PIV measurements are not possible due to laser reflection in the chamber walls, a phosphorescent particle may avoid this. Otherwise, the multi-YAG system could be used to image the velocity of the flame front fluctuation.

- Advances in laser technology should be applied in the form of updating the mature techniques to high speed or volumetric measurements.

- Temperature mapping has been the holy grail of combustion diagnostics for decades, yet the systematic application to complex environments is absent. Advances in seeding techniques such as the TMI indium source that was developed for paper V could be implemented to practical combustion environments.

- In general the field of laser-based combustion diagnostics would benefit from standardized measurement and data processing techniques, especially in case of application to complex combustion environments.

CHAPTER 8

ACKNOWLEDGMENTS

Thank God I made it this far!

Studying in a foreign country can be intimidating, as one encounters different customs, bureaucracy and cultural norms. Those who have shared in my life the last five years have heard of the various challenges, excitements and comedic events that peppered my time here. In light of this I can offer this highest praise: I saw the Combustion Physics department as a place of welcome. I knew that I would be received with kindness and as a respected colleague when I passed through the doors to Enoch Thulin building. This type of environment is unique and does not occur without practiced intent.

I would like thank my advisers for their direction and support during the past five years. Professor Aldén, I appreciate that you have been accessible to me during my time here. More than that you have encouraged me to be good at being the scientist that I am. I think that at times you have had more faith in my ability than I have. Professor Klingmann, you have repeatedly explained to me without condescension the vagueries of this thing called flow. And turbulence. And mixing. And combustion modelling. That list could continue on ad nauseum. Dr. Li you have been great help both in the lab, fixing broken lasers, and out. Taking the time to argue with me about the projects when we had different understandings meant a lot. Dr. Collin, I cannot imagine your task was easy. Five years ago I am not sure that either of us knew what to do with each other. I was clueless and motivated which must not have made your job easy. As time has gone by, I think we have both improved in our roles.

The combustion physics division just wouldn't function without the tireless work of Minna Ramkull and Cecilia Bille. I am convinced that these two work harder and know more than most of us put together. Rutger Lorensson, när jag visste att jag kunde komma ned och prata skit om bilen och rolig antika saker som de "vanliga" tror är sopor vägde mitt arbete lite mindre tungt på axlarna. Jag kommer ihåg att du också hade något att göra med mekaniska saker i labbet. Vi hade inte kunnat laga saker, bygga maskindelar eller sköta riggen utan dig. Igor Buzuke I may not have been the first to ask for help with electronic problems, but I appreciate both that you let me invade the electronics shop to fix my stuff, and that you encouraged me, sometimes, in my lunacy. Lennart Ostermann, without your help I could not have kept the backup server running long enough for Igor to come and fix it.

Finally I would like to thank the coworkers that have shared my office space and lab space in the past five years. Zhiwei Sun impressed me constantly with

his hard work and intelligence. Andreas Lantz, the first day we worked together you lit your arm on fire. You have shown marked improvement from that day. Thank you for introducing me to fluorescence and hours in the lab struggling with things that unfortunately did not work out. To my successors in the Turbokraft project, Arman Subash and Atanu Kundu- good luck! We did the easy stuff and now you can do the interesting stuff. Abdoulah Abou-Taouk, much of the understanding I have about our burner is based on your modeling, thank you for your high quality work. To my closest coworker these last four years, Ivan Sigfrid, since you graduated I realize how much work you did, that I never knew about. I think that we worked well together, I cannot remember a single heated argument. I can say that without your help I would not have gotten so much done. Thank you.

Anna, you have been amazing! You have likely read this thesis more thoroughly than I have myself. Your dinners, surprise visits and encouragement have helped carry me through these past months. Thank you.

CHAPTER 9

SUMMARY OF PUBLICATIONS

Paper I

"Investigation of a Premixed Gas Turbine Central Body Burner using OH Planar Laser Induced Fluorescence at Elevated Pressures" Whiddon, R., Sigfrid, I. R., Collin, R. and Klingmann, J.
ASME TurboExpo 2013 conference proceedings GT2013-94443

The pilot component of a gas turbine burner is investigated with pLIF at elevated pressure using four fuels: methane, methane diluted with nitrogen, a synthetic gas blend and a nitrogen diluted synthetic gas blend. The purpose of the investigation was to visualize the post burner OH distribution for the fuels, and any effects pressure would have on that OH distribution. Images of the OH distribution in conjunction with temperature measurements along the combustion chamber wall suggest a change in the extent of the flame distribution in the combustion chamber that was ϕ and fuel dependent.

In addition to authoring this paper, I was responsible for the laser based measurements and data processing of the resulting OH-pLIF data. Dr. Sigfrid calculated the experimental flow parameters and assisted in writing the paper. Dr. Collin assisted with operating the High pressure facility. Professor Klingmann and Dr. Collin oversaw completion of the article.

Paper II

"Experimental Investigation of Lean Stability of a Prototype Syngas Burner for Low Calorific Value Gases" Sigfrid, I. R., Whiddon, R., Alden, M. and Klingmann, J.
ASME Turbo Expo 2011 conference proceedings GT2011-45694

The lean stability limit of an experimental low emission burner was investigated at atmospheric pressure. The tests featured four fuels: methane, low calorific content methane/nitrogen, hydrogen/carbon monoxide/methane syngas and low calorific content hydrogen/carbon monoxide/methane/nitrogen fuels. The CO emission was used as an indicator of the onset of flameout. The onset of flameout was tested at a range of equivalence ratios of a central stabilizing pilot. In all cases the stability limit is improved by running the central

stabilizing flame at high equivalence ratios. *Note on error-* due to the miscalculation of viscosity for the syngas and dilute syngas fuels the mass flow values were reported 20% higher than actual. For correction, the equivalence ratio and mass flow values reported should be multiplied by 0.8 for these two fuels.

I was responsible for creating the burner control program, worked together with Dr. Sigfrid to collect data and contributed to the article. Dr. Sigfrid was the primary author and responsible for experimental parameters, data processing and presentation of the results. Professors Aldén and Klingmann oversaw completion of the article.

Paper III

"Parametric Study of Emissions from Low Calorific Syngas Combustion, with Variation of Fuel Distribution, in a Prototype Three Sector Burner" Sigfrid, I. R., Whiddon, R., Aldén, M. and Klingmann, J.
ASME Turbo Expo 2011 conference proceedings GT2011-45689

Variation in the NOx and CO emissions with respect to changes in fuel distribution between the three sections of an experimental low emission burner was recorded. A target global equivalence ratio was maintained while the fuel was partitioned selectively to the intermediate and main burner sections. Also, a stabilizing central pilot burner was varied in equivalence ratio. It was found that the due to scales of flow, biasing the fuel flow to the main burner sector lowered NOx emissions. The stabilizing central pilot was found to have a strong contribution to the total NOx level, due to higher equivalence ratio despite being only a small proportion of total fuel flow. *Note on error-* due to the miscalculation of viscosity for the syngas and dilute syngas fuels the mass flow values were reported 20% higher than actual. For correction, the equivalence ratio and mass flow values reported should be multiplied by 0.8 for these two fuels.

I was responsible for creating the burner control program and assisted in data collection, data processing and contributed to the article. Dr. Sigfrid was the primary author and responsible for the experimental parameters and data processing. Professors Aldén and Klingmann oversaw completion of the article.

Paper IV

"Experimental Investigation of Laminar Flame Speeds for Medium Calorific Gas with Various amounts of Hydrogen and Carbon Monoxide Content at Gas Turbine Temperatures." Sigfrid, I. R., Whiddon, R., Collin, R., Klingmann, J.
ASME Turbo Expo 2010 conference proceedings GT2010-22275

The laminar flame speed of methane and five synthetic gases were measured at gas turbine relevant temperatures using the conical flame half angle method.

The flame was imaged with a Schlieren imaging setup. The burner flow field was quantified with PIV to correct for a non uniform flow velocity. The laminar flame speeds were corrected for flame stretch

I was responsible for setting up the Schlieren imaging system, data processing of the images and fitting of the flame half angles. I contributed to the article. Dr. Sigfrid was the primary author and responsible for PIV imaging experiments, consequent flow field analysis and devising the method to correct for flame stretch. Professor Klingmann and Dr. Collin supervised writing.

Paper V

"Trimethylindium as an Indium Source for Combustion Experiments" Whiddon, R., Zhou, B. Borggren, J. and Li, Z. S
manuscript in preparation

A means of seeding indium into a premixed flame was devised and constructed. Trimethylindium was used as the indium carrier molecule due to a vapor pressure to potentially seed indium at measurable levels in the test burner. The seeding system was evaluated for its linearity of response using the emission from two prominent atomic transitions. The results were rather linear above 5 ppm seeding level, with self absorption being a problem at high seeding concentrations. Laser absorbance and fluorescence measurements show a low seeding efficiency, but similar trends in self absorption and linearity. Several indium molecules that show band structures in red/orange spectral region were observed when seeding was applied to a nitrogen flow heated by a surrounding flame.

I was primary author on this paper and responsible for the design and construction of the seeding apparatus. B. Zhou and I performed the measurements for linearity of response based on emission level. J. Borggren and B. Zhou collected the laser absorption and fluorescence images. B. Zhou collected the spectra of indium molecules in the inert carrier flow. Dr. Li worked with revising the manuscript and provided oversight in the document production.

Paper VI

"Laser-Based Investigation of a Gas Turbine Pilot Burner Combustion with Variation of Equivalence Ratio, Residence Time and Cooling Flow Temperature." Whiddon, R., Kundu, A., Subash, A. A., Collin, R., Aldén, M. and Klingmann, J.
manuscript in preparation

The inclusion of rich stabilizing pilot burners in premixed gas turbine combustors is a means of stabilizing potentially damaging combustion fluctuations

while running at lean conditions. These are interesting parts of the combustor as, though they have a fraction of the combustion volume of the turbine combustor at large, they can contribute significantly to emissions. In this paper observations were made of the spatial distribution of OH LIF signal for different reaction variables: equivalence ratio, temperature of a cooling flow and the non reacting residence time in a partially enclosed combustion environment. Additionally, the emissions of various combustion products and the temperature distribution in the burner body were monitored at the experimental points. The goal of the work is to understand the contributions of an enclosed pilot burner to the stable combustion of a larger burner assembly, and to investigate emissions at different combuster loadings. In completion of this work, a well defined measurement set was collected for comparison with CFD modeling studies.

I was the primary experimenter and author of this paper. A. A. Subash and A. Kundu assisted with data collection. A. A. Subash was responsible for processing the OH-pLIF and Chemiluminescence images. A. Kundu processed the emissions data. Manuscript progress is supervised by Dr. Collin and professors Aldén and Klingmann.

APPENDIX 1

Atmospheric Burner Control Program

This program enables the safe operation of a burner in the atmospheric testing facility. The program provides for control of up to four mass flow controllers connected to the computer via the RS-232 ports located in the RS-232 interface/power block. The program interfaces with the bulk air blowers using the analog output of the Vellemen USB/DAQ project board located behind the VA-CONN power control unit. Bulk air mass flow is interfaced through the analog input ports of the Velleman USB/DAQ project board. Temperature probes are logged through the Agilent datalogger which is connected via a second RS-232 port. If a Kistler pressure probe is being used, attachment should be made to the high-speed National Instruments DAQ. There is no provision for control of the inline air heaters at this time.

System Startup

- Check that mass flow controller lines are secured to the RS-232 interface/power control unit and that the control unit is turned off.

- Ensure that the area is clear of all fire dangers and that cords are clear from walkways.

- Turn on the high volume exhaust system.

- Turn on the power to the VACONN AC frequency controller.

- Turn on power to the air mass flow meters, mass flow controllers and the Agilent data logger.

- Boot the computer and load the Atmospheric Burner Control Program, clicking run.

- In the small setup screen (figure 10) select the RS-232 port for the Agilent Data logger. If correct, the green "connected" indicator should light.

- In the mass flow controller frame select the RS-232 port for the RS-232 interface/power block. Make any changes necessary to the flow range and gas and then click populate. You will be alerted of any non connected MFC ports.

- Check that the green "connected" indicators are lit for all necessary items. Then click exit. (note, exit will only become enabled when after the populate button is pressed.)

- After a short time the system should start cycling with an audible trigger.

Running Experiments

The running screen Figure 10 is dominated by the two charts in the upper left hand side. The topmost is the measurement of thermocouples in the burner, inlet, preheater and exhaust. These values update at 1 Hz intervals. Below this chart is the Kistler pressure probe graph. It is normally in a non-recording state, by clicking on "Trace on" the probe will be activated. This graph updates in 1 second intervals, though the detector collects data at 100 kHz.

Flow rates for the bulk air flow are in the middle bottom of the screen. The horizontal slider, or the numerical input box may be used to enter the desired blower speed setting (0-100%). After setting the value correctly click the check box marked "update". The measured values for flow in g/s are shown below the horizontal slider. From left to right they are the flow rate in blower 1, blower 2 and the total bulk air flow rate. The flow setting and flow rates are updated at 10 Hz.

The mass flow controllers for fuel or air are shown on the right half of the screen. The sequence of controllers is the same as the sequence entered in the setup panel. To change values, use either the vertical slider or the numerical input box to select the desire value. To update the value click the check box labeled "Modify" for the selected mass flow controller and then click "Update MFC" The "connected" indicator should switch from green to red momentarily while the value is updated. Flow controller read values are shown in their respective box to the right of the vertical control slider. Calculated equivalence ratios are shown in numerical output boxes situated in the center of the screen. These values are calibrated for methane only. Contact the author if you wish to learn how to change the fuel. These values update at 4 Hz.

Utility buttons are located at the bottom left of the screen. Clicking the "Record" button will invoke a file save interface where you enter the name of the measurement file. The button will be replaced with a progress bar. All files are stored in a CSV format. The "Setup" button may be used to alter the flow range or gas type of the mass flow controllers, or change the RS-232 port of the Agilent data logger. Again, you must click populate once before being able to exit the setup program. The "STOP" button will shut down all flows and finalize any data saving processes before exiting the program. The "Kill" button is used in case of emergency. It will only shut down the fuel flows, but not the bulk air flow. Two small error indicators in the bottom left alert if the connection has been lost to the Agilent data logger or the log file.

System Shutdown

- Extinguish any flame by manually shutting off the fuel flow, or clicking the "kill" button.
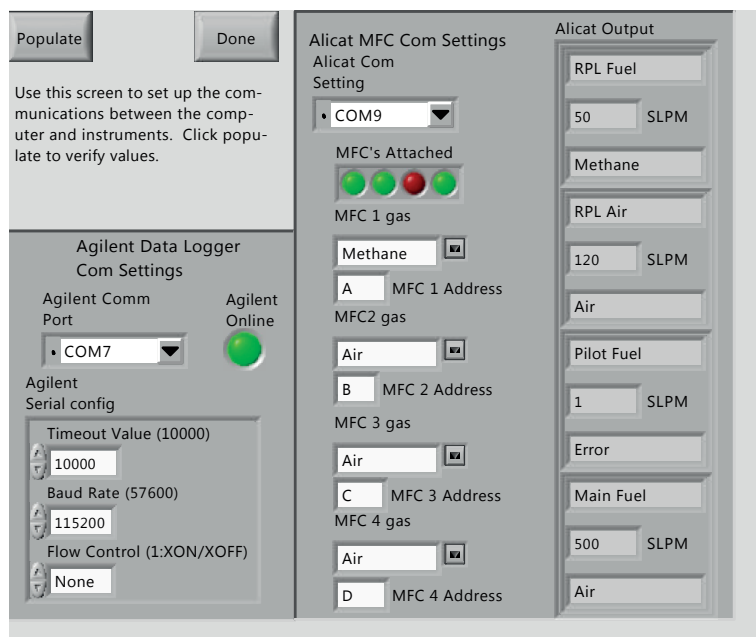
Figure 10.1: Atmospheric Burner Control Program, setup panel.

- Turn off any heating systems that have been energized.

- Shut off gas bottles at the bottle by closing the main valve, not the regulator.

- After allowing the burner to cool sufficiently, turn on each of the mass flow controllers shortly, one at a time, to vent the pressure in the feed lines.

- When the temperature of the burner is cooled safely, click on the "STOP" button. This will ensure that all flows are closed.

- Turn off power to the mass flow controllers, Agilent data logger and the mass flow meters.

- Shut down the computer after removing any desired files.

- Turn off the VACONN AC frequency controller. (This will most likely trip the room circuit breaker.)

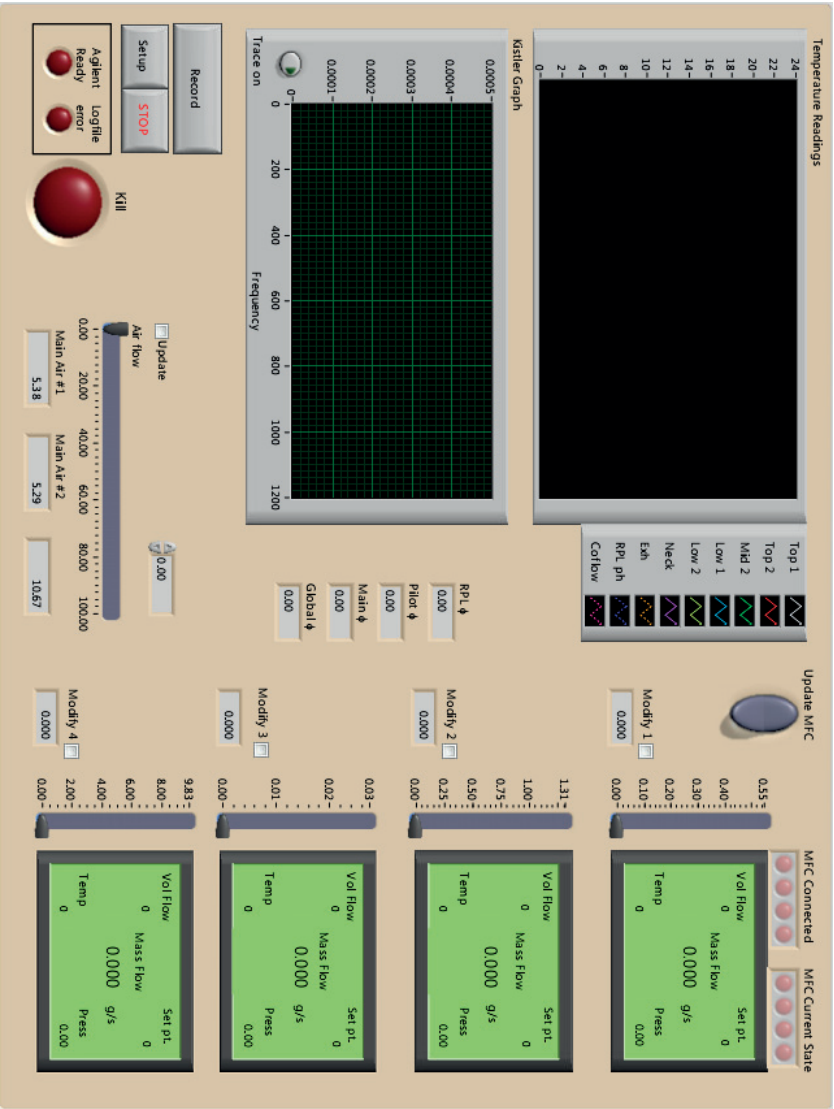- Shut down the high volume exhaust system before leaving for the day.

Figure 10.2: Atmospheric Burner Control Program, main panel.

Bibliography

[1] White, L. E., 1943. "Energy and the Evolution of Culture". *American Anthropologist,* **45**(3), pp. 335–356.

[2] Secretariat, P., 2012. Renewables 2012 Global Status Report. Tech. rep., United Nations Environmental Programme.

[3] Hoffert, M. I., Caldeira, K., Benford, G., Criswell, D. R., Green, C., Herzog, H., Jain, A. K., Kheshgi, H. S., Lackner, K. S., Lewis, J. S., Lightfoot, H. D., Manheimer, W., Mankins, J. C., Mauel, M. E., Perkins, L. J., Schlesinger, M. E., Volk, T., and Wigley, T. M. L., 2002. "Advanced Technology Paths to Global Climate Stability: Energy for a Greenhouse Planet". *Science,* **298**(5595), pp. 981–987.

[4] EPA-452/R-13-003, 2013. Regulatory Impact Analysis for the Proposed Standards of Performance for Greenhouse Gas Emissions for New Stationary Sources: Electric Utility Generating Units. Tech. rep., United States Environmental Protection Agency.

[5] Lefebvre, A. H., 1999. *Gas Turbine Combustion.* Taylor & Francis.

[6] Ditchburn, R. W., 1991. *Light.* Dover Publications, Mineola, New York.

[7] Garbuny, M., 1965. *Optical Physics*, international ed. Academic Press, New York.

[8] Svanberg, S., 2004. *Atomic and Molecular Spectroscopy.* Advanced Texts in Physics. Springer Berlin, Heidelberg.

[9] Banwell, C., and McCash, E., 1994. *Fundamentals of Molecular & Spectroscopy.* McGraw-Hill Education (India) Pvt Limited.

[10] Eckbreth, A. C., 1996. *Laser Diagnostics for Combustion Temperature and Species*, second ed. Gordon and Breach, Amsterdam.

[11] Herzberg, G., 1944. *Atomic Spectra & Atomic Structure.* Dover Publications, New York.

[12] Schawlow, A., and Townes, C., 1958. "Infrared and Optical Masers". *Physical Review,* **112**(6), Dec., pp. 1940–1949.

[13] Maiman, T. H., 1960. "Stimulated Optical Radiation in Ruby". *Nature,* **187**(4736), Aug., pp. 493–494.

[14] Geusic, J. E., Marcos, H. M., and Van Uitert, L. G., 1964. "Laser Oscillations in Nd-doped Yttrium Aluminum, Yttrium Gallium and Gadolinium Garnets". *Applied Physics Letters,* **4**(10), p. 182.

[15] Maslow, A. H., 1966. *The Psychology of Science: A Reconnaissance.* Maurice Bassett.

[16] Aldén, M., Bood, J., Li, Z., and Richter, M., 2011. "Visualization and Understanding of Combustion Processes using Spatially and Temporally Resolved Laser Diagnostic Techniques". *Proceedings of the Combustion Institute,* **33**(1), pp. 69–97.

[17] Sigfrid, I. R., Whiddon, R., Collin, R., and Klingmann, J., 2013. "Influence of Reactive Species on the Lean Blowout Limit of an Industrial DLE Gas Turbine Burner". *Combustion and Flame,* **161**, May, pp. 1365–1373.

[18] Schefer, R. W., 1997. "Flame Sheet Imaging Using CH Chemiluminescence". *Combustion Science and Technology,* **126**(1-6), pp. 255–279.

[19] Nori, V., and Seitzman, J., 2007. "Chemiluminescence Measurements and Modeling in Syngas, Methane and Jet-A Fueled Combustors". In 45th AIAA Aerospace Sciences Meeting and Exhibit, Aerospace Sciences Meetings, American Institute of Aeronautics and Astronautics.

[20] Libby, P. A., and Williams, F. A., 1976. "Turbulent Flows Involving Chemical Reactions". *Annual Review of Fluid Mechanics,* **8**(1), Jan., pp. 351–376.

[21] Raffel, M., Willert, C. E., Wereley, S. T., and Kompenhans, J., 2007. *Particle Image Velocimetry,* second ed. Experimental Fluid Mechanics. Springer Berlin Heidelberg, Berlin, Heidelberg.

[22] Nichols, E. L., and Howes, H. L., 1923. "The Photoluminescence of Flames". *Physical Review,* **22**, pp. 425–431.

[23] Nichols, E. L., and Howes, H. L., 1924. "The Photoluminescence of Flames. II". *Physical Review,* **23**, Apr, pp. 472–477.

[24] Winefordner, J., and Vickers, T., 1964. "Atomic Fluorescence Spectroscopy as a means of Chemical Analysis.". *Analytical Chemistry,* **36**(1), pp. 161–165.

[25] Alkemade, C. T. J., 1970. "A Theoretical Discussion on some aspects of Atomic Fluorescence Spectroscopy in Flames". *Pure and Applied Chemistry,* **23**(73).

[26] Joklik, R. G., and Daily, J. W., 1982. "Two-line Atomic Fluorescence Temperature Measurement in Flames: an Experimental Study". *Applied Optics,* **21**(22), pp. 4158–4162.

[27] Browner, R., and Winefordner, J., 1972. "Measurement of Flame Temperatures by a Two-line Atomic Absorption Method". *Analytical Chemistry,* **44**(2), pp. 247–252.

[28] Aldén, M., Grafström, P., Lundberg, H., and Svanberg, S., 1983. "Spatially Resolved Temperature Measurements in a Flame using Laser-excited Two-line Atomic Fluorescence and Diode-array Detection". *Optics Letters,* **8**(5), pp. 241–243.

[29] Haraguchi, H., Smith, B., Weeks, S., Johnson, D. J., and Winefordner, J. D., 1977. "Measurement of Small Volume Flame Temperatures by the Two-line Atomic Fluorescence Method". *Applied Spectroscopy,* **31**(2), Mar., pp. 156–163.

[30] Wolff, D., Schlüter, H., Beushausen, V., and Andresen, P., 1993. "Quantitative Determination of Fuel Air Mixture Distributions in an Internal Combustion Engine using PLIF of Acetone". *Berichte der Bunsengesellschaft für physikalische Chemie,* **97**(12), pp. 1738–1740.

[31] Bazile, R., and Stepowski, D., 1995. "Measurements of Vaporized and Liquid Fuel Concentration Fields in a Burning Spray Jet of Acetone using Plaser Laser Induced Fluorescence". *Experiments in Fluids,* **20**(1), pp. 1–9.

[32] Yip, B., Miller, M., Lozano, A., and Hanson, R., 1994. "A Combined OH/Acetone Planar Laser-induced Fluorescence Imaging Technique for Visualizing Combusting Flows". *Experiments in Fluids,* **17**(5), pp. 330–336.

[33] Johansson, I., and Litzen, U., 1967. "The Term Systems of the Neutral Gallium and Indium Atoms Derived from New Measurements in the Infrared Region". *Arkiv Fysikum,* **34**, p. 573.

[34] Nygren, J., Engström, J., Walewski, J., Kaminski, C. F., and Aldén, M., 2001. "Applications and Evaluation of Two-line Atomic LIF Thermometry in Sooting Combustion Environments". *Measurement Science and Technology,* **12**(8), Aug., pp. 1294–1303.

[35] Kohse-Höinghaus, K., 1994. "Laser Techniques for the Quantitative Detection of Reactive Intermediates in Combustion Systems". *Progress in Energy and Combustion Science,* **20**(3), pp. 203 – 279.

[36] Daily, J. W., 1997. "Laser Induced Fluorescence Spectroscopy in Flames". *Progress in Energy and Combustion Science,* **23**(2), Jan., pp. 133–199.

[37] Stepowski, D., 1999. "Planar Optical Measurement Methods for Gas Turbine Components". *Series, RTO Lecture*, pp. 6–1–6–18.

[38] Aldén, M., Edner, H., Holmstedt, G., Svanberg, S., and Höberg, 1982. "Single-pulse Laser-induced OH Fluorescence in an Atmospheric Flame, Spatially Resolved with a Diode Array Detector". *Applied Optics,* **21**(7), pp. 1236–1240.

[39] Probert, R. P., and Singham, J. R., 1946. "The Measurement of Gas Temperatures in Turbine Engines". *Journal of Scientific Instruments,* **23**(4), Apr., pp. 72–77.

[40] Omenetto, N., Benetti, P., and Rossi, G., 1972. "Flame Temperature Measurements by means of Atomic Fluorescence Spectrometry". *Spectrochimica Acta*, **27B**, pp. 453–461.

[41] Cattolica, R., 1981. "OH Rotational Temperature from Two-Line Laser-Excited Fluorescence". *Applied Optics*, **20**(7), pp. 1156–1166.

[42] Devillers, R., Bruneaux, G., and Schulz, C., 2008. "Development of a Two-line OH-laser-induced Fluorescence Thermometry Diagnostics Strategy for Gas-phase Temperature Measurements in Engines". *Applied Optics*, **47**(31), Oct., p. 5871.

[43] McMillin, B. K., Palmer, J. L., and Hanson, R. K., 1993. "Temporally Resolved, Two-line Fluorescence Imaging of NO Temperature in a Transverse Jet in a Supersonic Cross Flow". *Applied Optics*, **32**(36), Dec., pp. 7532–7545.

[44] Seitzman, J. M., Kychakoff, G., and Hanson, R. K., 1985. "Instantaneous Temperature Field Measurements using Planar Laser-induced Fluorescence". *Optics Letters*, **10**(9), Sept., p. 439.

[45] Lee, M. P., McMillin, B. K., and Hanson, R. K., 1993. "Temperature Measurements in Gases by use of Planar Laser-induced Fluorescence Imaging of NO". *Appied Optics*, **32**(27), Sept., pp. 5379–5396.

[46] Cruyningen, I., Lozano, A., and Hanson, R. K., 1990. "Quantitative Imaging of Concentration by Planar Laser-induced Fluorescence". *Experiments in Fluids*, **10**(1), Oct., pp. 41–49.

[47] Arnold, A., Bombach, R., Käppeli, B., and Schlegel, A., 1997. "Quantitative Measurements of OH Concentration Fields by Two-dimensional Laser-induced Fluorescence". *Applied Physics B: Lasers and Optics*, **64**(5), May, pp. 579–583.

[48] Harrington, J. E., and Smyth, K. C., 1993. "Laser-induced Fluorescence Measurements of Formaldehyde in a Methane/Air Diffusion Flame". *Chemical Physics Letters*, **202**(3âĂŞ4), pp. 196 – 202.

[49] Brackmann, C., Nygren, J., Bai, X., Li, Z., Bladh, H., Axelsson, B., Denbratt, I., Koopmans, L., Bengtsson, P.-E., and Aldén, M., 2003. "Laser-induced Fluorescence of Formaldehyde in Combustion using Third Harmonic Nd:YAG Laser Excitation". *Spectrochimica Acta Part A: Molecular and Biomolecular Spectroscopy*, **59**(14), pp. 3347 – 3356.

[50] Schäfer, F., 1992. "Dye Lasers and Laser Dyes in Physical Chemistry". In *Dye Lasers: 25 Years*, M. Stuke, ed., Vol. 70 of *Topics in Applied Physics*. Springer Berlin, Heidelberg, pp. 19–36.

[51] Kajava, T., Lauranto, H., and Salomaa, R., 1992. "Mode Structure Fluctuations in a Pulsed Dye Laser". *Applied optics*, **31**(33), pp. 6987–6992.

[52] Fluorescence SpectraViewer, 2014. www.lifetechnologies.com.

[53] Scientific Digital Cameras: Fundamental properties of a digital camera., 2014. www.andor.com.

[54] Boyle, W. S., and Smith, G. E., 1970. "Charge-Coupled Semiconductor Devices". *Bell System Technical Journal,* **49**(4), pp. 587–593.

[55] Aikens, R. S., 1991. "Charge-Coupled Devices for Quantitative Electronic Imaging". *International Amateur-Professional Photoelectric Photometry Communications,* **44**, p. 1.

[56] Mendis, S., Kemeny, S. E., and Fossum, E. R., 1994. "CMOS Active Pixel Image Sensor". *Electron Devices, IEEE Transactions on,* **41**(3), pp. 452–453.

[57] Bosch, L. A., 1995. "Dynamic Uses of Image Intensifiers". In Photoelectronic Detectors, Cameras, and Systems, C. B. Johnson and E. J. Fenyves, eds., pp. 159–172.

[58] Ingle, J., and Crouch, S., 1988. *Spectrochemical Analysis.* Prentice Hall PTR, Upper Saddle River, New Jersey.

[59] Alkemade, C. T. J., Snelleman, W., Boutilier, G., Pollard, B., Winefordner, J., Chester, T., and Omenetto, N., 1978. "A Review and Tutorial Discussion of Noise and Signal-to-Noise Ratios in Analytical Spectrometry–I. Fundamental Principles of Signal-to-Noise Ratios". *Spectrochimica Acta Part B: Atomic Spectroscopy,* **33**(8), pp. 383–399.

[60] Boutilier, G. D., Pollard, B. D., Winefordner, J. D., Chester, T. L., and Omenetto, N., 1978. "A Review and Tutorial Discussion of Noise and Signal-to-Noise Ratios in Analytical Spectrometry–II. Fundamental Principles of Signal-to-Noise Ratios". *Spectrochimica Acta Part B: Atomic Spectroscopy,* **33**(8), pp. 401–416.

[61] Hanson, R. K., Seitzman, J. M., and Paul, P. H., 1990. "Planar Laser-Fluorescence Imaging of Combustion Gases". *Applied Physics B: Lasers and Optics,* **50**, pp. 441–454.

[62] Kurz, R., 2005. "Gas Turbine Performance". In Proceedings of the thirty-fourth turbomachinery symposium, pp. 131–146.

[63] Crutzen, P. J., 1979. "The Role of NO and NO_2 in the Chemistry of the Troposphere and Stratosphere". *Annual Review of Earth and Planetary Sciences,* **7**(1), May, pp. 443–472.

[64] Brimblecombe, P., and Stedman, D. H., 1982. "Historical Evidence for a Dramatic Increase in the Nitrate Component of Acid Rain". *Nature,* **298**(5873), July, pp. 460–462.

[65] Correa, S. M., 1993. "A Review of NO_x Formation Under Gas-Turbine Combustion Conditions". *Combustion Science and Technology,* **87**(1-6), Jan., pp. 329–362.

[66] Sigfrid, I. R., Whiddon, R., Aldén, M., and Klingmann, J., 2011. "Parametric Study of Emissions From Low Calorific Value Syn-Gas Combustion, With Variation of Fuel Distribution, in a Prototype Three Sector Burner". In Proceedings of the ASME Turbo Expo, Vol. 2: Combustion, Fuels and Emissions, Parts A and B, GT2011-45689, pp. 643–649.

[67] Schorr, M. M., and Chalfin, J., 1999. "Gas Turbine NO_x Emissions Approaching Zero–Is it Worth the Price?". *General Electric Power Systems, Schenectady, New York*, pp. 1–6.

[68] Bowman, C. T., 1992. "Control of Combustion-generated Nitrogen Oxide Emissions: Technology Driven by Regulation". *Symposium (International) on Combustion,* **24**(1), pp. 859 – 878. Twenty-Fourth Symposium on Combustion.

[69] Dryer, F., 1977. "Water Addition to Practical Combustion Systems–Concepts and Applications". *Symposium (International) on Combustion,* **16**(1), pp. 279 – 295.

[70] Komori, T., Yamagami, N., and Hara, H., 2004. Design for blast furnace gas firing gas turbine.

[71] Ståhl, K., and Neergaard, M., 1998. "IGCC Power Plant for Biomass Utilisation, Värnamo, Sweden". *Biomass and Bioenergy,* **15**(3), pp. 205–211.

[72] Allen, G., Chan, H., and Wey, R., 1983. "Flare-gas Recovery Success at Canadian Refineries". *Oil Gas J.;(United States),* **81**(26).

[73] Gökalp, I., and Lebas, E., 2004. "Alternative Fuels for Industrial Gas Turbines (AFTUR) ". *Applied Thermal Engineering,* **24**(11–12), pp. 1655 – 1663. Industrial Gas Turbine Technologies.

[74] Huang, Z., Zhang, Y., Zeng, K., Liu, B., Wang, Q., and Jiang, D., 2006. "Measurements of Laminar Burning Velocities for Natural Gas–Hydrogen–Air Mixtures". *Combustion and Flame,* **146**(1), pp. 302–311.

[75] Halter, F., Foucher, F., Landry, L., and Mounaïm-Rousselle, C., 2009. "Effect of Dilution by Nitrogen and/or Carbon Dioxide on Methane and Iso-octane Air Flames". *Combustion Science and Technology,* **181**(6), pp. 813–827.

[76] Sigfrid, I. R., Whiddon, R., Collin, R., and Klingmann, J., 2010. "Experimental Investigation of Laminar Flame Speeds for Medium Calorific Gas With Various Amounts of Hydrogen and Carbon Monoxide Content at Gas Turbine Temperatures". In Proceedings of the ASME Turbo Expo, Vol. 2: Combustion, Fuels and Emissions, Parts A and B, GT2010-22275, pp. 173–181.

[77] Abou-Taouk, A., 2011. "CFD Modeling of Combustion in Flexi-fuel Burners at Gas Turbine Conditions". Master's thesis, Chalmers University of Technology.

[78] Escudier, M. P., and Keller, J., 1985. "Recirculation in Swirling Flow - A Manifestation of Vortex Breakdown". *AIAA Journal,* **23**(1), Jan., pp. 111–116.

[79] Reichert, B. A., Hingst, W. R., and Okiishi, T. H., 1994. "Circular-to-Rectangular Transition Duct Flow Without and With Inlet Swirl". *Journal of Propulsion and Power,* **10**(1), Jan., pp. 88–94.

[80] Sigfrid, I. R., Whiddon, R., Abou-Taouk, A., Collin, R., and Klingmann, J., 2012. "Experimental Investigations of an Industrial Lean Premixed Gas Turbine Combustor with High Swirling Flow". In Proceedings of the ASME Gas Turbine India, GTINDIA2012-9681, pp. 559–570.

[81] Abou-Taouk, A., Sigfrid, I. R., Whiddon, R., and Eriksson, L. E., 2012. "A Four-Step Global Reaction Mechanism for CFD Simulations of Flexi-Fuel Burner for Gas Turbines". In Proceedings of the 7th International Symposium on Turbulence, Heat and Mass Transfer,.

[82] Sigfrid, I. R., Whiddon, R., Collin, R., and Klingmann, J., 2013. "Experimental and Reactor Network Study of Nitrogen Dilution Effects on NO_x Formation for Natural Gas and Syngas at Elevated Pressures". In Proceedings of the ASME Turbo Expo, Vol. 1A: Combustion, Fuels and Emissions, GT2013-94355.

GT2013-94443

INVESTIGATION OF A PREMIXED GAS TURBINE COMBUSTOR CENTRAL BODY BURNER USING OH PLANAR LASER INDUCED FLUORESCENCE AT ELEVATED PRESSURES.

Ronald Whiddon *
Robert Collin
Marcus Alden
Department of Combustion Physics
Lund University
Sweden

Ivan Sigfrid
Jens Klingmann
Department of Energy Sciences
Lund University
Sweden

ABSTRACT

Experiments were performed on the central body rich-premix-lean (RPL) burner of a Siemens Industrial Turbomachinary 4th generation DLE combustor to observe the combustion changes that may occur when using fuels other than natural gas. Measurements were taken of temperatures at multiple points along the RPL body while hydroxyl (OH) radical distribution extending from the dump plane of the burner was imaged by planar laser induced fluorescence (PLIF). The RPL burner was run using four fuels- methane, a generic syngas (67.5% H_2, 22.5% CO and 10% CH_4) and dilutions of these with nitrogen to a Wobbe index of 15 MJ/m^3. Each of the fuels was operated at several equivalence ratios ranging from $\phi = 0.80$ to $\phi = 1.80$, for combustion pressures of 3, 6 and 9 bar. It was found that the flame position in the RPL, determined from temperature measurement at the thermocouple positions, was dependent on the fuel, equivalence ratio and to a lesser extent pressure. A link was established between the OH distribution in the post burner region and RPL temperature profiles based on the expected flame behavior inside the RPL. For all measurement points some combustion occurred within the burner volume, indicated by thermocouples at the burner exit.

INTRODUCTION

The use of unconventional fuels is an area of gas turbine research, with a wide range of motivations. Garnering the greatest public attention is the use of carbon neutral or reduced carbon deficit fuels in gas turbines; however, of practical importance is the production of energy using lower grade combustible gases such as gases from material processing or storage. Regardless the reason, by expanding our working knowledge of less conventional gas turbine fuels, we will expand the energy supply and take advantage of under-exploited energy sources resulting in economic and, frequently, environmental benefits. [1–3]

Logically, the use of a fuel with a flexible component list can exacerbate poor gas turbine performance whether it be demonstrated by increased emissions level, flashback, degraded cooling, instabilities, etc. [4]. Additionally, the most attractive burner emissions are found near the lean combustion limit where severe instabilities can result. Inclusion of a pilot flame that operates at a richer, more stable equivalence ratio (ϕ) can alleviate induced instabilities in the larger combustion volume [5]. However the pilot burner is also subject to different combustion performance depending on the makeup of the fuel.

In this work, laser induced fluorescence (LIF) of the hydroxyl radical (OH) is used to image the presence of combustion species from the central body burner in the post burner volume. The OH radical is produced early in the flame chemistry by the chain branching reaction of O_2 and H, and later from chain prop-

*Please address all correspondence ronald.whiddon@forbrf.lth.se

agation reactions of various flame intermediates (CHO, CH_2O, OOH, etc.) [6]. In lean flame measurements, the OH radical appears at the onset of combustion and is in greater concentration than other radicals, the concentration reducing slowly in the hot post combustion gases. [7–9]. High concentration and longevity of the OH radical make it a good marker for flame and post flame regions in large, highly turbulent flames.

LIF signal is produced when light at the wavelength corresponding to transitions between precise electronic, vibrational and rotational energy levels is absorbed by electrons in the valence shell of the target molecule and is later emitted as light of the same or different wavelength. For the OH molecule, the commonly targeted transitions are around 283 nm and 310 nm. The fluorescent signal ($I_{F,OH}$) is described by equation 1.

$$I_{F,OH} = n_{OH} I_L \Phi_C \Phi_L \Phi_Q \qquad (1)$$

Where n_{OH} is the number density of OH molecules, I_L is the initial intensity of the laser, Φ_C is the fluorescence collection efficiency, Φ_L is the laser absorption loss and Φ_Q is the fluorescence quantum yield. The fundamental limit of signal is the concentration of the target molecule (n_{OH}) and the intensity of the excitation source (I_L), which increase with pressure and laser energy, respectively. However, all of the efficiency terms decrease as pressure increases due absorption of light in the laser and fluorescence paths and quenching of the excited OH molecules. The laser absorption loss and fluorescence collection efficiency are also dependent on system design. As a consequence, without detailed correction for multiple determinants of the fluorescent signal, it is impossible to make quantitative comparisons between OH signals from different pressures and systems.

EXPERIMENTAL SYSTEMS AND METHODS

Four fuels were used during testing, their component makeups are found in table 1. Methane was used as a baseline fuel due

to the similarity with Natural gas. A high hydrogen content fuel was used as a generic syngas that might be generated from gasification processes. Both methane and the generic syngas were diluted with nitrogen to lower the Wobbe index to $15MJ/m^3$.

BURNER

A Siemens 4th generation DLE burner, an iteration of which is available in the SGT-750, was provided for testing with non standard fuels. The burner is composed of three premixed burner sectors- a radial swirled main sector, an axial swirled intermediate sector and a jet swirled central body burner, termed the RPL (rich-pilot-lean). The RPL is used to ignite the intermediate and main sectors, but also affects combustion stability. An adapter was used to mount only the RPL sector in the elevated pressure rig. The adapter throat diameter was the same as the intermediate sector, 26mm, but it lacked a swirl element. This adapter allowed cooling of the RPL and the necessary bulk airflow to create the elevated pressure conditions. Thermocouples attached to the outer surface of the RPL, figure 1, were used to give indication of combustion inside the RPL.
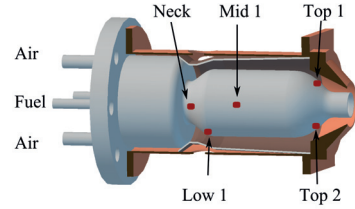

FIGURE 1: Rich-pilot-lean (RPL) burner with cutaway of mounting adapter. Thermocouple positions are marked in red, labels are in convention with subsequent occurrence.

TABLE 1: Gas composition for investigated fuels.

Fuels	Gas Compositions vol.%				W†[MJ/m^3] †	LHV [MJ/kg]	Fuel/Air$_{st}$
	CH$_4$	H$_2$	CO	N$_2$			
Methane	100	0	0	0	55.30	50.01	0.0584
Diluted Methane	33.5	0	0	66.5	15.00	11.19	0.261
Syngas	10	67.5	22.5	0	27.70	33.14	0.104
Diluted Syngas	6.9	46.56	15.52	31.02	15.00	14.05	0.245

†W: Wobbe calculated from higher heating value at 1 Atm and 273.15 K [10]

ELEVATED PRESSURE RIG

All experiments described in this document were performed in the elevated pressure combustion rig described in [11]. This apparatus features a dual shell combustion chamber with a pressure limit of 16 bar. Bulk airflow is provided by a high volume compressor (up to 1.3 kg/s) which passes through the outer shell of the combustion chamber, through a preheating tower, then back through the burner assembly and inner shell of the combustion chamber. The bulk airflow was not preheated in this work as the flow was too low for proper function of the heating tower. Quartz windows in the inner and outer shells allow orthogonal optical access to the combustion chamber. A detail of the high pressure rig, showing the laser path, is shown in figure 2. The pressure in the combustion chamber is controlled by restricting the combustion chamber exit with an adjustable constriction. Finally exhaust gases are cooled, filtered and vented to the atmosphere.

EXPERIMENTAL SETTINGS

Measurements were conducted at pressures of 3, 6 and 9 bar, with cooling air flow rates of 0.028 kg/s, 0.100 kg/s and 0.163 kg/s, respectively. Air and fuel were supplied to the RPL from
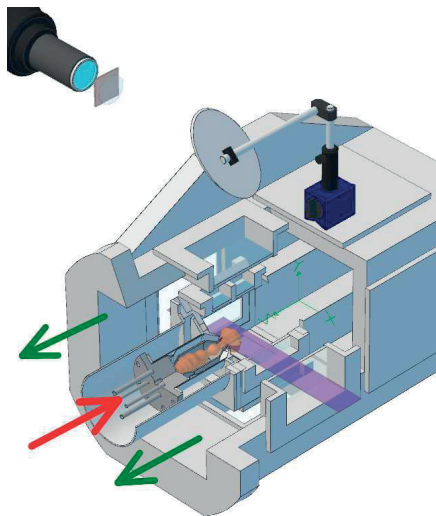

FIGURE 2: Elevated pressure rig combustion chamber section view. Outer shell airflow shown in green, inner flow in red. Laser sheet path is illustrated by a light purple band.

gas bottles, the flows regulated by two coriolis mass flow controllers. The combustion air was preheated to 650 K before passing into the RPL. The same nominal volume flow of 1.4 dm^3/s was used for the 3 and 6 bar experiments, at 9 bar the flow was reduced to 1.2 dm^3/s, limited by the flow controller range. At 3 and 6 bar the equivalence ratios were stepped in intervals of 0.2 between $\phi = 0.8$ and $\phi = 1.8$, conditional on successful combustion at a given equivalence ratio. At 9 bar only three equivalence ratios were tested: $\phi = 1.0$, one rich and one lean equivalence ratio determined by stable burner operation.

LASER AND OPTICS

The laser sheet was produced by an ND:YAG pump laser exciting the Rhodamine 6G gain medium of a dye laser. The laser wavelength was tuned to 566 nm and frequency doubled to near 283 nm. The laser emission line was finely tuned to the Q1(8) transition of the OH radical ($X_{v''=0} \rightarrow A_{v'=1}$) by scanning the excitation spectrum of a Bunsen flame. The laser was formed into a sheet by combination of a -40 mm cylindrical lens and positive 50 mm diameter, 500 mm focal length convex lens. The lenses were arranged with coincident foci which generated a parallel sheet approximately 50 mm in width. The laser sheet was directed across the exit of the RPL oriented parallel to the axial flow of the burner. The laser pulse energy varied from 10 to 14 mJ during measurements, with the energy being optimized before the start of each imaging series.

LIF from OH radicals in the measurement region was collected using a Stanford Instruments PiMAX 2 ICCD camera mounting a 100mm UV-nikkor objective with an aperture setting of 2.8. Two Schott filters, UG11 and WG280, were placed before the objective to reduce transmission of light not arising from the OH transitions near 310nm ($X_{v''=0} \leftarrow A_{v'=0}$). The ICCD integration time was set to 200 nanoseconds to further limit noise contribution from Plank radiation and flame chemiluminescence.

The measurements were composed of 998 single shot images for the 3 bar experiments and 499 single shot images for the 6 and 9 bar. The sample number was reduction was required due to the increased consumption rate of fuels at higher pressures. The single shot images are background subtracted; no correction for laser sheet energy distribution was applied. To evaluate the variability of the flame position, the single shot images were thresholded, filtered using a two dimensional FFT filter and averaged. The resulting probability distribution shows the spatial likelihood of observing LIF from an OH radical in the measurement region.

RESULTS

Temperature measurements recorded from the 5 thermocouples mounted on the outer surface of the RPL are shown in figure 3. They are named as in figure 1.
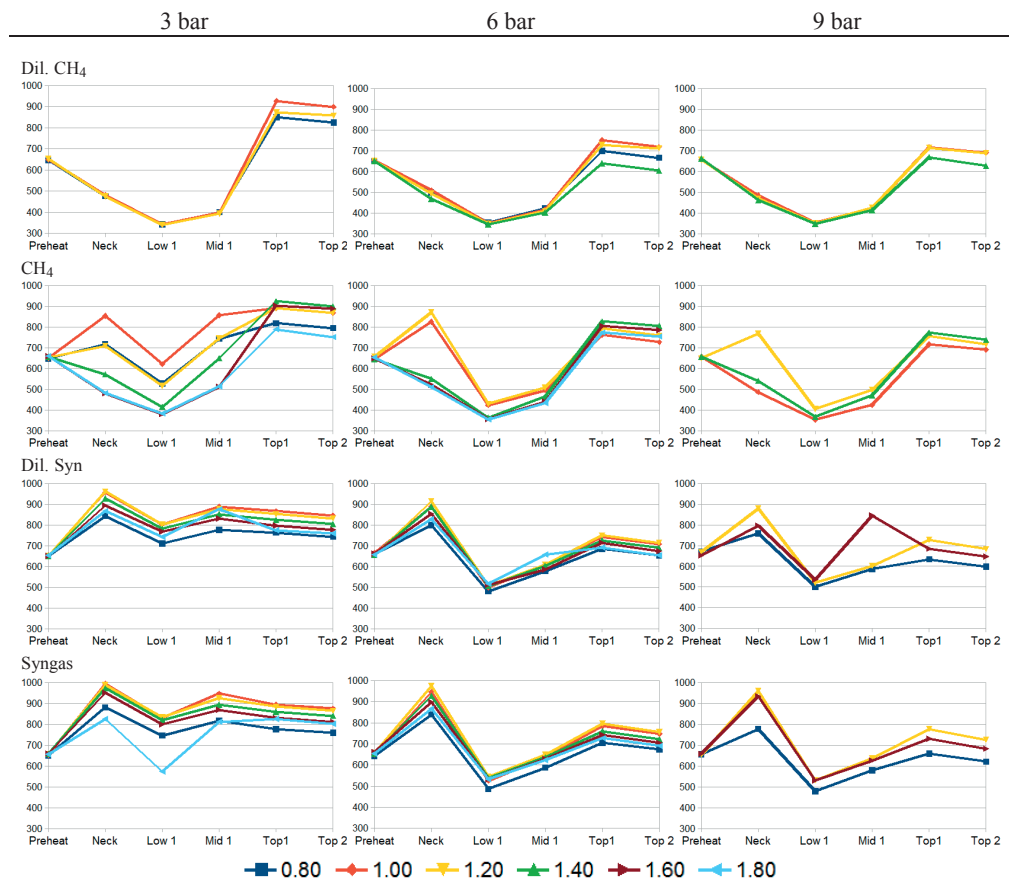
FIGURE 3: Temperature averages for preheater and RPL mounted thermocouples for the various pressures, fuels and equivalence ratios tested. Images show from top to bottom; dilute methane, methane, dilute syngas, and syngas. Pressures are shown from left to right; 3, 6 and 9 bar
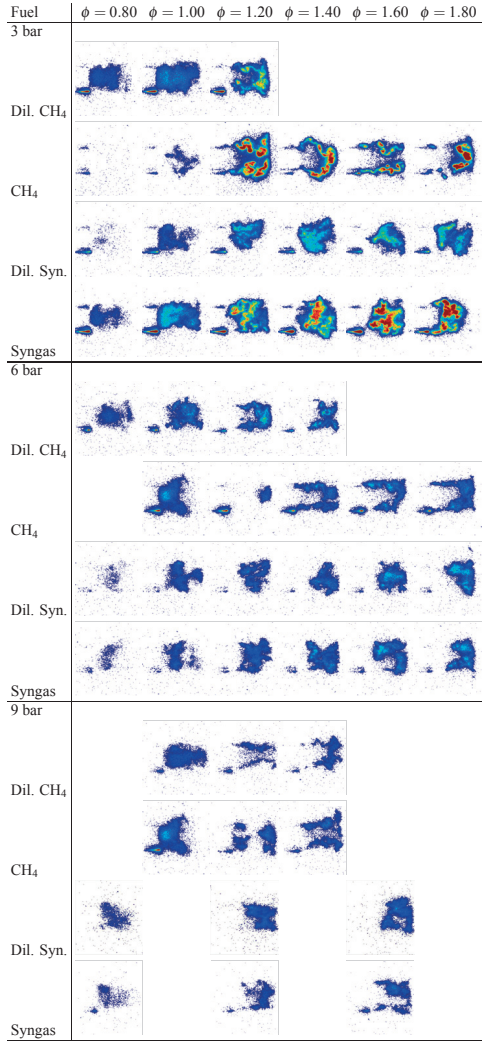
FIGURE 4: Single pulse OH LIF images for various pressures, ϕ and fuels. Flow is from left to right, intensity range is 0 to 4000 counts, blue to red.
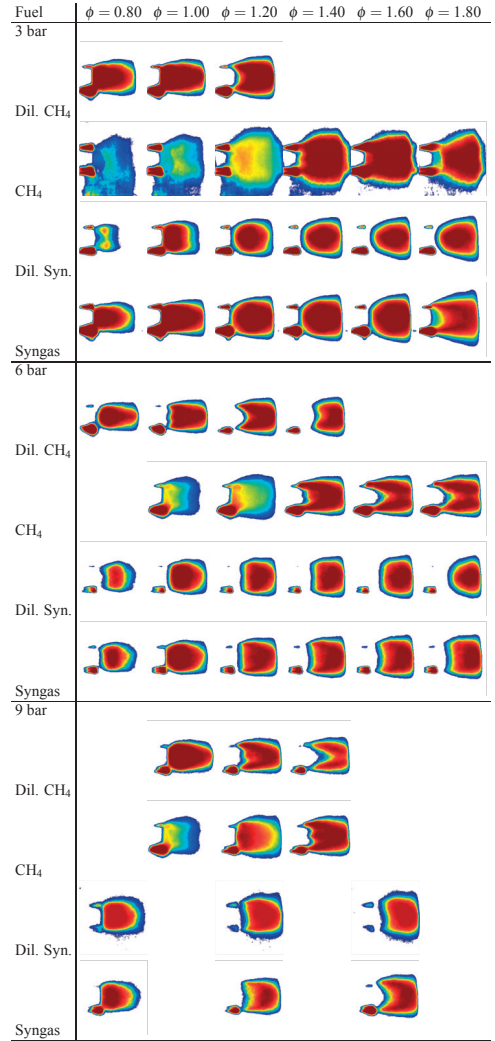

FIGURE 5: Spatial probability of occurrence for the OH molecule for various pressures, ϕ and fuels. Flow is from left to right, intensity range is 0 to 1, blue to red.

Single shot OH-LIF images, chosen at random for each of the test coordinates (pressure, fuel, equivalence ratio), are shown in figure 4. OH probability distributions from the same test coordinates are shown in figure 5. In both image sets, the burner is oriented horizontally with flow moving from left to right. The RPL end extends into the images as seen by the laser reflections of its surface at the left side of the image.

DISCUSSION

Before a examining the measurements, it is useful to consider the gas flow that occurs inside the RPL volume. CFD models of a similarly shaped burner which were composed by Grosshans et al. [13] and Salewskia et al. [14] show a swirling flow will follow the contour of an expanding curved wall. In the axial center of the volume a recirculation zone will establish, stretching towards the inlet. A contracting curved outlet will raise axial velocities, and will also strengthen any remaining swirl. The spatial distribution of flow velocities means that fuels with low flame speed will combust towards the center of the burner while faster burning fuels will stabilize in the higher velocity flows. Hence, syngas will be the most likely to combust in the high velocity regions near the wall while dilute methane may be limited to the central slow region, according to their respective flame speeds. [15, 16]

Temperature

The thermocouple "Neck" is positioned closest to the RPL fuel/air inlet where flow velocities will be quite high. As this position has limited exposure to the cooling flow any temperature higher than 650 K will indicate proximal combustion. The thermocouple "Low 1" is located just before the RPL expansion ends and "Mid 1" is slightly downstream of this position. These thermocouples are heavily skewed by the cooling flow, making it difficult to identify local heat release, as temperatures might appear low relative to "Neck" even when combustion is present. Thermocouples "Top 1&2" show temperatures that are consistently higher than "Low 1" and "Mid 1" for all fuels and pressures. As these thermocouples reflect a blend of combusting and non-combusting regions of the RPL, this is proof that for all conditions investigated, some portion of combustion takes place inside the RPL. Understandably, recorded temperatures reflect the influence of pressure on cooling flow, i.e., thicker air removes more heat. This should be considered when making comparisons between different pressures.

Methane shows the greatest difference in temperature behavior over the range of experimental variables. At 3 bar, equivalence ratios of 0.80, 1.00 and 1.20 demonstrate combustion near the RPL entrance. The temperature recorded for these three equivalence ratios at "Mid 1" would show that further heat release occurs, as temperatures are higher than those recorded up-

stream. Moving to "Top 1&2", $\phi = 0.80$ drops in temperature relative to $\phi = 1.00$ and 1.20, suggesting a slightly different combustion process at the RPL exit. The $\phi = 1.60$ and 1.80 show essentially no heat release at the RPL entrance, however, thermocouples "Top 1&2" show that combustion has occurred such that the resulting temperature is equal to those measured for the previous equivalence ratios at RPL exit. The $\phi = 1.40$ test at this pressure indicates very slight heat release near the RPL entrance, as the temperature recorded at "Neck" is higher than in the $\phi = 1.60$ and 1.80 cases. There is an increase in temperature at the "Mid 1" position, and values equal to levels for the $\phi = 1.00$ and 1.20 are seen at the RPL exit. It would seem that the flame speed for this equivalence ratio is just slightly too slow to support a flame in the high velocity flow region. At 6 bar pressure, the methane fuels show only two temperature profiles between the different equivalence ratios. For $\phi = 1.00$ and 1.20, there is still a measured increase in temperature at the "Neck" thermocouple while all other thermocouples only show a relative increase at the exit. At this pressure, it was not possible to ignite below $\phi = 0.93$. At 9 bar the only equivalence ratio to exhibit heat release at the "Neck" position is $\phi = 1.20$.

The dilute methane temperature profiles confirm that there is no combustion at the inlet of the RPL for this fuel, indicated by the drop in temperature between "Preheat" and "Neck" readings. The temperatures recorded for "Top 1" and "Top 2" show that there is heat release from the lower velocity regions of the RPL center. This trend is true for all pressures and equivalence ratios of dilute methane tested. The temperature values seen here for "Neck", "Low 1" and "Mid 1" may be considered characteristic of combustion cases where there is no combustion in the region near the RPL wall.

Both syngas and dilute syngas burn close to the entrance of the RPL, in all test cases that used these fuels. Temperature values for dilute syngas at 3 bar are stable along the length of the RPL for all equivalence ratios. This indicates combustion is occurring close to the wall and is not interrupted as it progresses through the RPL. When increasing pressure to 6 bar, the temperature drops drastically at "Low 1". This is due in large part to more efficient cooling at higher pressure, but may also indicate local quenching of combustion. There is no significant difference in the 9 bar case. Syngas follows the same pattern as dilute syngas with respect to temperature values with the exception of the syngas $\phi = 1.80$ case. At "Low 1" there is a drop in temperature which is not due to cooling, but rather suggests that the flame cannot stabilize in the high velocity flow near the wall at this position.

In all, three temperature profiles are evident:

TP 1 Combustion starting early in the RPL and extending along the wall towards the RPL exit.

TP 2 Combustion restricted only to the center of the RPL.

TP 3 Combustion appearing at the "Neck" position but no indication of combustion at "Low 1".

OH-LIF

Two things are immediately apparent from the single shot OH-LIF images, figure 4; first the increase in signal at 3 bar for rich equivalence ratios, and second, the decrease in intensity of the OH-LIF signal as pressure is increased. For rich equivalence ratios there is excess fuel available at the RPL exit which will result in further OH production. The decrease in signal corresponding to pressure shows that the signal loss factors mentioned in equation 1 outweigh any increase in OH number density.

The OH-LIF visual structure can be classified in a rudimentary way using two parameters; the position- attached or detached and the appearance- diffuse or hollow. Examples of these structures are shown in figure 6 for both single shot and probability distribution images. While discussion of structure refers specifically to the OH signal, relevance to flame structure may be inferred. The OH structures that are seen for the various fuels, equivalence ratios and pressures in figure 5 can be understood by considering how flow through the RPL for the three above mentioned temperature profiles will affect the distribution of combustion products and unreacted air/fuel mixture transported out of the RPL.

In temperature profile 1, fuel and air are evenly consumed throughout the volume of the RPL. Lean combustion may come to near completion inside the RPL if the combustion rate versus residence time permits. OH molecules seen in the laser measurement region will have either been generated inside the RPL or as a result of uninterrupted combustion extending past the RPL exit. This can lead to a highly variable OH distribution as pro-
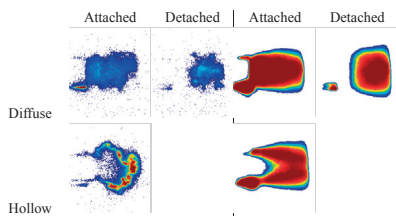

Attached   Detached | Attached   Detached

Diffuse

Hollow

FIGURE 6: Dominant combinations of appearance and location parameters for the OH-LIF signal. Single shot examples on left and probability distribution examples on right.

duction slips occasionally past the RPL exit, which can be seen in the diffuse-attached OH structure of the 3 bar, lean images for methane, syngas and dilute syngas. In rich conditions, the gases exiting the RPL will contain an even distribution of fuel but oxygen from the cooling flow must diffuse into this fuel rich exhaust for combustion to resume. As the concentration of fuel remaining in the RPL outflow increases, more time is needed for the mixture to drop below the rich combustion limit and so the flame moves further downstream of the RPL exit, as indicated by the production of OH. This behavior is exemplified in the diffuse-detached structures of syngas and dilute syngas at 3 bar.

For temperature profile 2, combustion is only occurring in the slow moving central region of the RPL. Thus, fuel and air in the high velocity region near the wall of the RPL does not ignite and is carried through the RPL exit. The center of flow passing through the RPL exit is drawn from the central, lower velocity regions of the reaction volume, it will contain combusting and/or combusted gases. In fuel lean situations, combustion will take place once the flow velocity slows sufficiently, though combustion may be sustained in the center flow across the RPL exit. The result is an OH signal that is diffuse; but, as a some portion of combustion must occur outside of the RPL, the OH distribution will be more consistent than the lean case in temperature profile 1. Lean dilute methane experiments are an example of this process. Under rich conditions, combustion is found at the radial edge of the RPL outflow due to the combination of the slowing flow and entrainment of air from the cooling flow lowering the equivalence ratio. This creates the hollow-attached structure seen to dominate the fuel rich methane and dilute methane experiments.

The third temperature profile is characterized by a temperature value denoting combustion registered at the "Neck" position with a rapid drop in temperature at the "Low 1" position. This profile is the most prolific, seen for methane $\phi = 1.00$ and 1.20 at 6 bar and $\phi = 1.20$ at 9 bar, and all equivalence ratios for syngas and dilute syngas at both 6 and 9 bar. The temperature profile at pressures greater than 3 bar might be explained as increased cooling of the thermocouples, which are mounted on the outer surface of the RPL. Then this would be nothing more than a skewed temperature profile 1. However, the 3 bar syngas experiment for $\phi = 1.80$ has this temperature profile as well; in this case cooled thermocouples are are not the culprit. Additionally, the OH structure from this test has much in common with fuel rich conditions that exhibit the type 2 temperature profile. The explanation for the ambiguity in the $\phi = 1.80$ syngas 3 bar experiment is that the combustion registered by the "Neck" thermocouple is quenched near "Low 1", perhaps due to the cooling at that position. So, fuel/air mixture in the high velocity flow near the wall which had begun to react, stops before all the oxygen is consumed, possibly reigniting further down the RPL. If the combustion proceeds to a great extent before exiting the RPL, it will contain little oxygen, which should result in the phenomena

discussed for fuel rich conditions in temperature profile 1. If the combustion is mostly incomplete, the unreacted air/fuel mixture will behave as discussed for the fuel rich conditions for temperature profile 2. In point of fact the concepts of quenching and degree of combustion completion in the high velocity flow region of the RPL is the exact explanation for all the temperature distributions seen. Temperature profile 1 and 2 are merely the opposite extremes of where combustion processes occur, showing no quenching near the RPL wall and severe quenching, respectively. The conditions that exists between these two extremes are why syngas, dilute syngas and methane all show a type 3 temperature profile for 6 and 9 bar experiments, but demonstrate such different OH structures as they either reach near complete combustion or only just begin.

Before closing it must be admitted that the deductions made only draw on basic consideration of laminar flame speed and the likely distributions of flow velocities in the body of the RPL. Only one concept of fluid motion through the RPL is considered for all fuels and pressures, this may be incorrect. Cooling and quenching are alluded to, but the complex interactions between heat release and heat loss as it pertains to light and heavy gases is beyond the scope of this paper. This may be particularly pertinent in a more detailed comparison of syngas to methane, or to dilute syngas, which contains a large percentage of nitrogen.

Conclusions

Temperature data from thermocouples attached to the skin of a central body burner is organized into three groups based on whether combustion was indicated close to the wall mounted thermocouples.

A correlation exists between laminar flame speeds and detected combustion near the wall. Thus syngas and dilute syngas are often indicated as burning near the wall, while dilute methane does not. This correlation applies to equivalence ratios as well.

Methane experiments at 3 bar show a strong relationship between equivalence ratio and indicated flame location. It possible that tuning of the volumetric flow rates for this experiment would cause a significant change for flame distribution in the RPL.

OH-LIF images for all experiments are organized according to three basic patterns: diffuse-attached, diffuse-detached, and hollow-attached

For fuel lean combustion, a diffuse-attached structure is most prevalent for all fuels. For fuel rich combustion of methane and dilute methane hollow-attached is the common structure, fuel rich combustion of syngas and dilute syngas fall into the diffuse-detached category.

Increasing the pressure does not appear to drastically change the flame location inside the RPL, neither does it drastically change the structure of the OH distribution outside the RPL.

REFERENCES

[1] Roy, G., 2010. "Utilizing associated gas in industrial gas turbines". *Cogeneration and On-Site Power Production, 11*(1), January, pp. 1–6.

[2] Gkalp, I., and Lebas, E., 2004. "Alternative fuels for industrial gas turbines (aftur)". *Applied Thermal Engineering, 24*(1112), pp. 1655 – 1663. Industrial Gas Turbine Technologies.

[3] Christen, K., 2004. "Environmental impacts of gas flaring, venting add up". *Environmental Science & Technology, 38*(24), pp. 480A–480A. PMID: 15669294.

[4] Chiesa, P., Lozza, G., and Mazzocchi, L., 2005. "Using hydrogen as gas turbine fuel". *Journal of Engineering for Gas Turbines and Power, 127*(1), pp. 73–80.

[5] Albrecht, P., Bade, S., Lacarelle, A., Paschereit, C. O., and Gutmark, E., 2010. "Instability control by premixed pilot flames". *Journal of Engineering for Gas Turbines and Power, 132*(4), pp. 1–8.

[6] Coffee, T. P., 1984. "Kinetic mechanisms for premixed, laminar, steady state methane/air flames". *Combustion and Flame, 55*(2), pp. 161–170.

[7] Bechtel, J. H., and Teets, R. E., 1979. "Hydroxyl and its concentration profile in methane-air flames". *Appl. Opt., 18*(24), Dec, pp. 4138–4144.

[8] Norton, T. S., Smyth, K. C., Miller, J. H., and Smooke, M. D., 1993. "Comparison of experimental and computed species concentration and temperature profiles in laminar, two-dimensional methane/air diffusion flames". *Combustion Science and Technology, 90*(1-4), pp. 1–34.

[9] Buschmann, A., Dinkelacker, F., Schfer, T., Schfer, M., and Wolfrum, J., 1996. "Measurement of the instantaneous detailed flame structure in turbulent premixed combustion". *Symposium (International) on Combustion, 26*(1), pp. 437 – 445.

[10] Gasunie, N. N., 1988. *Physical Properties of Natural Gases*. N.V. Nederlandse Gasunie.

[11] Seyfried, H., Brackmann, C., Lindholm, A., Linne, M., Barreras, F., and Bank, R. V. D., 2007. "Optical Diagnostics Applied to a Gas Turbine Pilot Burner". *AIAA Journal, 45*(11), Nov., pp. 2702–2709.

[12] Sigfrid, I. R., Whiddon, R., Alden, M., and Klingmann, J., 2011. "Experimental investigations of lean stability limits of a prototype syngas burner for low calorific value gases".

ASME Conference Proceedings, **GT2011**(45694), pp. 651–658.

[13] Grosshans, H., Szasz, R., and Fuchs, L., 2010. "Sensitivity analysis of spray dispersion and mixing for varying fuel parameters". In 7th International Conference on Multiphase Flow - ICMF 2010 Proceedings, ICMF.

[14] Salewski, M., Duwig, C., Milosavljevic, V., and Fuchs, L., 2007. "Large Eddy Simulation of Spray Combustion in a Swirl-Stabilized Gas Turbine Burner". In 43rd AIAA/ASME/SAE/ASEE Joint Propulsion Conference & Exhibit, Joint Propulsion Conferences, American Institute of Aeronautics and Astronautics.

[15] Sigfrid, I. R., Whiddon, R., Collin, R., and Klingmann, J., 2010. "Experimental investigation of laminar flame speeds for medium calorific gas with various amounts of hydrogen and carbon monoxide content at gas turbine temperatures". *ASME Conference Proceedings,* **2010**(43970), pp. 173–181.

[16] Prathap, C., Ray, A., and Ravi, M., 2008. "Investigation of nitrogen dilution effects on the laminar burning velocity and flame stability of syngas fuel at atmospheric condition". *Combustion and Flame,* **155**(12), pp. 145 – 160.

Paper II

GT2011-45694

EXPERIMENTAL INVESTIGATIONS OF LEAN STABILITY LIMITS OF A PROTOTYPE SYNGAS BURNER FOR LOW CALORIFIC VALUE GASES

Ivan R. Sigfrid
Department of Energy Sciences
Lund University
Sweden

Ronald Whiddon
Department of Combustion Physics
Lund University
Sweden

Marcus Aldén
Department of Combustion Physics
Lund University
Sweden

Jens Klingmann
Department of Energy Sciences
Lund University
Sweden

ABSTRACT

The lean stability limit of a prototype syngas burner is investigated. The burner is a three sector system, consisting of a separate igniter, stabilizer and Main burner. The ignition sector, Rich-Pilot-Lean (RPL), can be operated with both rich or lean equivalence values, and serves to ignite the Pilot sector which stabilizes the Main combustion sector. The RPL and Main sectors are fully premixed, while the Pilot sector is partially premixed. The complexity of this burner design, especially the ability to vary equivalence ratios in all three sectors, allows for the burner to be adapted to various gases and achieve optimal combustion. The gases examined are methane and a high H_2 model syngas (10% CH_4, 22.5% CO, 67.5% H_2). Both gases are combusted at their original compositions and the syngas was also diluted with N_2 to a low calorific value fuel with a Wobbe index of 15 MJ/m^3. The syngas is a typical product of gasification of biomass or coal. Gasification of biomass can be considered to be CO_2 neutral. The lean stability limit is localized by lowering the equivalence ratio from stable combustion until the limit is reached. To get a comparable blowout definition the CO emissions is measured using a non-dispersive infrared sensor analyzer. The stability limit is defined when the measured CO emissions exceed 200 ppm.

The stability limit is measured for the 3 gas mixtures at atmospheric pressure. The RPL equivalence ratio is varied to investigate how this affected the lean blowout limit. A small decrease in stability limit can be observed when increasing the RPL equivalence ratio. The experimental values are compared with values from a perfectly stirred reactor modeled (PSR), under burner conditions, using the GRI 3.0 kinetic mechanism for methane and the San Diego mechanism for the syngas fuels.

INTRODUCTION

The demand for an environmentally friendly energy supply is pushing the gas turbine community to develop gas turbine systems that can handle a wide variety of fuels. Currently, a number of gas turbines are in use which are designed to run on specific fuels e.g., fuel oil, diesel and natural gas [1]. However, producing a gas turbine that can handle a wide range of fuels, without the down-time associated with refits, is difficult. Such a wide range operability hinges on the design of a combustor that functions properly irrespective of the fuel being used. Such an installation would offer the ability to alternate the fuel depending on availability and cost.

Table 1 Compositions of the gases examined

Gases	Gas compositions vol%				W* [MJ/m³]	LHV [MJ/kg]	Fuel/Air$_{St}$
	CH$_4$	H$_2$	CO	N$_2$			
Ref.	100	0	0	0	55.30	50.01	0.0584
Syngas	10	67.5	22.5	0	27.70	33.14	0.104
Diluted Syngas	6.9	46.56	15.52	31.02	15.00	14.05	0.245

*Wobbe index based on the higher heating value (HHV).

This paper investigates the lean blowout limit (LBO) of a scaled 4th generation premixed dry low emission (DLE) burner supplied by Siemens, which was developed, in part, to be fuel flexible. The difficulty in handling different fuels lies in the large variance in fuel characteristics e.g., Wobbe index [2], laminar flame speed, ignition delay time and adiabatic flame temperature [3]. Wobbe index describes the ability of a fuel to transport energy into a system; a lower Wobbe index fuel requires larger volumes of fuel in order to maintain a desired power output. This added flow pushes the compressor towards the instable operating region close to the surge line [4]. Fuels that have a high laminar flame speed, for instance fuels with high hydrogen content, may cause flashback. The ignition delay time may cause the premixed fuel/air to auto-ignite prior to reaching the combustion zone. Variations in adiabatic flame temperature not only affect the NOx emissions by influencing the thermal NOx reaction pathway [5-7], but also, if too high, can reduce the combustor lifetime. The fuels investigated in this paper are methane (as a reference) and a high hydrogen content syngas mixture [1], which is also diluted with nitrogen, see Table 1. Noticeable is the large difference in the stoichiometric fuel to air ratio (Fuel/Air$_{St}$), which is four times larger for diluted syngas compared to methane. The diluted syngas is a type of gas that could be produced and combusted in an IGCC.

NOMENCLATURE

T	Temperature
Y	Mass fractions
W	Molecular weight
c_p	Specific heat at constant pressure
h	Species specific enthalpy
t	Time
$\dot{m}$	Mass flow
$\dot{w}$	Mass flow

Greek letters

ϕ	Equivalence ratio
ρ	Density
τ_{res}	Residence time
$\dot{\omega}$	Production rate

Subscripts

Main	Main burner section
Pilot	Pilot burner section
RPL	RPL burner section
i	Index
in	Inlet
tot	Total

EXPERIMENTAL SETUP

The experimental setup consists of an air and fuel supply system, the burner, a liner with an emissions probe at the end and an emission measurement system. The air and fuel supply, emissions system and the data sampling are only covered briefly in this paper.
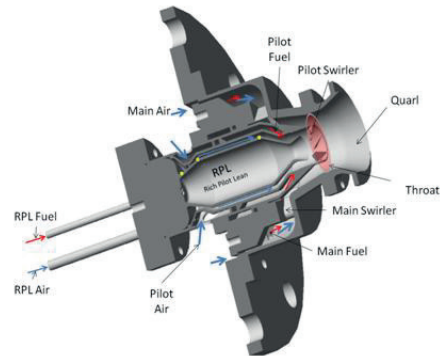

Figure 1 Scaled 4th generation DLE burner. The red arrows indicate fuel flow and blue arrows air flow. RPL thermocouple placements are indicated by yellow dots. The throat section of the burner is highlighted in red.

Burner

The burner used in the experiments is a scaled 4th generation DLE burner supplied by Siemens. It is has three concentric sections with separate fuel feeds. The sections are called RPL (Rich-Pilot-Lean), Pilot and Main (figure 1). All sections are in co-swirl arrangement.

The RPL is a central body stabilizer and can be set to run under both rich and lean conditions. The volume flow through the RPL can be controlled independently of the Pilot and the Main sections and is set to ~2.4% of the total volume flow. It is kept constant for all the tests in this investigation. The fuel and air is premixed before entering a swirler in the bottom of the RPL, after which the mixture is ignited. The position of the flame is monitored by three type N thermocouples placed on the outside wall of the RPL. These three thermocouples are placed at the RPL swirler, the conical expansion of the RPL and at the exit contraction of the RPL (yellow dots, Figure 1). The probe positions are Neck, Bottom and Top, designated, starting from the RPL entrance.

The fuel to the Pilot is injected perpendicularly to the oncoming airflow, at the exit contraction of the RPL, where it mixes with the air until combustion, just before the axial swirlers. As the fuel is injected close to the combustion zone, it is assumed that the mixing of fuel and air is not complete. The fuel to the Main is injected through circular pins positioned upstream of radial swirlers.

The combustion is stabilized in the conical section after the burner (figure 1). The conical section leads to an 85 mm x 700 mm cylindrical liner, which allows the necessary post combustion residence time (~15 ms), with a combustor loading below 10 kg/s atm$^{1.8}$m^3 as defined in [8].

$$Combustor\ Loading = \frac{\dot{m}}{VP_{in}^{1.8}10^{0.00145(T_{in}-400)}}$$

At the end of the combustion liner, there is a contraction to 50% of the liner cross-sectional area extending 15 cm. An emissions rake located in this extension, samples the exhaust gases at 8 equidistant points.

The air split between the Main and the Pilot is controlled by the pressure drop over their respective air paths. To determine the air split, effective areas are used [9]. The effective area is, theoretically, the area of the *vena contracta* after a step contraction that would give the same pressure drop as the air flow through an arbitrary air path.

The calculated air flow distribution is 21% through the Pilot and 79% through the Main burner pathway. The accuracy of the calculated effective areas are 5% for the Pilot and 2% for the Main, disregarding any effects from fuel injection.

Air and fuel supply

The air is supplied to the burner via two separate systems-one which supplies the Main and Pilot sections of the burner, and a second that supplies the RPL. Both systems preheat the air to 650 K. The fuel is supplied to the three burner sections separately, making it possible to vary the equivalence ratios in each section independently.

Emissions system

The emission system consists of a paramagnetic O_2 meter (Oxynos 100), an IR photometry CO/CO_2 meter (Binos 100) and a chemiluminescence NO_x meter (CLD 700). In this paper only values from the CO meter are considered.

Data sampling

For data sampling and control of the combustion system, an in-house computer program was used. It registers 30 measurements for each data point at a rate of 1 Hz. The standard deviations of these measurements are shown as error bars in the figures.

MODELLING

The blowout residence time and the adiabatic flame temperature (figure 2) was modeled using the free software package CANTERA [10]. The laminar flame speed calculations (figure 3) were done using the commercial software DARS v2.04 [11, 12]. The chemical kinetic mechanisms used were GRI 3.0 [13] for methane and the San Diego mechanism [14] for the syngas mixtures. The San Diego mechanism was used since it gives better agreement with results for syngas [12, 15].

Blowout residence time

The blowout residence time (figure 4) is calculated using an in-house perfectly stirred reactor (PSR) model which assumes non-isothermal adiabatic reaction [16]. A PSR qualitatively describes the chemical kinetic influence on the LBO. However the actual LBO is influenced on the burner geometry and function. The inlet temperature for the calculations is 650K.

The reactions occur in a reactor with one inlet and outlet, where the inlet flow is instantaneously mixed with the reacting flow. Thus the reacting flow and the outlet have the same state. The model solves the species conservation equation:

$$\frac{dY_i}{dt} = \frac{1}{\tau_{res}}\left(Y_{i,in} - Y_i\right) + \frac{\dot{w}_i W_i}{\rho}$$

and the energy equation:

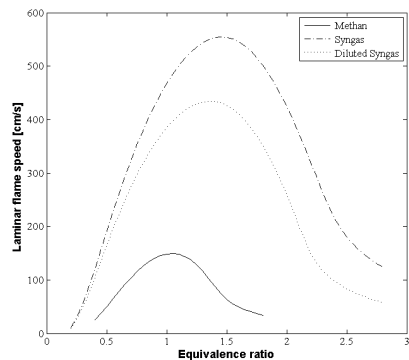**Figure 2 Adiabatic flame temperature for the examined fuels at inlet temperature 650 K**

Figure 3 Laminar flame speeds for the examined fuels at inlet temperature 650 K

$$c_p \frac{dT}{dt} = \frac{1}{\tau_{res}} \sum Y_{i,in}(h_{i,in} - h_i) + \sum \frac{h_i \dot{w}_i W_i}{\rho}$$

where:

$$\tau_{res} = \frac{\rho V}{\dot{m}}$$

The continuity equation assumes the conservation of mass, which is true for a steady state solution. The equations above are solved for the residence time in question until steady state is achieved. The blowout residence time is defined as the minimum residence time acquired to maintain ignition in the reactor. The result of the calculations is illustrated in figure 4. The lean blowout equivalence ratio can be found where the gradient is large. It is harder to define a specific blowout equivalence ratio for the rich mixtures as the gradient is not as steep.

DEFINITION OF LEAN BLOWOUT

The lean blowout measurements were performed by lowering the total equivalence ratio of the burner until the combustion ceased or the CO emissions indicated that the flame was about to blowout. For this experiment, the blowout limit was defined as the equivalence ratio where CO concentration exceeded 200 ppm (figure 5). The 200 ppm limit was chosen both because it is high enough to indicate bad combustion and further the gradient $\frac{d[CO]}{d\phi}$ is large, thus reducing influence of the concentration measurement error.

EXPERIMENTAL RESULTS

All experiments were performed at atmospheric pressure with an inlet air temperature of 650 K. The metal temperature on the outside wall of the RPL was measured at
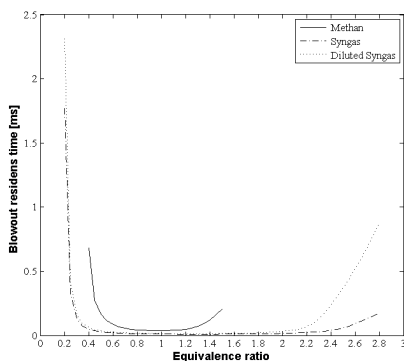
three points to give an indication of the flame position inside the RPL. (Observing figure 8, equivalence rations 1.6 and 1.8, the measured RPL wall temperature is ~630 K, indicating some degree of heat loss between the preheater and the RPL wall.) The mean unburnt volume flow 0.12 m³/s, 0.14 m³/s and 0.16 m³/s for methane. For syngas and diluted syngas it was 0.09 m³/s and 0.13 m³/s, respectively. This gives a variation of throat velocity (unburnt gas) between 49-86 m/s. The throat section is situated at the beginning of the quarl (figure 1). The RPL equivalence ratio was varied as part of the experiment, to determine its role in combustion. The total RPL flow was 0.0028 m³/s the same for all experiments. The equivalence ratios of the Main and the Pilot sections of the burner were kept equal throughout the experiments. When performing the blow out tests the throat velocity and the RPL settings were held constant. It should be noted that accuracy of the total equivalence ratio is ±0.0025 for all measurements, limited by the standard deviation of the air flow supplied to the Main and Pilot.

Methane

The methane blowout test was performed with RPL equivalence ratios ranging from 0.8 to 1.8 (figure 6). When the tests are conducted at higher RPL equivalence ratios, the blowout occurs at progressively lower total equivalence ratios (figure 7). Additionally, the combustion is more stable at higher RPL equivalence ratios, as the smaller standard deviation in CO concentration indicates less fluctuation in the combustion. In most cases, the transition from stable combustion to flameout can be seen as a rapid increase in CO emission (figure 5); however, when the RPL equivalence ratio was set to 0.8, blowout occurred at total equivalence ratio 0.47, without onset of high CO values. The measured blowout limits were found to be in agreement with the range predicted by the PSR calculation: ~0.45
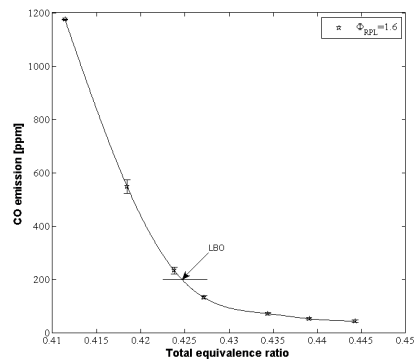

Figure 4 The blowout equivalence ratio is observed where the gradient of the blowout residence time is steep

Figure 5 The lean blowout of methane at an RPL equivalence ratio of 1.6 were measured to be at a total equivalence ratio of 0.422. Volume flow 0.12 m3/s
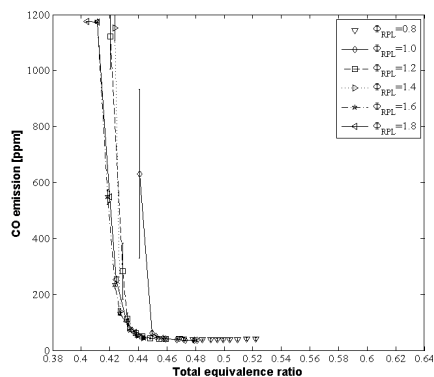
Figre 6 CO emission from lean blowout measurement for methane. Volume flow 0.12 m³/s

Figure 7 Change of blowout limit for methane when varying RPL equivalence ratio. Volume flow 0.12 m³/s

depending on the specified cutoff blowout residence time (figure 4).

The temperature measurements from the RPL give some indication of the RPL flame behavior at the chosen equivalence ratios. A high temperature shows the presence of combustion heat release. For equivalence ratios 0.8-1.4 (figure 8), the temperature measurements show that the flame is positioned in the upper half of the RPL, as the Top temperature probe shows the highest temperature. At the RPL equivalence ratios 1.6 and 1.8 the temperatures indicate that no combustion takes place inside the RPL; thus, due to change in equivalence ratio the flame speed has dropped below a limit where the flame can be stabilized inside the burner.

An LBO test for the volume flows 0.14 m³/s and 0.16 m³/s (figure 9) indicate that increasing the flow through the burner slightly increases the lean blowout equivalence ratio. This is a typical behavior for most combustors [17]. The tests were done with the RPL equivalence ratio 1.6. The RPL temperature measurements for this test are ~800 K, indicating that the RPL combustion is within the RPL.

Syngas

The undiluted syngas blowout test was performed with RPL equivalence ratios ranging from 0 to 1.8. The lean blowout measurements for syngas show that the blowout limit is significantly lower than for methane, ranging from equivalence ratio 0.3-0.34 (figure 10).

With syngas combustion it was possible to run the burner without any combustion taking place in the RPL (figure 10). When increasing the RPL equivalence ratio the stability limit trend is the same as that for methane, i.e., lean blowout occurs at lower values (figure 11).
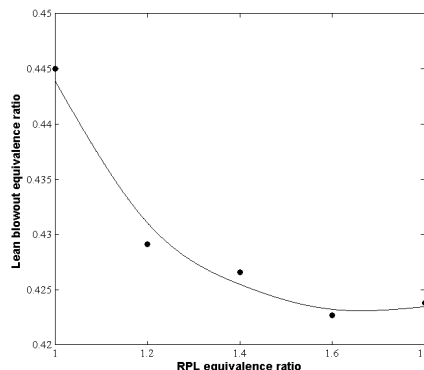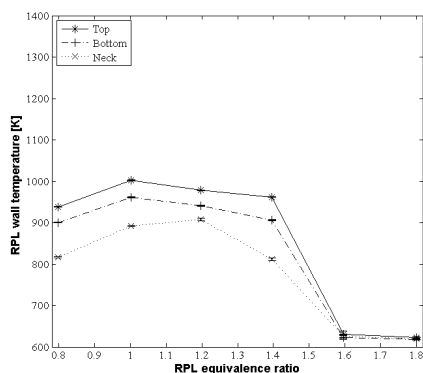

Figure 8 Temperature measurements for methane. Volume flow 0.12 m³/s

Analysis of the temperature measurements indicate, because of the small temperature difference between the three thermocouples that at an RPL equivalence ratio of 0.4, combustion takes place in the centre of the burner, similar to stoichiometric methane. The laminar flame speeds in figure 2 show that the laminar flame speed for the syngas at an equivalence ratio of 0.4 is at the same level (approximately 100 cm/s) as for the methane measurements (excluding the two richer RPL equivalence ratios).

For RPL equivalence ratios from 0.8-1.8, the high neck temperature indicates that combustion occurs directly after entering the RPL, perhaps attached to the inlet ports. The high temperatures seen at the RPL exit for equivalence
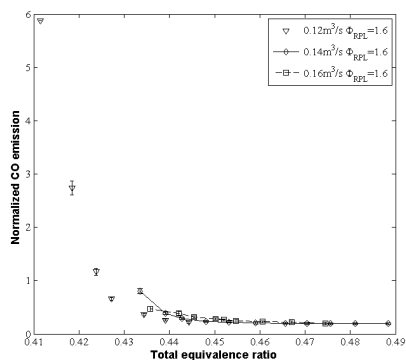
Figure 9 CO emission from lean blowout measurement for methane

Figure 10 CO emission from lean blowout measurement for syngas. Volume flow 0.09 m³/s

ratios of 1.2-1.6 suggest that there may be flash back in the Pilot burner section (figure 12). Removal of the liner showed that indeed the flame was attaching to the Pilot swirl vanes. The large standard deviations of these measurements are a result of a transient heating of the RPL from the beginning of measurement until the flame attaches to the Pilot vanes and the RPL lip had reached a steady state.

Diluted Syngas

The diluted syngas blowout test was performed with RPL equivalence ratios ranging from 0.4 to 1.8 (figure 13).

Again, the trend of lower blowout values for higher RPL equivalence ratios holds (figure 14), in this case extending the minimum stable total equivalence ratio from 0.325 to 0.31. This is a proportionately smaller influence of the RPL on stabilizing the combustion, as compared to methane and pure syngas.

The temperature profile for the different RPL equivalence ratios is similar to that of pure syngas (figure 15), with the exception that all equivalence ratios have their highest temperature at the RPL neck, i.e., combustion in vicinity of the inlet ports. No flashback at the Pilot region is observed.

DISCUSSION

Lean blow out limit

The RPL is shown to have an influence on the stability of the combustion in the burner. As the equivalence ratio of the RPL is increased the LBO is lowered. An increase in equivalence ratio, while the keeping the total flow constant, results in a higher fuel flow and subsequently increases the available chemical energy through the RPL. This together with the recirculated hot gases serves as the ignition source to Pilot and Main premixed flows. Observing the trends of
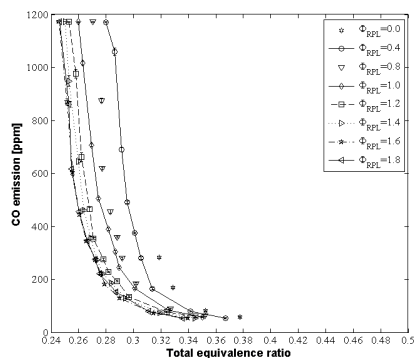

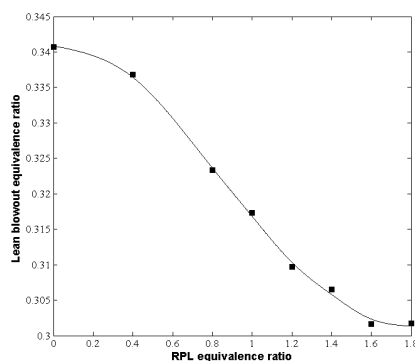**Figure 11 Change of blowout limit for syngas when varying RPL equivalence ratio. Volume flow 0.09 m³/s**

figures 7, 11 and 14, the influence of increasing the equivalence ratio is getting weaker with higher equivalence ratios. This is probably because, even though the chemical energy is increased as stated above, not enough of this energy is released as heat and active radicals at higher equivalence ratios to aid the stabilization of the combustion in the Pilot and Main.

Blow off

In the methane tests blow off was observed when the RPL combustion was pushed out of the RPL at higher equivalence ratios. The flame speed can be assumed to be proportional to the laminar flame speed. Observing figure 2
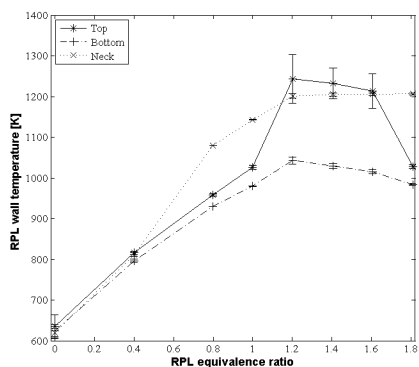
Figure 12 Temperature measurements for syngas. Volume flow 0.09 m³/s

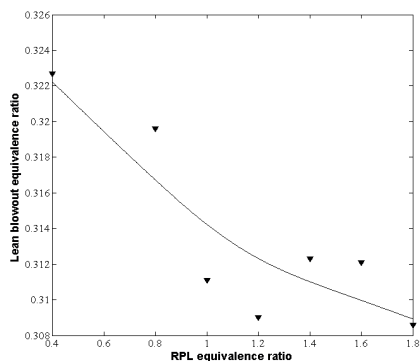**Figure 14 Change of blowout limit for diluted Syngas when varying RPL equivalence ratio Volume flow 0.13 m³/s**

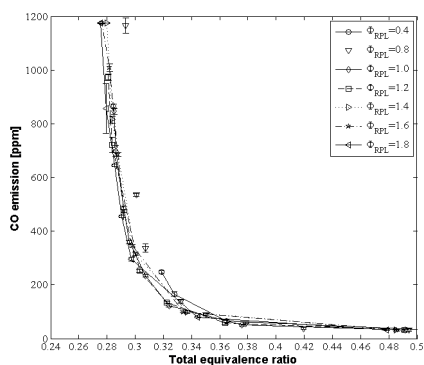**Figure 13 CO emission from lean blowout measurement for diluted syngas. Volume flow 0.13 m³/s**

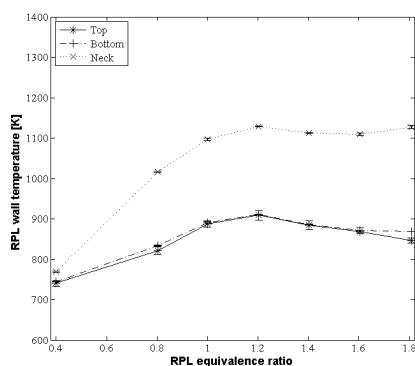**Figure 15 Temperature measurements for diluted Syngas Volume flow 0.13 m³/s**

it can be seen that the laminar flame speed is significantly lower for RPL equivalence ratios 1.6 and 1.8. It is likely, that the unburnt velocity inside the RPL, at these equivalence rations, is larger than the flame speed and as a result pushes the flame out of the RPL. This phenomenon was not observed for the methane tests at 0.14 m³/s and 0.16 m³/s. One explanation could be that the recirculation zone from the Pilot and Main is stronger which keeps the RPL combustion inside the RPL body. Another could be that the higher combustion loading [MW/m³] radiates more heat down into the RPL and increase the reaction rates inside the RPL. This is an issue for further investigation.

Flash back

When the syngas test was performed at high equivalence ratio, flame attachment to the RPL exit lip and the Pilot swirlers where observed. This is considered to be flashback. The reason why it happened with the syngas, and not the other two gases, is that the flame speed is considerably higher for this mixture (figure 2). The flash back occurred at equivalence ratios higher than those that give the highest laminar flame speed. A reason for this could be that the rich combustion exhaust from the RPL diffuse/mix with the Pilot premixed stream. The intermediate mixture will consist of a range of equivalence ratios. Depending on the amount of mixing a different peak flame speed may be present.

CONCLUSIONS

The lean blowout limit of three fuels has been examined in a scaled DLE burner at different RPL equivalence ratios. The experiments were conducted at atmospheric pressure and a inlet temperature of 650 K.

Improvements on the lean stability limit can be achieved by increasing the equivalence ratio in the RPL. For methane this will, at high RPL equivalence ratios, force the flame out of the RPL. The syngas fuels did not show this behavior due to the high hydrogen content. For the syngas fuels, thermocouples indicated that the flame inside the RPL was close to the premixed inlet.

The blowout limit of the syngas mixtures was significantly lower than the methane mixture due to the high hydrogen contents and all blowout limits could be predicted using PSR model.

The higher flame speed of the undiluted syngas mixture caused the Pilot combustion to attach to the Pilot swirlers and the exit lip of the RPL for RPL equivalence ratios close to the peak laminar flame speeds.

ACKNOWLEDGEMENTS

REFERENCES

[1] Moliere, M., 2002, "Benefiting from the Wide Fuel Capability of Gas Turbines: A Review of Application Opportunities," ASME Conference Proceedings

[2] Klimstra, J., 1986, "Interchangeability of Gaseous Fuels--the Importance of the Wobbe-Index," SAE transactions, 95(6)

[3] Lieuwen, T., Mcdonell, V., Petersen, E., and Santavicca, D., 2008, "Fuel Flexibility Influences on Premixed Combustor Blowout, Flashback, Autoignition, and Stability," Journal of Engineering for Gas Turbines and Power, 130(1)

[4] Eriksson, P., Genrup, M., Jonshagen, K., and Klingmann, J., 2009, "Off-Design Performance Investigation of a Low Calorific Gas Fired Two-Shaft Gas Turbine," ASME Conference Proceedings, 2009(48852)

[5] Sigfrid, I. R., Whiddon, R., Aldén, M., and Klingmann, J., 2011, "Parametric Study of Emissions from Low Calorific Value Syn-Gas Combustion, with Variation of Fuel Distribution, in a Prototype Three Sector Burner.," ASME Conference Proceedings, 2011

[6] Warnatz, J., Dibble, R. W., Maas, U., and Springerlink (Online Service), 2006, Combustion Physical and Chemical Fundamentals, Modeling and Simulation, Experiments, Pollutant Formation,

[7] Zeldovich, Y. B., 1946, "The Oxidation of Nitrogen in Combustion and Explosions," Acta Physicochimica USSR, 21(4)

[8] Walsh, P. P., and Fletcher, P., 2004, Gas Turbine Performance, Blackwell, Oxford.

[9] Andersen, B. W., 2001, The Analysis and Design of Pneumatic Systems, Krieger

[10] Goodwin, D. G., 2003, "Proceedings of Cvd Xvi and Eurocvd Fourteen, Electrochem. Soc.," eds., pp. 155–162.

[11] Dars – Software for Digital Analysis of Reactive Systems. Diganars, D., USA, (http://www.Diganars.Com), 2009

[12] Sigfrid, I. R., Whiddon, R., Collin, R., and Klingmann, J., 2010, "Experimental Investigation of Laminar Flame Speeds for Medium Caloricic Gas with Various Amounts of Hydrogen and Carbon Monoxide Content at Gas Turbine Temperatures " ASME Conference Proceedings, 2010

[13] Smith, G. P., Golden, D. M., Frenklach, M., Moriarty, N. W., Eiteneer, B., Goldenberg, M., Bowman, C. T., Hanson, R. K., Song, S., Gardiner Jr, W. C., Lissianski, V. V., and Qui, Z., 1999, "Gri-Mech 3.0," (http://www. me. berkeley. edu/gri_mech)

[14] 2006, "San Diego Mechaism," (http://maeweb. ucsd.edu/~combustion/cermech/)

[15] Jarnekrans, D., 2007, "Combustion Characteristics of Mcv/Lcv Fuels - a Numerical Chemical Kinetics Study at Gas Turbine Conditions " Ph.D. thesis, Lund University, Lund

[16] Kee, R. J., Coltrin, M. E., and Glarborg, P., 2003, Chemically Reacting Flow : Theory and Practice, Wiley, New York

[17] Lefebvre, A. H., 1999, Gas Turbine Combustion, Taylor & Francis, New York

Paper III

GT2011-45689

PARAMETRIC STUDY OF EMISSIONS FROM LOW CALORIFIC VALUE SYN-GAS COMBUSTION, WITH VARIATION OF FUEL DISTRIBUTION, IN A PROTOTYPE THREE SECTOR BURNER

Ivan R. Sigfrid
Department of Energy Sciences
Lund University
Sweden

Ronald Whiddon
Department of Combustion Physics
Lund University
Sweden

Marcus Aldén
Department of Combustion Physics
Lund University
Sweden

Jens Klingmann
Department of Energy Sciences
Lund University
Sweden

ABSTRACT

The emission composition is measured for a prototype burner while varying the equivalence ratio in discrete portions of the burner. The burner is a three sector system, consisting of a separate igniter, pilot/stabilizer and main burner. The design allows for discrete control of equivalence ratio in each of the three sectors. The ignition sector, designated RPL (Rich-Pilot-Lean), operates from rich to lean equivalence values, and serves to ignite the pilot sector, which, in turn, stabilizes the main combustion sector. All three burner sections are premixed. The burner is operated at atmospheric pressure with inlet flows heated to 650 K (±8 K). Tests were performed for three gases: methane, a model syngas (10% CH_4, 22.5% CO, 67.5% H_2), and dilute syngas. The dilute gas includes sufficient nitrogen to lower the heating value to 15 MJ/m^3. The model syngas and diluted syngas are representative of fuels produced by gasification process. The burner emissions, specifically, CO, CO_2, O_2 and NO_x, are measured while holding the RPL equivalence value constant and varying the equivalence ratio of the pilot and main sectors. The equivalence ratios for pilot and main sectors are chosen such that the total burner equivalence ratios remain constant during a test sequence. The target total equivalence ratio for each gas is chosen such that all experiments should have the same flame temperature.

INTRODUCTION

Minimization of pollutive emissions is a continuing goal of power source designers, both to meet legislative mandates [1] and for environmental conservation. Anthropogenic CO_2 emissions are currently targeted for reduction, which can practically be minimized in two ways; CO_2 can be stored in physical or chemical sink [2] and fuels that are considered CO_2 neutral can be burnt. CO_2 neutral fuels have various sources and component makeups; burning these non standard fuels necessitates a flexible combustor that can handle a wide range of fuels.

While CO_2 is a primary product of combustion, NO and NO_2 (collectively NO_x) are negative byproducts of combustion. NOx is both a local pollutant, contributing to smog and acid rain, and also a catalyst in the removal of ozone from the stratosphere [3]. There are several combustion reaction pathways that lead to NO_x formation. Two are most prominently associated with NO_x emissions for combustion under gas turbine conditions. One of these is the Fenimore mechanism, which is the reaction of CH radicals with N_2 to form HCN which then further oxidizes to NO [4]. As CH radicals form early in the hydrocarbon combustion process, this mechanism is also known as prompt NO_x. A second is the

Table 1 Compositions of the gases examined

Gases	Gas compositions vol.%				W* [MJ/m³]	LHV [MJ/kg]	Fuel/Air$_{St}$
	CH$_4$	H$_2$	CO	N$_2$			
Ref.	100	0	0	0	55.30	50.01	0.0584
Syngas	10	67.5	22.5	0	27.70	33.14	0.104
Diluted Syngas	6.9	46.56	15.52	31.02	15.00	14.05	0.245

*Wobbe index based on the higher heating value (HHV).

Zeldovich mechanism, which produces NO from the oxidation of thermally generated nitrogen radicals [5]. This `thermal NO_x' is the main mechanism of NO_x production in high temperature combustion, e.g., gas turbine combustion. Under certain conditions the other pathways can contribute appreciably to NO_x emissions; for instance, the Nitrous oxide pathway, which is significant at lean conditions [6, 7].

When designing a combustor that can be fueled with CO_2 neutral fuels, the NO_x emissions should not be neglected. This investigation is a parametric study of emissions using different fuels and fuel distributions in a scaled 4th generation dry low emission burner. Specifically, the concentrations of CO and NO_x are monitored while running the burner on three types of gaseous fuel, and for each fuel, varying the distribution to specific regions of the burner. While not typically a major pollutant in gas turbines, CO values are used herein as an indication of combustion quality, as its presence can indicate incomplete combustion or impending blowout [8]. CH_4 is used as the reference fuel, as it is the primary component of natural gas, a commonly used fuel in gas turbines. The other fuel examined is a syngas with high H_2 and CO content (Table 1) [9]. This fuel is also examined when diluted to a Wobbe index of 15 MJ/m^3. It can be considered a typical gasification gas [10].

EXPERIMENTAL SETUP

Burner

The burner under investigation is a prototype of a 4th generation DLE syngas burner designed by Siemens Industrial Turbomachinery (Figure 1). The burner is a three sector design with separate ignition, stabilization and bulk combustion sectors. Fuel flow to each of these sectors is individually controlled.[1] The ignition sector, RPL (Rich-Pilot-Lean), houses the spark ignition source and has isolated fuel and air feeds. Swirl is introduced in the base of the RPL by using angled inlet ports. The stabilization sector, Pilot is positioned between the RPL and bulk combustion sector. The Pilot air flow shrouds the RPL, with fuel being added just below the swirl vanes at the burner throat. The short distance between fuel injection and the combustion zone results in the Pilot probably not being fully premixed. The bulk combustion sector, Main, is the outermost of the three sectors. Fuel is added sufficiently upstream of the burner throat that the Main can be considered fully premixed. The prototype burner has a conical dump extension (quarl) that is coupled to a steel cylindrical liner, which contracts to ~50% of liner cross sectional area at the exit. The cylindrical liner, (size 85 mm x 700 mm) was constructed so that an adequate residence time (~15 ms) and a combustor loading [11] below 10 kg/s atm$^{1.8}$m^3 was obtained [8].

Air and Fuel system

The high volume air supply from two Rietschle SAP 300 blowers is divided between the Pilot and Main burner sectors,
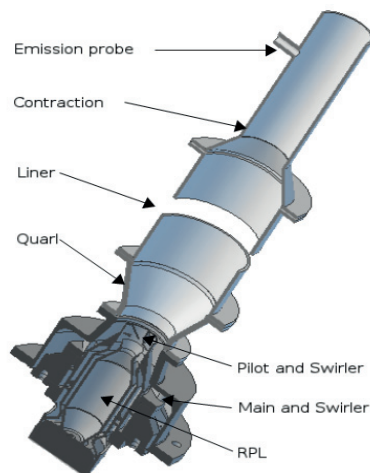
Figure 1: Burner Assembly

with 21% going to the Pilot and 79% to the Main [8]. Blower output is varied by controlling the line frequency with a Vacon OYJ variable AC driver. The AC driver is interfaced using a Velleman 8055 A/D convertor, allowing control of the bulk air flow. A precise flow rate for the bulk air flow is measured by two Eldridge MPNH-8000 thermal mass flow meters mounted just downstream of the blowers. The mass flow range for the blower system is from 0 to 110 g/s when combustion is absent. A separate air feed is supplied to the RPL sector from a compressed air source, controlled using an Alicat Scientific mass flow controller. All air supplies are heated to a temperature of 650 K (± 8 K) before entering the burner. Fuel supplies are controlled individually for each of the three sectors; the flows are controlled using Alicat Scientific mass flow controllers. Equivalence ratios computed from the measured O_2 and CO_2 values (assuming complete combustion) were within 5% of the equivalence ratios indicated by the measured mass flow rates. The three fuels tested were purchased preblended in 50 liter gas cylinders. The fuel compositions and selected properties are found in table 1.

Emissions Tracking

Samples are collected 5 cm upstream from the dump plane of the liner, after the contraction. The sampling rake is a 6 mm diameter, closed end, steel tube that lays perpendicular to the effluent flow, across the center of the liner outlet. There are eight 1.0 mm holes drilled at equally spaced intervals along the tube, which collect an averaged sample across the entire exhaust stream. The sample gas travels along a 50 cm length of steel tubing, and then ~3 m of unheated polymer tubing to the measurement rack. Directly on entry to the emissions rack, the sample is passed through a cooled condenser, to remove water from the sample. The response time for measurements is 25 seconds for NO_x measurements and 6

---

[1] Since equivalence ratio can be set in each of the three burner sectors, the respective values are referred to by the sector name, e.g., "Pilot equivalence ratio". The net equivalence ratio is referred to with, "total equivalence ratio".
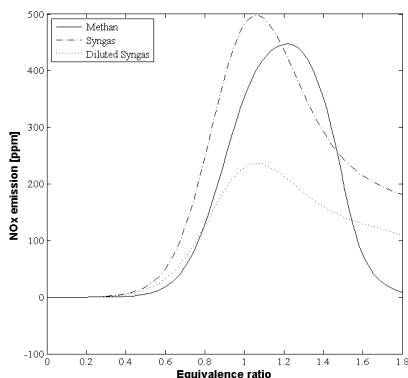
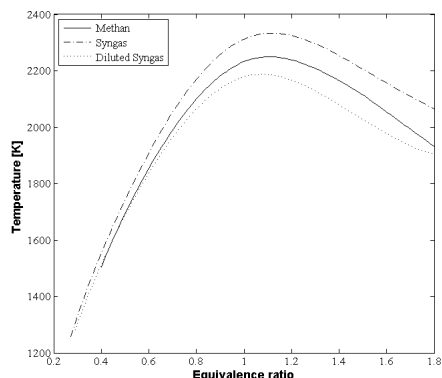**Figure 2: NOx emissions from PSR, 1.5 ms residence time**

Figure 3: Temperature from PSR, 1.5 ms residence time

seconds for all other species. Values from each analytical instrument are recorded at 1 second intervals.

CO and CO_2 are measured using a Rosemount Analytical Binos 100 gas analyzer. The measurement range is 0-1000 ppm and 0-20% for CO and CO_2 respectively. The stated uncertainty, from measurement of calibration gas, is <1% full scale reading for both CO and CO_2. The instrument was calibrated daily with 0 and 103 ppm CO, and 0 and 8% CO_2.

NO_x measurements were made using an Eco Physics model 700 EL-ht nitric oxide measurement instrument, with a range of 0.1-100 ppm NO_x. The error in measurements for all nitrogen oxides measured was found to be ~ 0.1% full scale. The NO_x meter was calibrated daily with 30 ppm NO_x.

Oxygen is measured with a Rosemount Analytical Oxynos 100. The instrument measurement span was set to 0 to 25% dry oxygen. The O_2 meter was calibrated daily with 0 and 21% O_2 (nitrogen and air).

EXPERIMENTAL PROCEDURE

In order to evaluate the contribution of different burner sectors to total emission levels, it was necessary to isolate each sector while maintaining a reasonable total adiabatic flame temperature. Investigation of the lean blowout limit effectively isolated the RPL component of emissions, while a second experiment focused on the Pilot and Main sectors by varying only the fuel splitting between the Pilot and Main sectors, all other variables held constant. For all tests, the flow through the RPL was the same, i.e. ~2.4% of the total flow in the methane test. The flow rates of the unburnt gas in the experiments were 0.12 m^3/s for methane; 0.09 m^3/s for syngas and 0.13 m^3/s for diluted syngas.

Lean Stability Sweep

Emissions levels were recorded in conjunction with an investigation of the burner lean blowout limit [8]. Tests were performed by igniting the burner at a specific RPL equivalence ratio and an arbitrary total equivalence ratio that gave stable combustion. During the test, the Pilot and Main equivalence ratios were kept equal to one another at all times, while the RPL equivalence ratio was kept static. The Pilot and Main equivalence ratios were reduced in equal measure until the burner was unable to sustain combustion: indicated when two consecutive tests gave an off-scale CO value or the flame extinguished. Measurements were recorded for each equivalence ratio, and this process was repeated for each of the fuels, and for several RPL equivalence ratios.

Fuel Partitioning

Emissions were measured while varying the relative fuel flow to the Pilot and Main burner sectors. The total equivalence ratio, corresponding to an adiabatic flame temperature of 1700 K, was held constant for each test. The respective total equivalence ratios were: methane 0.47, syngas 0.40 and dilute syngas 0.41. For all tests, the RPL equivalence ratio of 0.80 was maintained, and the remaining fuel necessary to reach the desired total equivalence ratio was supplied to the Pilot and Main sectors. The test began by setting the Pilot fuel flow controller to the highest achievable flow (mass flow controller limited), with the balance of fuel going to the Main burner region. The test proceeded by reducing the Pilot fuel flow in 0.1 g/s increments, and adding that same amount of fuel to the Main sector. Measurements were recorded at each increment until either blowout or zero flow in the Pilot Sector.

Table 2 NOx Reaction flow analysis

Gases	Equivalence ratio	Reaction flow%			
		Nitrous Oxide	NNH	Prompt NO$_x$	Thermal NO$_x$
Ref.	0.47	53.7%	29%	7.2%	10.1%
	1.21	-1.3%	3.3%	54.8%	43.2%
	1.40	0%	-1.0%	67.4%	38.66%
Syngas	0.45	39.5%	52.5%	1.3%	6.7%
	1.05	5.3%	14.1%	6.4%	74.2%
	1.40	0.0%	17.3%	32.4%	50.3%
Diluted	0.48	36.2%	55.5%	1.6%	6.7%
Syngas	1.05	4.7%	25.6%	10.4%	59.3%
	1.40	9.9%	20.9%	30.2%	39.0%

MODELLING

The RPL NO$_x$ emission was modeled by an adiabatic, non-isothermal perfectly stirred reactor (PSR) [12] , which should accurately model the behavior of the RPL primary recirculation zone[13]. For this analysis, GRI 3.0 [14] was used as the chemical kinetic model for each fuel, with DARS software [15]. The residence time was set to 1.5 ms to get a similar NO$_x$ response as in figure 7. It can be seen that there is a difference in where the modeled and measured NO$_x$ emissions peak, this was allowed because there is expected to be a diffusive combustion of the unburnt fuel in rich equivalence ratios giving rise to a higher NO$_x$ production. It should be noted that the PSR reactor can only be considered applicable in the strongly recirculated primary zone. The secondary zone is not modeled in this investigation. The predicted NO$_x$ level for each gas as a function of RPL equivalence ratio is shown in figure 2, while the predicted temperatures relation is shown in figure 3. The PSR model was repeated using DARS. The DARS software was used to estimate the contribution to total NO$_x$ (reaction flow%) of the various NO$_x$ pathways included in the GRI 3.0 mechanism (Table 2). The three mentioned NO production pathways, prompt, thermal and nitrous oxide, are shown. Also included is a fourth pathway, NNH, which is found to be important in high H$_2$ fuel combustion [16]. The reaction flow% is reported at three equivalence ratios for each fuel. The first, lowest equivalence ratio is at 1650 K adiabatic flame temperature, the middle equivalence ratio is the peak modeled flame temperature, and the last equivalence ratio is common between all three fuels.

RESULTS

Lean Stability Sweep

The CO emissions resulting from the combustion of dilute syngas are shown in Figure 4. The result is characteristic of all the gases tested, with the only variation being the equivalence ratio of blow out. At the lean blowout limit, CO
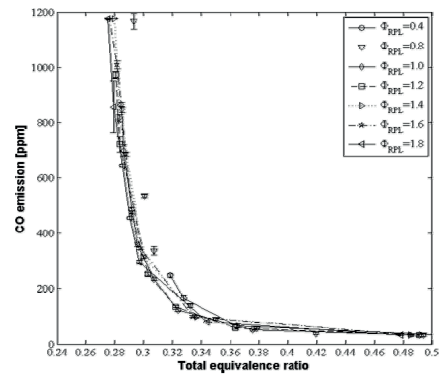

Figure 4: Dilute syngas, CO emission with total equivalence ratio for relevant RPL equivalence ratios.

emission is high, but it quickly reaches a low plateau when operating in stable, lean combustion.

NOx values from the same series of tests are shown in figures 5, 6 and 7; for methane, syngas and dilute syngas, respectively. Each figure shows an increase of NOx as total equivalence ratio increases; methane having the steepest response, syngas and diluted syngas approximately equal (note axis values).

The RPL has different response depending on the fuel used. Syngas and diluted syngas both have their peak NO$_x$ emission at equivalence ratios slightly below 1.2. The NO$_x$ response for Methane is increasing until an equivalence ratio of 1.7. The trend is seen more clearly when looking at measurements with adiabatic flame temperature of 1650 K shown relative to specific RPL equivalence ratios (Figure 8).
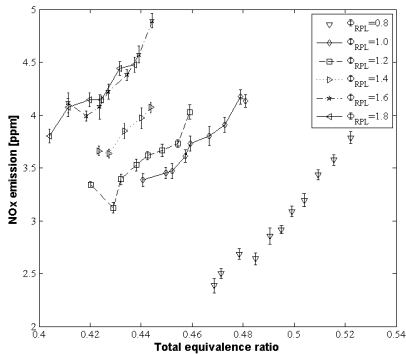
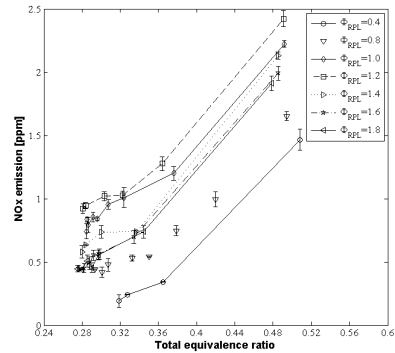**Figure 5: Methane, NO$_x$ emission with total equivalence ratio for relevant RPL equivalence ratios.**

Figure 7: Dilute syngas, NO$_x$ emission with total equivalence ratio for relevant RPL equivalence ratios.
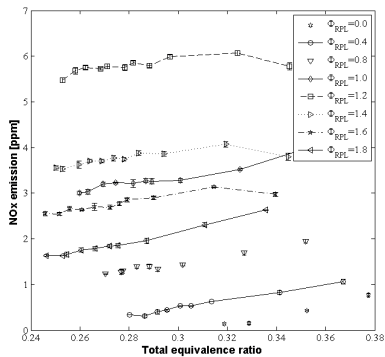

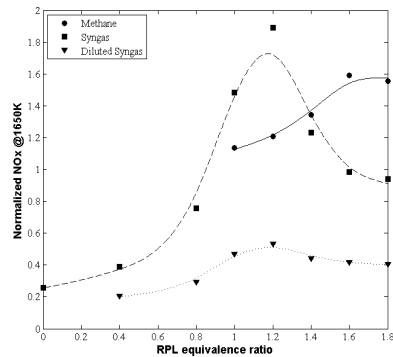**Figure 6: Syngas, NO$_x$ emission with total equivalence ratio for relevant RPL equivalence ratios.**

Figure 8: NO$_x$ emission for relevant RPL equivalence ratios, total flame temperature 1650 K.

Fuel Partitioning

Measurements of CO during fuel partitioning experiments did not show any appreciable variance over the range of tested parameters. It was possible to run the burner with no fuel supplied to the Pilot when using diluted syngas, and for syngas, combustion persisted with both the RPL and Pilot extinguished. Even in these extreme cases, there was no change in CO emission that could be distinguished from measurement uncertainty.

The measured NOx emissions showed a dependence on the fuel distribution between the Pilot and Main burner regions (Figure 9). The x axis values are the ratio of the Pilot equivalence ratio to the total equivalence ratio. To the right of

the x value: 1, the Pilot equivalence ratio is higher than the Main. Maximum measured Pilot equivalence ratios, limited by the range of the mass flow controller, were approximately 1.75, 0.62 and 0.90 for methane, syngas and diluted syngas, respectively. For x values less than 1 the Main equivalence ratio is higher than the Pilot. For the two syngas fuels it was possible to run the burner without the Pilot. A magnification showing values less than one is seen in Figure 10.

DISCUSSION

Relating the response of emissions to variations in burner operation sheds light on individual sector contribution to total emissions production. However, interactions of the three combustor sectors occlude direct cause effect relationships.
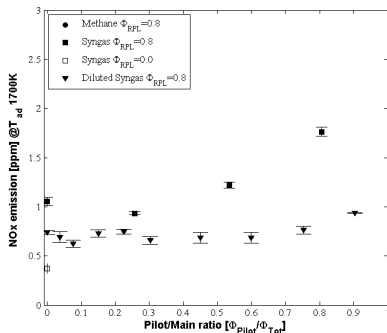
Figure 9: NOₓ emission, fuel partition weighted to Main burner sector.
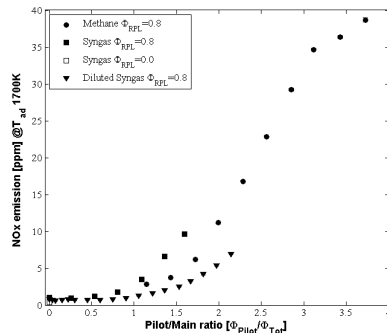

Figure 10: NOₓ with fuel partitioning, Pilot divided by total equivalence ratio.

At all practical operating points, no difference in CO was found, within the limit of instrumental accuracy. This indicates that for the conditions tested, combustion had reached approximately the same degree of completion in the time it took to reach the liner exit. Also, all tests showed a remnant of CO in the exhaust. While this is not common in gas turbine combustion, it most likely arises in these experiments from wall cooling in the uninsulated liner. NO_x showed a strong dependence on the tested parameters, whether type of fuel, equivalence ratio or distribution.

RPL NOx emission

The RPL is the least significant of the three burner sectors when considering the volume of fuel and air that pass through it, in this investigation ~2.4% of the total flow. It is remarkable that the RPL has such a large effect on total NO_x. By isolating the total equivalence ratios for an adiabatic flame temperature of 1650 K, NO_x is seen essentially as a function of the RPL equivalence ratio (Figure 8). Variation in the RPL equivalence ratio gave a large relative change in NO_x, especially for syngas, where levels increased almost six fold. This is also observed in the modeled PSR (Figure 2). This indicates a dominance of the thermal NO_x pathway in NO_x formation for syngas; for methane, thermal NO_x and prompt NO_x have similar contributions (table 2). This is due to low residence time and subsequently incomplete combusting. Increasing the PSR residence time move the peak NO_x towards equivalence ratio 1 and the thermal NO_x becomes the prominent path. Low total equivalence ratios for the burner mean that the bulk of fuel is combusted in an environment where the Nitrous oxide and NNH pathway are most important (table 2).

The RPL related NO_x was found to vary for each of the three fuels investigated. For syngas and diluted syngas, the highest NOx measurements were found near the RPL equivalence ratio 1.2 (Figure 8). This is in vicinity of the highest combustion temperatures predicted by the PSR model (Figure

3). The difference in NO_x emission between the two syngas fuels is again linked to the thermal NO_x pathway. The low flame temperature of diluted syngas greatly reduces the amount of NO_x production. For methane, NO_x emission levels were similar to syngas; however, methane NO_x emissions did not fall off at high equivalence ratios. Instead, NO_x emission increased steadily until leveling off at an equivalence ratio of 1.60. The PSR model shows that with short residence times, the NO_x peak for methane is expected at higher equivalence ratios than for syngas (figure 2). Essentially, methane does not react quickly enough to reach complete combustion during the RPL residence time. As a result, at high RPL equivalence ratios the RPL flame moves outside the RPL volume and combusts as a partial diffusion flame in the lean environment of the burner [8].

Pilot NOx Emission

Due to the strong interaction of the Pilot and Main sectors, it is impractical to consider them as completely separate. However, the fuel splitting experiment emphasizes the contribution of the Pilot sector to the total NO_x level, as any change in the Pilot equivalence ratio has 1/4 the effect on Main equivalence ratio. All fuels showed a quick increase in the NO_x emission as the Pilot equivalence ratio increased, which is reasonable given the dominance of the thermal NO_x pathway in total NO_x production, when moving towards higher flame temperatures. Although it was not determined for the syngas fuels, methane NO_x emission is increasing with equivalence ratio until approximately 1.60 where it begins to level off. This might be attributed to the mixing layer between the rich Pilot and lean Main flows, which should feature intermediate equivalence ratios, i.e., high combustion temperature. As mentioned, the Pilot is not expected to have complete mixedness, meaning that the equivalence ratio is not uniform, but rather a distribution of local equivalence ratios around a mean value [17, 18]. This effect can be seen by examining the syngas NO_x emissions values shown in figure 10. Ignoring effects of interaction

between the burner sectors, the NO_x contribution from the Main should be less than 0.5 ppm ("open square") the NO_x value with the RPL equivalence ratio of 0.80 is about 1.1 ppm (closed square x=0), the NO_x value when the Main and Pilot are equal and the RPL is 0.80 is about 2.5 ppm (estimation). The result is that the Pilot, which flows 1/4 as much as the Main sector, with the same lean equivalence ratio, produces almost 3 times the NO_x.

CONCLUSIONS

CO emissions indicate that the combustion is complete when operating sufficient distance from the blow out limit.

The RPL is a large contributor to NO_x, in spite of having a relatively low flow.

For the syngas fuels there is a peak NOx production where the RPL equivalence ratio show the highest combustion temperature.

Methane does not show highest NO_x at the calculated highest combustion temperature, this is because the combustion is not complete inside the RPL for this RPL flow.

The Pilot is found to give slightly higher than expected NO_x emissions.

The Dilute Syngas gave the lowest NO_x emissions indicating that the high concentration of N_2 and subsequently lower flame temperature inhibits the formation of NO_x.

ACKNOWLEDGEMENTS

REFERENCESReferenser

[1] Bowman, C. T., 1992, "Control of Combustion-Generated Nitrogen Oxide Emissions: Technology Driven by Regulation," Symposium (International) on Combustion, 24(1), pp. 859-878

[2] Bachu, S., Gunter, W. D., and Perkins, E. H., 1994, "Aquifer Disposal of Co2: Hydrodynamic and Mineral Trapping," Energy Conversion and Management, 35(4), pp. 269-279

[3] Crutzen, P. J., 1971, "Ozone Production Rates in an Oxygen-Hydrogen-Nitrogen Oxide Atmosphere," J. Geophys. Res., 76(30), pp. 7311-7327

[4] Fenimore, C. P., 1971, "Formation of Nitric Oxide in Premixed Hydrocarbon Flames," Symposium (International) on Combustion, 13(1), pp. 373-380

[5] Zeldovich, Y. B., 1946, "The Oxidation of Nitrogen in Combustion and Explosions," Acta Physicochimica USSR, 21(4), pp. 577-628

[6] Nicol, D. G., Steele, R. C., Marinov, N. M., and Malte, P. C., 1995, "The Importance of the Nitrous Oxide Pathway to No[Sub X] in Lean-Premixed Combustion," Journal of Engineering for Gas Turbines and Power, 117(1), pp. 100-111

[7] Richards, G. A., Mcmillian, M. M., Gemmen, R. S., Rogers, W. A., and Cully, S. R., 2001, "Issues for Low-Emission, Fuel-Flexible Power Systems," Progress in Energy and Combustion Science, 27(2), pp. 141-169

[8] Sigfrid, I. R., Whiddon, R., Aldén, M., and Klingmann, J., 2011, "Experimental Investigation of Lean Stability Limit of an Prototype Syngas Burner for Low Calorific Value Gases," ASME Conference Proceedings, 2011

[9] Sigfrid, I. R., Whiddon, R., Collin, R., and Klingmann, J., 2010, "Experimental Investigation of Laminar Flame Speeds for Medium Caloricic Gas with Various Amounts of Hydrogen and Carbon Monoxide Content at Gas Turbine Temperatures " ASME Conference Proceedings, 2010

[10] Moliere, M., 2002, "Benefiting from the Wide Fuel Capability of Gas Turbines: A Review of Application Opportunities," ASME Paper# GT-2002-30017

[11] Walsh, P. P., and Fletcher, P., 2004, *Gas Turbine Performance*, Blackwell, Oxford

[12] Kee, R. J., Coltrin, M. E., and Glarborg, P., 2003, *Chemically Reacting Flow : Theory and Practice*, Wiley, New York.

[13] Hermann, F., Klingmann, J., and Gabrielsson, R., 2003, "Computational and Experimental Investigation of Emissions in a Highly Humidified Premixed Flame," ASME Conference Proceedings, 2003(36843), pp. 819-827

[14] Smith, G. P., Golden, D. M., Frenklach, M., Moriarty, N. W., Eiteneer, B., Goldenberg, M., Bowman, C. T., Hanson, R. K., Song, S., Gardiner Jr, W. C., Lissianski, V. V., and Qui, Z., 1999, "Gri-Mech 3.0," (http://www.me.berkeley.edu/gri_mech)

[15] Dars – Software for Digital Analysis of Reactive Systems. Diganars, D., USA, (http://www.Diganars.Com), 2009

[16] Guo, H., Smallwood, G. J., Liu, F., Ju, Y., and Gülder, Ö. L., 2005, "The Effect of Hydrogen Addition on Flammability Limit and Nox Emission in Ultra-Lean Counterflow Ch4/Air Premixed Flames," Proceedings of the Combustion Institute, 30(1), pp. 303-311

[17] Mongia, R. K., Tomita, E., Hsu, F. K., Talbot, L., and Dibble, R. W., 1996, "Use of an Optical Probe for Time-Resolved in Situ Measurement of Local Air-to-Fuel Ratio and Extent of Fuel Mixing with Applications to Low Nox Emissions in Premixed Gas Turbines," Symposium (International) on Combustion, 26(2), pp. 2749-2755

[18] Shih, W.-P., Lee, J. G., and Santavicca, D. A., 1996, "Stability and Emissions Characteristics of a Lean Premixed Gas Turbine Combustor," Symposium (International) on Combustion, 26(2), pp. 2771-2778

Paper IV

GT2010-22275

EXPERIMENTAL INVESTIGATION OF LAMINAR FLAME SPEEDS FOR MEDIUM CALORIFIC GAS WITH VARIOUS AMOUNTS OF HYDROGEN AND CARBON MONOXIDE CONTENT AT GAS TURBINE TEMPERATURES

Ivan R. Sigfrid
Department of Energy Sciences
Lund University
Sweden

Ronald Whiddon
Department of Combustion Physics
Lund University
Sweden

Robert Collin
Department of Combustion
Physics
Lund University
Sweden

Jens Klingmann
Department of Energy Sciences
Lund University
Sweden

ABSTRACT

It is expected that, in the future, gas turbines will be operated on gaseous fuels currently unutilized. The ability to predict the range of feasible fuels, and the extent to which existing turbines must be modified to accommodate these fuels, rests on the nature of these fuels in the combustion environment. Understanding the combustion behavior is aided by investigation of syngases of similar composition. As part of an ongoing project at the Lund University Departments of Thermal Power Engineering and Combustion Physics, to investigate syngases in gas turbine combustion, the laminar flame speed of five syngases (see table) have been measured.

The syngases examined are of two groups. The first gas group (A), contains blends of H_2, CO and CH_4, with high hydrogen content. The group A gases exhibit a maximum flame speed at an equivalence ratio of approximately 1.4, and a flame speed roughly four times that of methane. The second gas group (B) contains mixtures of CH_4 and H_2 diluted with CO_2. Group B gases exhibit maximum flame speed at an equivalence ratio of 1, and flame speeds about 3/4 that of methane.

A long tube Bunsen-type burner was used and the conical flame was visualized by Schlieren imaging. The flame speeds were measured for a range of equivalence ratios using a constrained cone half-angle method. The equivalence ratio for measurements ranged from stable lean combustion to rich combustion for room temperature (25°C) and an elevated temperature representative of a gas turbine at full load (270°C).

The experimental procedure was verified by methane laminar flame speed measurement; and, experimental results were compared against numerical simulations based on GRI 3.0, Hoyerman and San Diego chemical kinetic mechanisms using the DARS v2.02 combustion modeler. On examination, all measured laminar flame speeds at room temperature were higher than values predicted by the aforementioned chemical kinetic mechanisms, with the exception of group A gases, which were lower than predicted.

Gases	Gas compositions vol.%				W* [MJ/m³]	LHV [MJ/kg]
	CH_4	H_2	CO	CO_2		
Ref.	100	0	0	0	55.30	50.01
A1	10	45	45	0	21.71	20.93
A2	10	67.5	22.5	0	27.70	33.14
B1	64.4	0	0	35.6	28.15	19.87
B2	60.06	5.08	0	35.32	27.51	19.65
B3	57.2	10.6	0	32.74	27.60	20.36

*Wobbe index based on the higher heating value (HHV).

INTRODUCTION

As the demand for energy increases, and carbon neutral energy becomes important, there will be a move to supplement or replace existing fuels with environmentally sound fuels. A component of this shift will be evidenced in moving gas turbines from traditionally sourced fuels, i.e., natural gas, to gases that are CO_2 neutral.

A wide range of fuels are suitable for the gas turbine engine, and will warrant interest [1]. For instance, digester gas, considered CO_2 neutral, has as the major component methane, and can be burned in gas turbines directly or blended with natural gas to make synthetic natural gas [2]. Alternatively, syngases, such as those produced by coal gasification, could be used to power gas turbines [1]. But, as the makeup of syngas is a process dependant blend of hydrogen, carbon monoxide, methane and other components [1], integration of syngas as a fuel source is necessarily less straightforward than digester gas. The demand rests on the gas turbine community to investigate new fuels and expand the energy pool.

In order to use nontraditional fuels, which have a range of heating values [3], it is essential to know the fundamental combustion properties of the fuels. Laminar flame speed is one of these combustion properties that yield information about reactivity, diffusivity and exothermicity of the gas.

Several studies of laminar flame speed for syngases have been done previously [4-8]. The investigation by Natarajan et al. of laminar flame speed for syngas mixtures [6] showed good agreement, at low hydrogen content, with reaction mechanisms for hydrogen and carbon monoxide [9] as well as single carbon molecules [10]. The agreement extends to conditions similar to gas turbine combustion. Improvements to the hydrogen combustion kinetic mechanism are being addressed [11].

In this work, the laminar flame speeds for two sets of gases have been measured by applying a constrained half-angle method to Schlieren images of the flame. The first set of gases (A, table 1) correspond to syngas from coal gasification [1]. For the second set of gases (B, table 1), gas B1 is typical of digester gas, whereas B2 and B3 were chosen to investigate the effect of hydrogen enrichment on flame speed. Methane was used as a reference gas for validation of the experimental procedure.

Laminar flame speeds were measured at two temperatures for equivalence ratios from rich to the lean blow off limit. In addition to room temperature (25°C), measurements were made at a temperature similar to gas turbine operating conditions (270°C). The data is compared with simulations based on the GRI 3.0 mechanism [12], the San Diego mechanism [13], and a Hoyerman developed mechanism [14].

Table 1 Compositions of the gases examined

Gases	Gas compositions vol.%				W* [MJ/m³]	LHV [MJ/kg]
	CH_4	H_2	CO	CO_2		
Ref.	100	0	0	0	55.30	50.01
A1	10	45	45	0	21.71	20.93
A2	10	67.5	22.5	0	27.70	33.14
B1	64.4	0	0	35.6	28.15	19.87
B2	60.06	5.08	0	35.32	27.51	19.65
B3	57.2	10.6	0	32.74	27.60	20.36

*Wobbe index based on the higher heating value (HHV).

NOMENCLATURE

A	Area
A_n	Burner nozzle cross sectional area
Re	Reynolds number
S_L	Laminar flame speed
T	Temperature
$\dot{V}$	Volume flow
r	Burner radius
t	Time
u	Upstream velocity
u_B	Upstream bulk velocity

Greek letters

α	Flame half-angle
κ	Stretch
ϕ	Equivalence ratio

Subscripts

B	Bulk
L	Laminar
n	Nozzle
u	Unburnt

EXPERIMENTAL SETUP

The burner used in this experiment was a Bunsen type burner with a 500 mm mixing length. The burner tip is interchangeable, and three burner tip diameters were used in experimentation: 4.1, 10.13 and 13 mm. The burner tip was selected to ensure stable combustion.

For measurements made at elevated temperature, the entire burner was surrounded by a resistive coil heater and insulated. The air line was coiled around the burner tube, and mixed with fuel at the base of the burner tube. The heating coil was operated by a Eurotherm controller with an attached thermocouple registering the heat around the burner tube. Experimental temperatures were verified by measuring the temperature of the gas exiting the burner tip.

Fuel-air mixtures were regulated by a pair of Bronkhorst thermal mass flow controllers. Prior to use, the flow controllers were calibrated for each gas blend by relating the bulk flow to PIV measurements. The error of the meters did not exceed 5%. PIV was also used to determine the radially dependant flow distribution at the burner tip.

The flame cone image was recorded by a Schlieren imaging assembly in a Z type configuration (Figure 1). Light was supplied to the setup by a 150 watt halogen gooseneck lamp (L). A 1.5 mm iris (I) was used to emulate a point light source as well as facilitate the alignment of the Schlieren assembly. The iris was situated at the focal point of the first (M1) of a pair of 15 cm, 1 meter focal length mirrors creating a parallel light path which passed through the bunsen flame (B) onto the second 15 cm mirror (M2). The second mirror focused the compound shadowgraph at the point of an angled razor blade (R) which blocked the shadowgraph passing the Schlieren image. The Schlieren image is then recorded by a LaVision Flowmaster camera, the image being cast directly into the camera's (C) objective.
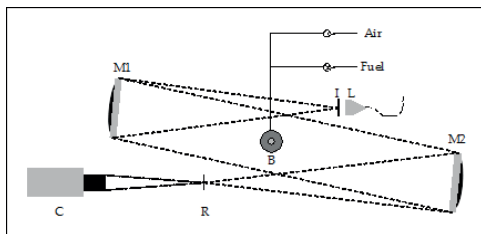

Figure 1 The experimental setup.

Measurements were taken over a range of air-fuel ratios, with the only restrictions being that the flame should be stable and in the laminar flow regime. For each gas blend and air-fuel ratio, two hundred images were recorded. In preheated measurements, the temperature was brought to 270°C, and

measured before and after the measurement set. Any temperature swings greater than 5 degrees were retested. The pressure for all measurements was 1 atm.

DATA PROCESSING

The Schlieren images of the flames were converted to flame speeds a three step data processing procedure: flame edge location, errant data rejection, and flame speed computation.

Initially the data exists as either a monotone png or bmp format picture. The flame is isolated in a roughly rectangular area that extends from the just below the burner tip to slightly above the flame cone. This cropped image is bisected at the vertical axis passing through the point of the flame cone. The coordinates for the flame cropping and bisection are applied to the entire data set for a specific set of test conditions. For each row and half of the flame, the point of maximum intensity is isolated for the cropped image. The X and Y coordinates of these maxima are recorded for subsequent processing. A quasi instantaneous slope of the maxima coordinates is used to graphically locate the region of the flame to be used for the flame speed values. The limits for the fitted region are noted relative to the burner radius. The slope from this linear fit is used to calculate the flame cone angle. To eliminate any spurious results due to camera misorientation, the flame half-angle is defined as the mean of both sides' values for a single flame image (figure 2).
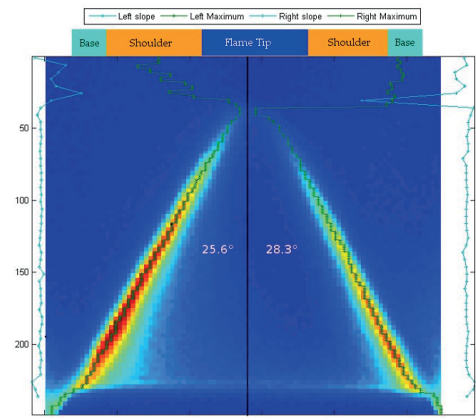

Figure 2 The raw processed Schlieren flame image with half-angles, before angle correction.

Variance in the flame speed calculation is most dependent on fluctuations in the cone angle, due to the trigonometric relation between them. Thus, a rigid criterion for data rejection was needed. It was decided that any flame angle outside one standard deviation from the mean flame angle would be dropped from the data set. This is a rather aggressive level of

elimination, which was necessary for the subsequent analysis steps.

The final step was the actual determination of the flame speed. The cone angles for the refined data set were processed along with their respective gas blend, temperature, burner diameter and bulk flow to generate a set of flame speeds for each picture. The mean and standard deviation of the flame speed were generated for each test set. All physical properties of the gases were calculated in accordance with Geerssen [15].

While traditional half-angle methods approximate flame speed using the shape of the flame and the bulk flow, this paper uses a modified half-angle procedure for flame speed measurement by identifying a region of the flame that is free from the effects of stretch and using the flow velocity at that point for computation of the laminar flame speed. This constrained cone-angle method is compared to the traditional half-angle method, shown in the validation section of the paper.

MODELLING

For purpose of comparison, the laminar flame speeds were modeled using three chemical kinetics models: the GRI 3.0 mechanism, the San Diego mechanism, and an extended Hoyerman mechanism; explanation of the reaction mechanisms can be found in [12-14], respectively. The GRI mechanism has been extensively tested for methane and natural gas combustion. For syngas combustion, when carbon monoxide and hydrogen are major components, the San Diego mechanism is typically in better agreement with experimental data. In this investigation, the San Diego mechanism was used in comparison with the high hydrogen content gases A1 and A2. The Hoyerman mechanism is suited to methane and longer hydrocarbons, and is a more detailed reaction set than either the GRI or San Diego mechanisms.

Laminar flame speed simulations were performed using the commercial software, DARS v2.02 [16]. The kinetic mechanisms were applied to the built-in model of a freely propagating, premixed flame. The modeled flame is assumed to be infinitely large and flat; hence, it is one dimensional and free of strain. The freely propagating flame model was calculated using a variable Lewis number. This also allows differential diffusion to be accounted for.

LAMINAR FLAME SPEED

Laminar flame speed is defined as the velocity at which a premixed flow approaches, perpendicularly, the surface of the flame. For Bunsen burner type flames, multiple methods exist that determine the flame speed; such as, the total area method [6-8], and the cone-angle method [4]. The limitations of each method are discussed in [17] and [18]. The cone-angle method which is employed with modification in this work relates the bulk flow velocity of the premixed gas to the laminar flame speed by:

$$S_L = u_B \sin \alpha$$

Where $u_B = \dot{V}/A_n$ is the bulk velocity (volume flow rate divided by the cross sectional area of the burner) and α is half the flame front angle. Examining Figure 2, the flame cone can be seen, as are two features of the conical flame that are problematic when assessing the flame cone angle. At the tip of the flame cone, the flame front is rounded over; similarly the flame bows outward to meet the burner edge. The distortion at the flame edge is a function of flow stagnation, heat loss and quenching [19], while the tip nonlinearity is caused by stretch and heat diffusion [20].

VELOCITY PROFILE

The simplicity of the cone-angle method relies on the assumption of a top hat profile for the bulk gas flow. However, when velocity profiles were measured 0.4 mm above the burner tip by PIV, they were found not to be top hat shaped. Additionally, the velocity profiles showed dependence on the flow Reynolds number, calculated from the bulk velocity, nozzle diameter, and unburnt fluid properties. PIV measurements of the velocity profile for 10 mm and 4 mm nozzles are shown as line traces in Figures 3 and 4, respectively.[1] The profiles were normalized to 1 radius in the x-direction and in the y-direction the velocity was normalized to give a unity volume flow. Velocity profiles for combustion measurements were generated using a cubic spline interpolation in Matlab[TM] to transform the profile from PIV measurements to the equivalent Reynolds numbers used in combustion experiments ('x' trace, Figures 3 and 4).
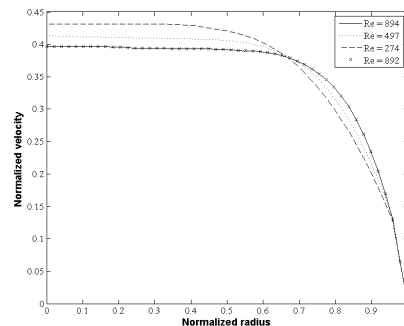
Figure 3 The normalized velocity profiles for the 10 mm nozzle. The marker (x) show the interpolated flow profile for Re = 892, which correspond to the methane measurement at $\emptyset$ = 1.056.

---

[1] The Measurements for gas B1 and B2 at the room temperature lean blow off limit required a 13mm burner tip for stability. In these cases, the Reynolds dependent flow profile from the 10mm burner was assumed.
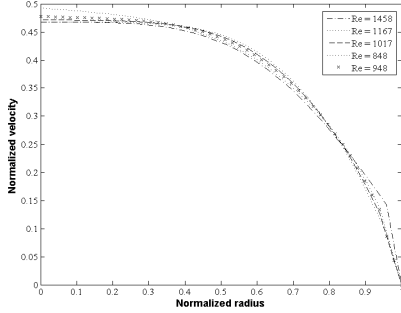
Copyright © 2010 by ASME

Figure 4 The normalized velocity profiles for the 4 mm nozzle The marker (x) shows the interpolated flow profile for Re = 948, which corresponds to the A1 gas measurement at $\emptyset$ = 1.41.

While the half-angle in the shoulder region does not vary with radius, the flow profile does show a radial and Reynolds dependence. By measuring the flow profile, and applying it to the flame cone angle, the laminar flame speed can be redefined as a function of radius and Reynolds number:

$$S_L(r) = u(Re, r) \sin \alpha$$

The combination of the constant α in the shoulder region and the variable flow profile would suggest an increase in the laminar flame speed at smaller radii. However, since laminar flame speed is constant, additional factors must be considered, specifically stretch [21, 22].

FLAME STRETCH
A definition of stretch is that it is the relative local time derivative of the flame surface [22].

$$\kappa = \frac{1}{A}\frac{dA}{dt}$$

The stretch definition for an axisymmetric Bunsen burner has been derived by Law [22]. In the shoulder region, with almost constant α, the stretch may be approximated as:

$$\kappa = -\frac{\sin \alpha}{r}\left[r \cos \alpha \frac{\partial u}{\partial r} + u \frac{\partial(r \cos \alpha)}{\partial r}\right]$$
$$\approx -\frac{\sin \alpha}{r}\left[r \cos \alpha \frac{\partial u}{\partial r} + u \cos \alpha\right]$$

Where both α and u are functions of the radius. The first term in the brackets leads to an increase in stretch ($\partial u/\partial r$<0), whereas the second term decreases stretch. At the center of the burner, stretch is negative, but towards the edge of the burner, the

stretch changes to a positive value. This gives a crossing point with a stretch value of zero, seen at 3.8 mm (Figure5).
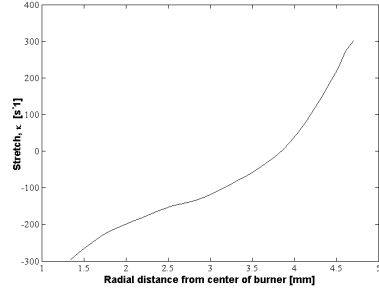

Figure 5 The variation of stretch with radius. Computed from measurement of methane at ϕ=1.056 and T_u=25°C.

Stretch affects the measured value for flame speeds; stretched flame speeds were found to be up to 20% higher than the non-stretch flame speeds. Only at the crossing point is the measured flame speed equal to the unstretched laminar flame speed. This characteristic is exploited by the constrained half-angle method which uses the velocity at the zero stretch radius and α for the linear region of the flame profile to calculate the laminar flame speed.

VALIDATION
To validate the procedures used, methane laminar flame speed values from the constrained half-angle method and traditional half-angle method [4] were compared to previous measurements [23-25] and predictions from the GRI 3.0 mechanism at 25°C (Figure 6). There is good agreement between the model, previous work, and the traditional half-angle method (open squares) performed for this paper. The constrained half-angle method (open triangles) does not show the same agreement. While the trend is in line with previous measured values, the velocities are more than 10% higher than values from the traditional half-angle method. However, as the tradition half-angle method relies on assumptions regarding flow profile that lead to an underestimation of the unburnt gas velocity, the disagreement is to be expected.
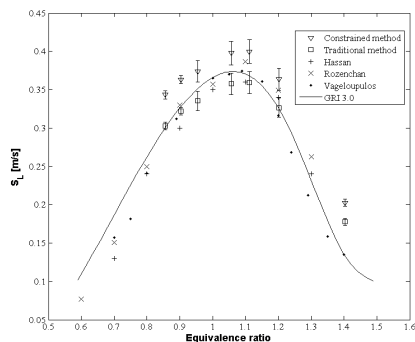
Figure 6 The measured and computed flame speeds for methane at T$_u$=25 °C.

RESULTS

The laminar flame speeds were measured for each of the gases found in table 1. Measurements were made at 25°C and 270°C, at 1 atm, and the reactions modeled using several chemical kinetic mechanisms. For methane and the group B gases, the GRI 3.0 [12] mechanism and the Hoyermann [14] mechanism were used; with group A gases, the GRI 3.0 [12] mechanism and the San Diego [13] mechanism were most appropriate. Flame speed measurements were done using the constrained half-angle method previously described.

Methane

The peak flame speeds for methane increased by a factor of 2.8 at 270°C. The flame cone, at higher temperature, was subject to instability, evident in the error bars shown for those measurements.

Methane flame speeds were compared to predicted values from the GRI 3.0 [12] Mechanism and the Hoyermann [14] mechanism. At 25°C, both mechanisms predict similar flame speeds, while measured flame speeds were higher than predicted. At elevated temperatures, the chemical kinetic mechanisms are no longer in agreement, with the Hoyermann [14] mechanism predicting a higher flame speed than the GRI 3.0 [12] mechanism. At high temperature, the Hoyermann[14] mechanism's curve better predicted measured flames speeds for most equivalence ratios.
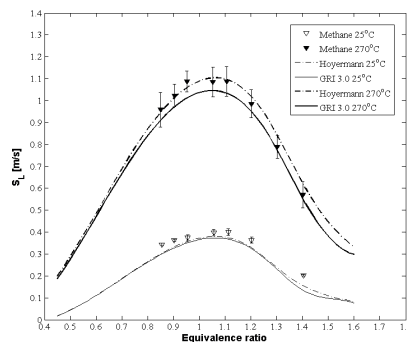

Figure 7 The measured and computed flame speeds for methane at T$_u$=25 °C and T$_u$=270°C.

Group A gases

Measurement on group A gases were performed at 25°C and 270°C. The measurements at 270°C showed flame speeds substantially slower than the predicted values, and were excluded from this paper. It is probable that the gases were pre-reacting in the heating section of the assembly, as the experiments were close to the auto ignition temperature.

Group A gases were compared with predicted values from the GRI 3.0 [12] and San Diego [13] mechanisms. Both mechanisms predict higher flame speeds than measured for either temperature. While the mechanism predicted the same equivalence ratios for maximum flame speed, they were not in agreement as to the actual velocity. The measured maximum flame speeds were found at lower equivalence ratio than predicted with gas A1, while gas A2 showed a higher than expected equivalence ratio at maximum flame speed. It is unclear whether this difference is due to error in measurement or a deficiency in the flame speed calculation from the chemical kinetic mechanisms.
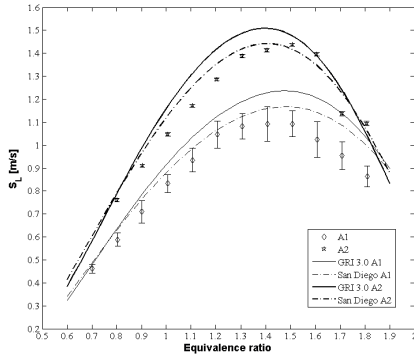
6   Copyright © 2010 by ASME

Figure 8 The measured laminar flame speeds for gases A1 and A2 at T_u=25 °C.

Figure 9 The measured laminar flame speeds for gas B1 at T_u=25 °C and T_u=270°C.

Group B gases

For group B gases, the measured flame speeds at both 25°C and 270°C were higher than the predicted values. Preheating the combustion mixture increased the flame speed by a factor of approximately 2.9 for all group B gases. In comparison to pure methane, there was little change in the equivalence ratio that yielded highest flame speeds. In the case of gases B2 and B3 it is likely that the increase in hydrogen content to 5% and 10%, respectively, was insufficient to cause a drastic change in peak velocity equivalence ratio. The decreased heating value of methane, diluted with CO2, (gas B1) gave a drop in the maximum flame speed at both temperatures measured. Raising the hydrogen content from 0% to 10% gave slight increases in maximum flames speeds; 27.5 cm/s to 30.2 cm/s at 25°C and 81.6 cm/s to 90.7 cm/s at 270°C.

Models of the group B gases, by the GRI 3.0 [12] mechanism and the Hoyermann [14] mechanism, were in good agreement with one another at 25°C. However, just as with the methane reference gas, there was lower correlation between the velocity values at higher temperature.
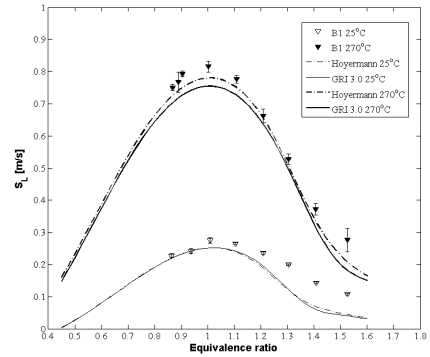

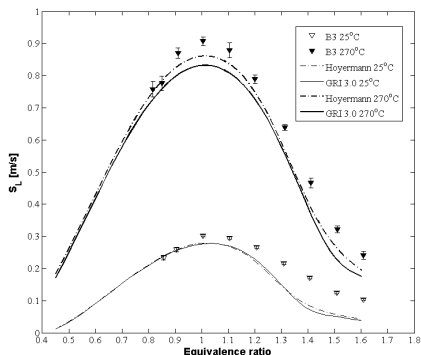**Figure 10 The measured laminar flame speeds for gas B2 at T_u=25 °C and T_u=270°C.**

7

Figure 11 The measured laminar flame speeds for gas B3 at T_u=25 °C and T_u=270°C.

CONCLUSIONS

The laminar flame speeds for several syngases were measured at two temperatures, 25°C and 270°C, using a constrained half-angle method. For each gas, the equivalence ratio was swept from the lean blow off limit of the burner to a mixture on the rich side of the maximum laminar flame speed. Methane was used as reference gas to validate the method. The constrained half-angle method yielded slightly higher flame speeds than reference values which used alternative methods.

Three different mechanisms were used as comparison for the measured flame speeds, namely, the GRI 3.0 [12] mechanism, the Hoyermann [14]   Mechanism and the San Diego [13] Mechanism. The measured laminar flame speeds were consistently higher than the value predicted by the mechanisms, with the exception of gases with high hydrogen and carbon monoxide contents, where they were slightly lower. Additionally, the maximum flame speed for these gases occurred at different equivalence ratio than was predicted by the chemical kinetic mechanism.

While the constrained half-angle method represents an effort to address failings in the traditional half-angle method, it is by no means a perfect approach. Improvements could be made by getting a more highly resolved flame image. Using a more highly resolved image, the flame half-angle could be measured continuously over the flame shoulder, rather than assuming a linear shoulder region. With local values for the half-angle, flame stretch could be calculated as a function of local flame angle, in addition to velocity and radius as currently assessed. This should improve the constricted half-angle model.

ACKNOWLEDGEMENTS

REFERENCES

[1] Moliere, M., 2002, "Benefiting from the Wide Fuel Capability of Gas Turbines: A Review of Application Opportunities," ASME Paper# GT-2002-30017, pp.

[2] Hagen, M., Polman, E., Myken, A., Jensen, J., Jönsson, O., and Dahl, A., 2001, "Adding Gas from Biomass to the Gas Grid," Swedish Gas Centre, Report SGC 118.

[3] De Lorenzo, L., Kreutz, T. G., Chiesa, P., and Williams, R. H., 2008, "Carbon-Free Hydrogen and Electricity from Coal: Options for Syngas Cooling in Systems Using a Hydrogen Separation Membrane Reactor," Journal of Engineering for Gas Turbines and Power, 130(3)

[4] Braun-Unkhoff, M., Kick, T., Frank, P., and Aigner, M., 2007, "An Investigation on Laminar Flame Speed as Part of Needed Combustion Characteristics of Biomass-Based Syngas Fuels," ASME Conference Proceedings, 2007(47918).

[5] Dong, C., Zhou, Q., Zhao, Q., Zhang, Y., Xu, T., and Hui, S., 2009, "Experimental Study on the Laminar Flame Speed of Hydrogen/Carbon Monoxide/Air Mixtures," Fuel, 88(10)

[6] Natarajan, J., Kochar, Y., Lieuwen, T., and Seitzman, J., 2009, "Pressure and Preheat Dependence of Laminar Flame Speeds of H2/CO/CO2/O2/He Mixtures," Proceedings of the Combustion Institute, 32(1).

[7] Natarajan, J., Lieuwen, T., and Seitzman, J., 2007, "Laminar Flame Speeds of H2/CO Mixtures: Effect of CO2 Dilution, Preheat Temperature, and Pressure," Combustion and Flame, 151(1-2).

[8] Natarajan, J., Nandula, S., Lieuwen, T., and Seitzman, J., 2005, "Laminar Flame Speeds of Synthetic Gas Fuel Mixtures," ASME Paper# GT2005-68917

[9] Davis, S. G., Joshi, A. V., Wang, H., and Egolfopoulos, F., 2005, "An Optimized Kinetic Model of H2/CO Combustion," Proceedings of the Combustion Institute, 30(1).

[10] Juan, L., Zhenwei, Z., Andrei, K., Marcos, C., Frederick, L. D., and James, J. S., Jr., 2007, "A Comprehensive Kinetic Mechanism for CO, CH2O, and CH3OH Combustion," International Journal of Chemical Kinetics, 39(3).

[11] Konnov, A. A., 2008, "Remaining Uncertainties in the Kinetic Mechanism of Hydrogen Combustion," Combustion and Flame, 152(4).

[12] Smith, G. P., Golden, D. M., Frenklach, M., Moriarty, N. W., Eiteneer, B., Goldenberg, M., Bowman, C. T., Hanson, R. K., Song, S., Gardiner Jr, W. C., Lissianski, V. V., and Qui, Z., 1999, "Gri-Mech 3.0," http://www.me.berkeley.edu/gri_mech.

[13] 2006, "San Diego Mechaism," http://maeweb.ucsd.edu/~combustion/cermech/.

[14] Hoyermann, K., Mauß, F., and Zeuch, T., 2004, "A Detailed Chemical Reaction Mechanism for the Oxidation of Hydrocarbons and Its Application to the Analysis of Benzene Formation in Fuel-Rich Premixed Laminar Acetylene and Propene Flames," Physical Chemistry Chemical Physics, 6(14),.

[15] Geerssen, T. M., 1988, *Physical Properties of Natural Gases*, NV Nederlandse Gasunie, The Netherlands, Groningen.

[16] Dars – Software for Digital Analysis of Reactive Systems. Diganars, D., USA, (http://www.Diganars.Com), 2009.,

[17] Andrews, G. E., and Bradley, D., 1972, "Determination of Burning Velocities: A Critical Review," Combustion and Flame, 18(1).

[18] Dugger, G. L., Simon, D. M., and Gerstein, M., 1959, "Laminar Flame Propagation," NACA Report 1300.

[19] Lewis, B., and Elbe, G. V., 1987, *Combustion, Flames and Explosions of Gases*, Academic, Orlando.

[20] Choi, C. W., and Puri, I. K., 2001, "Contribution of Curvature to Flame-Stretch Effects on Premixed Flames," Combustion and Flame, 126(3).

[21] Law, C. K., 1989, "Dynamics of Stretched Flames," Symposium (International) on Combustion, 22(1).

[22] Law, C. K., and Sung, C. J., 2000, "Structure, Aerodynamics, and Geometry of Premixed Flamelets," Progress in Energy and Combustion Science, 26(4-6).

[23] Hassan, M. I., Aung, K. T., and Faeth, G. M., 1998, "Measured and Predicted Properties of Laminar Premixed Methane/Air Flames at Various Pressures," Combustion and Flame, 115(4).

[24] Rozenchan, G., Zhu, D. L., Law, C. K., and Tse, S. D., 2002, "Outward Propagation, Burning Velocities, and Chemical Effects of Methane Flames up to 60 Atm," Proceedings of the Combustion Institute, 29(2).

[25] Vagelopoulos, C. M., and Egolfopoulos, F. N., 1998, "Direct Experimental Determination of Laminar Flame Speeds," Symposium (International) on Combustion, 27(1).

Paper V

Trimethylindium as an Indium Source for Combustion Experiments

Ronald Whiddon, Bo Zhou, Jesper Borggren, ZhongShan Li

November 8, 2013

Abstract

Trimethylindium (TMI) is used as an indium transport molecule for the introduction of indium atoms to a combustion environment. A seeding system was constructed to allow addition of an inert TMI laden carrier gas into the air-fuel mixture of a burner. TMI was found to be suitable source of indium, evidenced by the strong indium emission visible in the flame. The seeder was calibrated using the fluorescent emission intensity from the $6^2S_{1/2} \rightarrow 52P_{1/2}$ and $6^2S_{1/2} \rightarrow 5^2P_{3/2}$ transitions as a function of the calculated seeding concentration over a range of 2 to 45 ppm. The response was found to be linear over the range 3 to 22.5 ppm; at concentrations above 25ppm there is a loss of linearity attributable to a combination of self absorbtion, loss of saturation in the carrier gas flow and other factors. TMI derived indium signal was investigated at a variety of flame equivalence ratios by imaging the flame with filters so that the 410nm and 450nm indium transitions were imaged. The indium signal was seen to be evenly distributed in the flame, having a peak intensity at rich equivalence ratios. Laser investigation of the TMI seeded flame measured an actual indium concentration at the ppb level, a transfer efficiency 0.001. In agreement with the transition intensity ratios, there is self absorption seen at the higher concentrations of TMI seeding. Experiments were performed in which TMI was introduced to a post-combustion environment via an inert carrier gas. This resulted in an orange emission region in the carrier gas plume which was found to arise from InH transitions. Other transitions were found from the spectrum of the orange plume which are not yet positively identified.

I Introduction

Indium is an oft considered tracer, together with thallium, lead and gallium, for the determination of temperatures in flame when using the two-line atomic fluorescence[1, 2, 3], as it features a low lying excited state that has a significant population at flame temperatures. The most common approaches to getting indium atoms into the gas phase use indium chloride solution that is either directly aspirated (pneumatic/acoustic) or injected through a capillary into a hot flow. This seeding process is characterized by the creation of small droplets of indium chloride solution that dry to $InCL_3$ crystals which are thermally decomposed to form atomic indium when passing the flame front; thus indium signal can only be obtained from the post combustion region of the flame[4]. Aspirating seeders generate a range of droplet sizes, only some of which successfully join the carrier gas stream, excess must be drained off to diminish problems of clogging and condensation on instrument surfaces. In pneumatic nebulizers, small fluctuations in the driving pressure can result in noticeable changes in the seeding concentration over time. Any flux in a solvent based seeding system shows further effects in the flame by changing the flame chemistry and temperature as solvent concentrations change[5, 6, 7]. Recently, a group has investigated the seeding of indium atoms by laser ablating a metal indium sample in the flow stream, detecting the ground state indium via laser induced fluorescence[8]. In this manner, atomic indium is produced directly and measurements can be made in the preheat region of the flame. While it surmounts the clogging and solvent problems of liquid seeding systems, there are limitations due to the added complexity of a high energy laser system and a limited amount of seeding material that can be produced by such means.

We have experimented with the organometallic compound trimethylindium as seed source for indium in a combusting flow. Trimethylindium (TMI) is an organically linked metal that is used in vapor deposition of semiconductor devices. It reacts rapidly in air and water and decomposes at temperatures above 80 Celsius. In this work we adapt a chemical vapor deposition bubbler to supply TMI as an indium seeding substrate carried by an inert carrier gas into a fluid stream.

II Setup

A Combustion system

The experiments discussed in the following sections are performed on a hybrid McKenna burner featuring a central open jet, figure 1. The water cooled scintillated brass burner surface is 7.6

Figure 1: Photograph of a TMI seeded flame with ϕ=1.0 using the central jet mcKenna burner with laser induced fluorescence of Indium visible.

cm in diameter and created with methane and air via mass flow controllers. The burner was operated at an equivalence ratio of $\phi=0.9$ and served to stabilize the central jet by providing a combustion heated surrounding airflow. The burner's central jet is a 1 cm diameter open tube. The combustion mixture was supplied by blending nitrogen, oxygen and methane well upstream of the burner; individual gas flow was regulated by mass flow controllers. The nitrogen component of the combustion mixture was altered to counter changes in the carrier gas addition which yielded a consistent air blend for all carrier gas flow rates. The carrier gas from the TMI seeding apparatus was added to the central jet combustion mixture 15 cm from the burner surface. It was found that when increasing this distance up to 1 meter there was no discernible change in indium emission intensity for a given set of conditions.

B   Optics systems

Flame images were recorded with a PiMax III camera using a 50 mm objective focused at the flame center. Bandpass filters (CVI F10-410 and CVI F10-450) were used to discriminate between the indium. The peak transmission wavelengths were at 410 nm and another at 450 nm each with a 10 +/- 2nm bandwidth. Flame spectral measurements were collected by a 500 mm 1/f = 2.0 Halle lens was installed at one focal distance from the flame center and the entrance slit of an Acton half meter spectrometer. Where height is not specifically mentioned, spectra correspond to a position 26 mm above the burner surface, which was a region slightly above the visible cone of the central flame. The aforementioned PiMax III camera was used as detector, the system response was corrected using a tungsten calibration lamp.

C   Seeding system

A schematic of the indium seeding system and the burner are shown in figure 2. The system is built around a TMI crystal sublimation chamber and is designed to maintain the inert environment needed by the bulk TMI compound while allowing control of seeding concentration. The TMI container is supplied from SAFC, the function is described by Gerrard 8; for this application the bubbler is operated in the standard flow configuration. A mass flow controller located upstream of the bubbler regulates flow of instrument grade nitrogen through the seeding system. The tubing forward of the flow controller is 6mm stainless steel, all fittings and junctions are Swagelok couplings. The valves were metal seat, sealed bellows type, their arrangement enables

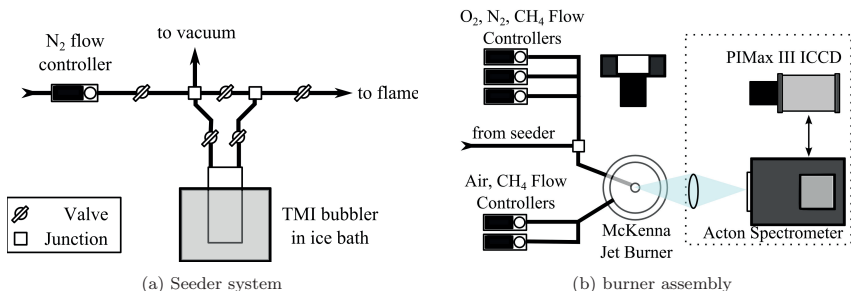(a) Seeder system   (b) burner assembly

Figure 2: Burner assembly with attached indium seeding apparatus. Imaging systems are changeable between a Princeton Instruments ICCD camera and Acton $\frac{1}{2}$ meter spectrometer.
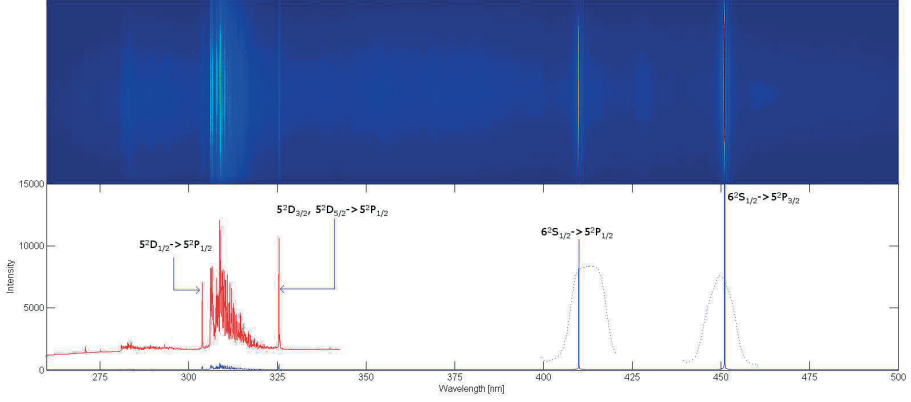
Figure 3: Flame spectrum from 26mm above the flame surface for 10 ppm TMI seeding. Indium lines are noted in the image. Overlayed with the spectrum is a 20x magnification of region from 260-340nm and the transmission curves for two Schott filters used in further experiments

the TMI bubbler to be isolated from the system without disruption of the flow. With the TMI bubbler isolated, the seeding system can be flushed with nitrogen, and evacuated- in order to clear contaminants from the system, e.g. water, oxygen or residual TMI. A backflow prevention valve was used between the seeding system and the burner to prevent the oxidizing environment of the air/fuel mixture from contaminating the seeder in the event of an pressure imbalance between the air/fuel flow and the seeding system. The nitrogen carrier gas, seeded with TMI is introduced to the burner fuel/air flow 15cm before the burner surface. The concentation of TMI at the burner was adjusted by changing the flow through the TMI bubbler, as this afforded the widest range of seeding concentrations. The concentration of TMI in the burner flow is calculated from the relative vapor pressure of TMI in the carrier gas stream (equation 1)9, as diluted by the fuel, nitrogen and oxygen mixture of the central burner jet (equation 2).

$$Log(P) = 10.98 - (3204/T)...[Torr] \tag{1}$$

$$C_{TMI} = [(P_{TMI}V_{carrier}/760)/(V_{carrier} + V_{N_2} + V_{O_2} + V_{CH_4}) \tag{2}$$

III Applications

A Indium in a Oxidizing Carrier Flow

A two dimensional emission spectrum from the TMI seeded ϕ=1.0 central jet is show in figure 3. The spectrum was taken at a height of 26 mm above the burner surface. The spectrometer slit width was 100 μm, and a 1200/mm grating with 300 nm blaze angle was used. The wide range spectrum is created by collecting several spectra over the entire range. For each sub-spectrum 100 accumulations were made with and integration time of 100 ms. The two dimensional spectrum is averaged to create a spectral line plot seen in the lower half of figure 3. Several characteristic lines have been identified using the NIST spectral databas for indium [9]. Featuring most prominently in the spectrum are the two atomic Indium lines from the $6^2S_{1/2} \to 5^2P_{1/2}$ and $6^2S_{1/2} \to 5^2P_{3/2}$ transitions at 410 and 451 nm, respectively. Using a 20x magnification of the 260-340 nm region
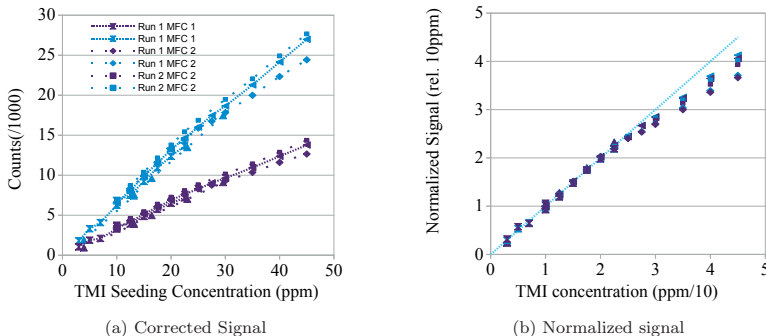
5

Figure 4: Calibration of seeding system, linearity of response. Purple values are from 410 nm emission and blue from 451 nm emission. Left image is data collected from several measurements, right image is data corrected against the 10 ppm signal level.

of the spectrum, a few more indium transitions are visible: 304 nm ($5^2D_{1/2} \rightarrow 5^2P_{1/2}$) and the doublet at 325 nm ($5^2D_{3/2}, 5^2D_{5/2} \rightarrow 5^2P_{1/2}$). The presence of these lines makes it obvious that indium in its atomic form is indeed present in the flame, thus the TMI is functional as a seed source for flame measurements.

To calibrate the response of the seeding system, the emission intensity of the $6^2S_{1/2} \rightarrow 5^2P_{1/2}$ and $6^2S_{1/2} \rightarrow 5^2P_{3/2}$ transitions were measured while changing the TMI seeding concentration from 2.5 to 45 ppm. Trimethylindium was added to the fuel/air mixture fed to the central jet which was operated with an equivalence ratio of ϕ=1.0. The surrounding McKenna flame featured an equivalence ratio of ϕ=0.9. Addition of nitrogen in the TMI seeding flow was compensated for by reducing the nitrogen component of the fuel/air mixture. The signal intensity as a function of calculated TMI concentration in the combustion mixture is shown in figure 4 left. There is a linear response in the range from 10 25 ppm TMI, though this is somewhat occluded by the variability in the signal for various runs. The variabilty in the signal was can be attributed to the disassembly and reconstruction of the TMI seeding system, burner and optics components between measurement days. It is possible to remove the effects of the mechanical changes to system by considering the simplified equation for atomic emission: $I_{ji} = n_j A_{ji} V \Omega$. Normalizing the emission intensity at any TMI concentration, I_{ji}, by the emission intensity at 10 ppm for the same run eliminates the system collection efficiency (Ω), probe volume (V), and transition coefficient (A_{ji}) specific to that run. This leaves only the relationship between the relative emission and the population, $I_\chi/I_{10} = n_\chi/n_{10}$. Figure 4 right is a corrected signal response wherein each run is shown relative to the 10 ppm signal for that discrete run. It becomes clear that the seeding system is linear below 22 ppm TMI, and there is unity increase in signal with increase in TMI concentration.

The linearity of the seeding systems is seen to extend only up to approximately 22.5 ppm TMI. After this value the emission intensity is seen to fall away from linearity, the effect is greater for the 450nm transition than for the 410nm transition. As the two transitions arise from the same upper energy level, the intensity is predicted by the probability of each transition. The ratio of the intensity of the 410nm emission to the 451nm shoul be a flat line at 0.56 [10], slightly off from the measured ratio in figure 5 of 0.52. Also in this figure it is seen that the ratio falls off at higher concentrations of TMI. This would suggest self absorption as all physical causes of fluctuation in the signal would affect both transitions equally.
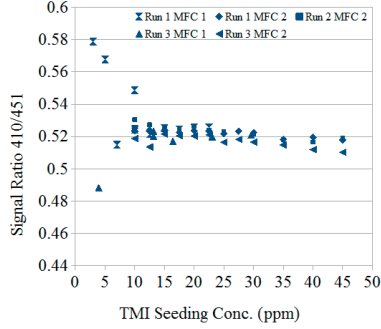
Figure 5: Ratio of signal intensities from the 410 / 451 nm indium transition as a function of TMI concentration.

Pictures of indium emission from the 410 and 450 nm transitions are shown in figure 6 left and middle, respectively. The images shown were for TMI seeded at 10ppm to a central jet with equivalence ratio, ϕ =1.0 and a ϕ=0.9 surrounding McKenna flame. Selection of the specific transition was done by fitting the appropriate Schott color filter before the camera objective. The resultant images are the mean of 300 discrete exposures with 200 us integration time per exposure. Intensity plots are for central jet equivalence ratios of ϕ = 0.8, 1.0 and 1.2 at 10, 20 and 26mm above the burner surface are shown in figure 6 right. Indium signal is evenly distributed away the combustion region with signal decreasing radially as the indium diffuses away from the flame front.
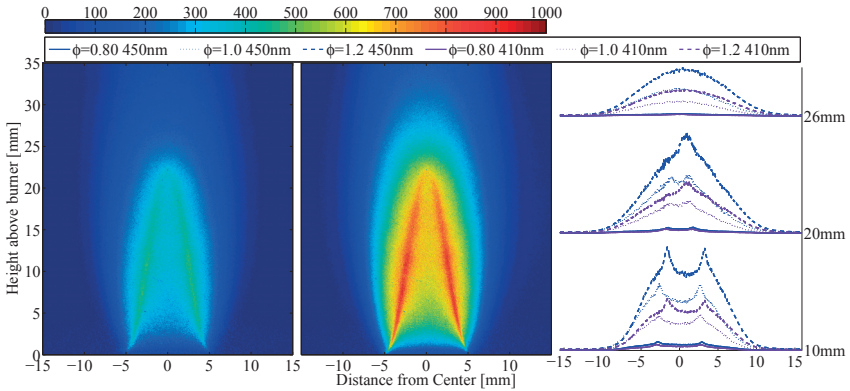

Figure 6: ICCD intensity map of indium transitions at 410nm (left) and 450nm (middle) acquired using filters. At right is the horizontal intensity maps at 10, 20 and 26 mm above the burner surface.
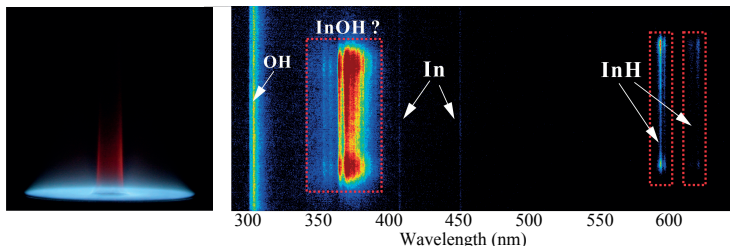
Figure 7: Emission from inert central jet with 234 ppm TMI seeding, surrounding McKenna flame operated at equivalence ratio of 1.4 shown in figure left. At right is the wide range spectrum of the orange luminescence

B   Indium in Nitrogen Carrier

During the TMI seeder shutdown procedure the oxygen and methane components of the carrier stream are stopped and the system flushed with nitrogen to remove residual TMI from the central jet gas lines. It was noticed that a faint orange luminescence was present in the central jet. An image of this luminescence together with the low resolution spectrum of the flame are shown in figure 7.

System Settings

The jet burner was operated with only nitrogen and TMI, flow rates for the jet were similar to the combustion experiments. The luminescence was faintly visible with 10 ppm TMI concentration however increasing the concentration yielded a stronger intensity. The surrounding McKenna flame was operated at and equivalence ratio of 1.4, the emission was not observed when the flame was operated at leaner values. Even a small amount of oxygen in the coflow was found to inhibit the luminescence.

Spectral Features

The congested cluster of bands that appear near 360 nm are believed to be caused by transtions of the molecule InOH [11]. High resolution spectra of the two band groups near 600 nm are shown in figure 8. These emission bands have well resolved structure arising from InH transitions, this was confirmed by simulating the recorded spectra using PGOPHER software [12]. For simulation, a temperature of 580K and a pure Lorentzian profile with 0.11 nm in linewidth were adopted.

InH emission spectrum was observed from a King furnace as reported first by Grundstrom, 1938 [13], followed by extensive studies of the InH spectrum [14, 15, 16]. To the best of the authors knowledge, the present work reports the first observation of the InH emission spectrum in combustion environment. While further investigation of various indium compounds in the inert jet is ongoing, this is an exciting development as combustion synthesis is currently the most widely used means of nanomaterials production[17].
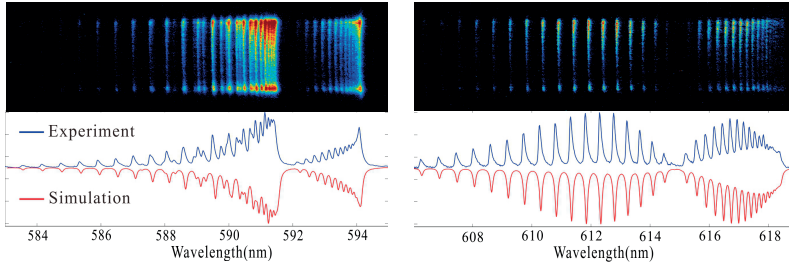
Figure 8: High resolution spectra of InH transitions and corresponding predicted spectra from PGOPHER software.

C Indium Laser Induced Fluorescence

Atomic transitions have a high absorption cross-section compared to molecules and even the low effect diode laser induces a strong fluorescence signal, as can be seen in figure 1 showing a picture of the flame taken with a compact system camera.

A tunable external cavity diode laser, Toptica model DL-100 Pro, centered at 410.2 nm was used to conduct laser based measurements of the TMI seeded flame. The laser power was approximately 10 mW with a specified line width of less than 1 MHz. The collimated laser beam was aligned over the center of the jet burner at a height of x cm. An intensified CCD camera recording the induced fluorescence was placed perpendicular to the beam path and a photodiode located after the flame recorded the laser absorption. Part of the laser light was recorded on an external reference photodiode and a confocal Fabry-Perot ethalon.

Measurement Procedure

According to Beer-Lamberts law the transmitted intensity, I, through an absorbing media is related as

$$I = I_0 e^{\sigma l N} \tag{3}$$

where I_0 is the incident power, σ the absorption cross-section, l the absorption path length and N the number density of the absorbing species. The laser is scanned over a hyperfine transition of indium and the laser power is measured before and after the flame. This serves the same purpose as locking the laser to the peak transition without experimental complications introduced from a PID locking system. The absorption path length is known from the camera image of the indium distribution and the absorption cross-section for the $6^2 S_{1/2} \rightarrow 5^2 P_{1/2}$ transition is calculated from the Einstein A coefficient:

$$\sigma(\nu) = \frac{A\lambda^2 g(\nu - \nu_0)}{8\pi} \frac{2J+1}{2J'+1} \tag{4}$$

Here λ is the wavelength of the transition, g the normalized line shape function and the J ratio is the degeneracy of each state. Both hyperfine peaks $6^2 S_{1/2}, F = 4 \rightarrow 5^2 P_{1/2}, F = 5$ and peak $6^2 S_{1/2}$ F=5$\rightarrow 5^2 P_{1/2}$ F=4 could have been used to conduct the LIF measurements as the transitions are equally strong. Out of convenience the laser was locked to $F = 5 \rightarrow F = 4$ due to the increased laser power at this wavelength and stronger LIF signal. The filter centered at 450 nm was used in front of the ICCD camera to detect the non-resonant fluorescence and rid the images of background flame emission. A stoichiometric TMI seeded jet flame surrounded with a lean co-flow flame of ϕ=0.9 was used to study the concentration and distribution of indium.
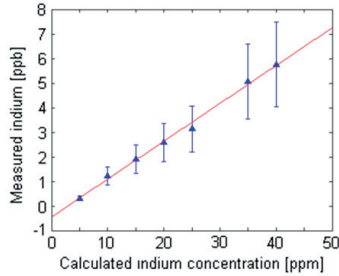
9

Figure 9: Indium concentration as measured by laser absorbtion versus the calculated concentration of TMI. Negative Y intercept indicates that there is a loss of Indium to the walls.

Indium Concentration

The measured indium concentration plotted against the calculated concentration from equation 2 is shown in figure 9. A linear dependence between the seeding concentration and measured concentration is seen. It is evident that the concentration of indium atoms in the flame is drastically lower than the predicted amount of TMI leaving the bubbler, suggesting that TMI is removed from the gas stream. Observation of deposits in the gas lines reinforces the conclusion that TMI is deposited before reaching the flame. The greatest errors in the measured concentrations originate from uncertainties in the line shape simulation, mainly uncertainties in the average temperature along the absorption path length and the laser line width.

Indium Distribution

The upper portion of figure 10 shows the laser induced fluorescence signal in the flame seeded with 5 ppm averaged over 150 images. Assuming the absorption is negligible the intensity of LIF signal is proportional to the indium concentration distribution in the flame. The distribution of the LIF signal bounded by dashed red lines is shown in the lower portion of figure 10 along with the response for several different seeding concentrations . The concentration of indium is highest directly after the reaction zone, exponentially decaying away from the jet flame front indicative of indium distribution governed by diffusion. For higher concentrations absorption of the laser beam is observed. The disparity in LIF intensity between the left and right peaks is explained by the LIF signal being proportional to the laser intensity times the indium concentration. As the concentration increases to the center of the burner the laser is absorbed resulting in the shape of the curve.
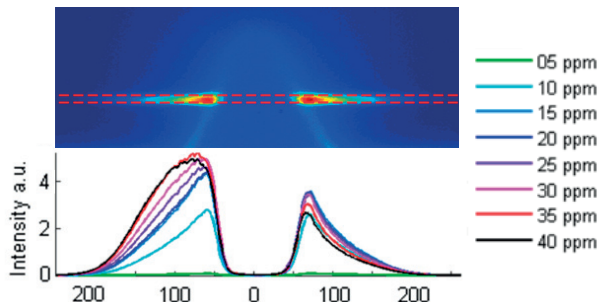
Figure 10: Laser absorbance imaged across a methane air jet flame with 5 ppm TMI seeding. Red dashed lines show integrated beam height. Lower chart is LIF signal as a function of TMI seeding concentration, which is a function of absorbance across the flame.

Conclusion

This work was performed to assess the possibility of seeding indium into a combustion environment without resorting to a liquid phase injection method. In that respect there was marked success, indium signal was present and uniformly distributed in the flame. Deviation from linearity in the indium emission signal as a function of the seeding concentration indicates a differential absorbtion of the two prominent indium lines, something that was noticed also in diode laser experiments. There is a non-negligible loss of indium due to deposition of TMI residues in the lines leading to the burner, with only about 1/1000th of the TMI successfully converted to atomic indium at the flame region as measured by laser absorbance.

By carrying TMI in a non oxidizing environment to a rich combustion environment it was discovered that the TMI partially decomposed to InH and at least one other indium compound indicated by the presence of a orange luminescence. This may present the possibility of online spectroscopic monitoring of TMI concentrations in vapor deposition applications. This could also be of interest to the semiconductor community particularly in the area of flame fabrication of nanomaterials.

The successful application of this indium seeding method drives further interest in two line atomic fluorescence temperature determination in the flame. This is a tried method that is still being actively developed both on the systems side and the application side. We are additionally looking at the feasibility of using other high vapor pressure compounds seeded in a similar manner to thermally map the lower temperature regions of the flame, especially the pre-heat zone of the flame.

References

[1] Haraguchi, H., Smith, B., Weeks, S., Johnson, D. J., and Winefordner, J. D., 1977. "Measurement of Small Volume Flame Temperatures by the Two-line Atomic Fluorescence Method". *Applied Spectroscopy,* **31**(2), Mar., pp. 156–163.

[2] Aldén, M., Grafström, P., Lundberg, H., and Svanberg, S., 1983. "Spatially resolved temperature measurements in a flame using laser-excited two-line atomic fluorescence and diode-array detection". *Optics Letters,* **8**(5), pp. 241–243.

[3] Omenetto, N., Benetti, P., and Rossi, G., 1972. "Flame Temperature measurements by means of atomic fluorescence spectrometry". *Spectrochimica Acta,* ***27B***, pp. 453–461.

[4] Nygren, J., Engström, J., Walewski, J., Kaminski, C. F., and Aldén, M., 2001. "Applications and evaluation of two-line atomic LIF thermometry in sooting combustion environments". *Measurement Science and Technology,* ***12***(8), Aug., pp. 1294–1303.

[5] Gibson, J. H., Grossman, W. E. L., and Cooke, W. D., 1963. "Excitation Processes in Flame Spectrometry.". *Analytical Chemistry,* ***35***(3), Mar., pp. 266–277.

[6] Winefordner, J. D., and Latz, H. W., 1961. "Quantitative Study of Factors Influencing Sample Flow Rate in Flame Photometry". *Analytical Chemistry,* ***33***(12), Nov., pp. 1727–1732.

[7] Chan, Q. N., Medwell, P. R., Kalt, P. A. M., Alwahabi, Z. T., Dally, B. B., and Nathan, G. J., 2010. "Solvent effects on two-line atomic fluorescence of indium.". *Applied optics,* ***49***(8), Mar., pp. 1257–66.

[8] Chan, Q. N., Medwell, P. R., Mahmoud, S., Dally, B. B., Alwahabi, Z. T., and Nathan, G. J., 2011. "New Seeding Methodology for Concentration Measurement". In Sixth Australian Conference on Laser Diagnostics in Fluid Mechanics and Combustion, pp. 1–4.

[9] Johansson, I., and Litzen, U., 1967. "The term systems of the neutral gallium and indium atorns derived from new measurements in the infrared region". *Arkiv Fysikum,* ***34***, p. 573.

[10] Hult, J., Burns, I., and Kaminski, C., 2005. "Two-line atomic fluorescence flame thermometry using diode lasers". *Proceedings of the Combustion Institute,* ***30***(1), Jan., pp. 1535–1543.

[11] Lakin, N. M., Brown, J. M., Beattie, I. R., and Jones, P. J., 1994. "The identification of InOH in the gas phase and determination of its geometric structure". *The Journal of Chemical Physics,* ***100***(11), p. 8546.

[12] Western, C. M., PGOPHER, a Program for Simulating Rotational Structure. *http://pgopher.chm.bris.ac.uk.* University of Bristol.

[13] Grundstrom, B., 1938. "Band Spectrum of Indium Hydride". *Nature,* ***141***(3569), Mar., pp. 555–555.

[14] Ginter, M. L., 1963. "The band spectrum of the InH molecule: Characterization of the a3Π state". *Journal of Molecular Spectroscopy,* ***11***(1-6), Jan., pp. 301–320.

[15] Freed, K. F., 1966. "On the Hyperfine Structure of InH and the Theory of the Hyperfine Structure of Molecules in Hund's Case (C)". *The Journal of Chemical Physics,* ***45***(5), p. 1714.

[16] Veseth, L., 1976. "The hyperfine structure of diatomic molecules: Hund's case (cα)". *Journal of Molecular Spectroscopy,* ***59***(1), Jan., pp. 51–62.

[17] Kammler, H. K., Mädler, L., and Pratsinis, S. E., 2001. "Flame Synthesis of Nanoparticles". *Chemical Engineering & Technology,* ***46***, pp. 583–596.

Paper VI

DRAFT: LASER-BASED INVESTIGATION OF GAS TURBINE PILOT BURNER COMBUSTION WITH VARIATION OF EQUIVALENCE RATIO, RESIDENCE TIME AND COOLING FLOW TEMPERATURE.

Ronald Whiddon [*]
Arman Ahamed Subash
Robert Collin
Marcus Alden
Department of Combustion Physics
Lund University
Sweden

Atanu Kundu
Jens Klingmann
Department of Energy Sciences
Lund University
Sweden

ABSTRACT

A 75 milliliter, partially enclosed burner, which serves to ignite and stabilize the main combustion sector of a gas turbine burner was investigated at atmospheric pressure to observe the effect of equivalence ratio, residence time and cooling flow temperature on combustion in and after the burner. Thermocouples placed on the outer skin of the burner were used to discern location of the flame inside the burner volume. Combustion that extends past the exit of the burner was visualized with planar laser excitation of fluorescence from formaldehyde and the OH radical. Additionally, high speed imaging of the flame chemiluminescence was recorded. Combustion emissions were registered with an exhaust gas analyzer, detecting NOx, CO, and unburned hydrocarbons in the exhaust. Initially changes in the burner combustion were induced by varying the equivalence ratio from $\phi = 0.8$ to 1.8. Residence time in the burner was altered by changing the mass flow rate through the burner at these equivalence ratios, and finally the burner wall cooling was set at from 300 and 600 Kelvin.

INTRODUCTION

The gas turbine engine is a versatile means of converting chemical energy to electricity or motive power, being used in transportation, pumping and in power production. In the subset of power production, gas turbines can be employed as base load production facilities, and with the increasing use of renewable source energy production the gas turbine role has expanded to stabilizing power fluctuations of temporally variable sources, distributed grid production and clean combustion of biomass fuels [1–3].

The gas turbine can be considered as a continuous process converter for producing hot gases from fuel. The individual segments of the conversion process, e.g., compression, combustion, expansion can be designed specifically for their given purpose. This has led to high efficiency in combustion with almost 100% oxidation of fuel [4]. Though clean in terms of unburnt fuel, the high combustion temperatures can yield high levels of nitrogen oxides (NOx), regulation of which is continually tightened [5]. This has led to implementation of cooler combusting lean-premixed burners as a means of reducing these emissions. As a consequence of the lower temperature, the thermal NOx creation pathway is inhibited [6–8]. There is a trade-off in running in the premixed, low equivalence ratio regime, namely that combustion can be less stable than at higher equivalence ratios. Combuster and burner design must be tailored to ensure safe and stable operation while maintaining useful operational range.

Lean premixed combustion can be stabilized by inclusion of a pilot burner with the main combuster [9, 10]. This facilitates initial ignition of the whole burner, and can act as a constant, stable re-ignition point for the flame body while running. However, the higher temperatures from this richer combustion region have been found to be the major portion of total NOx emission in some Dry Low NOx burners [10].

In this work a pilot burner is examined in detail to support a

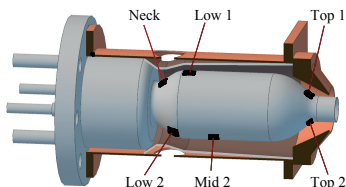[*]Please address all correspondence ronald.whiddon@forbrf.lth.se

FIGURE 1: Burner shown in sectioned mounting adapter for atmospheric measurements. Location of thermocouples along the outer skin are shown, named in coordination with later reference.

discussion of how the burner functions under the different operating parameters.

EXPERIMENTAL SYSTEMS AND METHODS
Burner Assembly

The object of measurement in this paper was the ignition/pilot section of a dry, low emissions burner designed for use in the Siemens SGT-750 gas turbine. The complete burner assembly is composed of concentrically arranged structures: an outer main sector, an intermediate sector and the central pilot/igniter. The pilot/ignitor (henceforth "burner") has been removed from the larger assembly and mounted in an atmospheric pressure test rig to discretely study various attributes of its combustion.

The atmospheric rig supported control and operation as well as providing a means of monitoring operating parameters. There is a bulk air blower that provided the cooling coflow to the burner. It was monitored with a mass flow controller, and could be controlled by adjusting the blower motor speed. The airflow passes through Leister inline heater which was used in half of the experiments to heat the bulk airflow to 600 K. After the heater element, airflow passes over a sequence of meshes to break up large flow structures that may be induced by bends in the supply ducting. All of the bulk airflow passes over the outer skin of the burner and exits about 1 cm before the burner exit. At that point the bulk air can mix freely with gases exiting the burner. A combustion liner with a 110 cm^2 cross section and 1 meter length sits atop the burner/coflow assembly. The first 40 cm of this combustion liner are made in quartz to allow optical access to the post burner region. At the end of the combustion liner there is a contraction and from this region the burner exhaust is sampled.

The fuel and air supplied to the burner are both controlled by using mass flow controllers. Only methane was used in this work as this was the fuel that showed the most variability in character when conducting elevated pressure experiments [11]. Methane was supplied from gas bottles while air was supplied from a large

compressor after being dried and filtered.

Diagnostics

A variety of diagnostic methods were applied to the burner. The burner has 6 thermocouples mounted on the outer surface at various positions indicated in figure 1. These thermocouples were monitored during measurements and are used to intuit the extent of flame distribution in the burner volume. Combustion emissions were sampled 1 meter downstream of the burner exit, where it had been diluted with cooling air. The emissions measured were unburned hydrocarbons, NOx, CO, CO_2 and O_2.

Images were recorded of the flame by three methods: Laser induced fluorescence(LIF) of the hydroxyl radical, LIF of formaldehyde and high speed flame luminescence imaging. The OH-LIF imaging was accomplished by exciting the Q1(8) transition using a frequency doubled, Nd:YAG pumped, rhodamine 590 dye laser, a wavelength near 283.5 nm. The beam was formed into a sheet several centimeters high which was passed through the mid-line of the burner exit. A Phantom high speed camera fitted with a Hamamatsu image intensifier was used to record the OH emission, running at 10 frames per second with an intensifier exposure time of 100 ns. A 105mm quartz objective focused light into the camera, with a Schott WG305 long-pass filter attached to restrict laser scatter interference with the image. Laser induced fluorescence measurements of formaldehyde were taken by exciting the formaldehyde molecule with the frequency tripled emission of a Nd:YAG laser at 355 nm. The beam was formed into a sheet and overlapped with the measurement area of the OH-LIF laser sheet. Formaldehyde emission was collected with a 50 mm glass objective and a Princeton Instruments PI-MAX III camera. A 355nm laser line filter was used to block the excitation wavelength. The formaldehyde images were taken at 10 Hz with an exposure time of 100 ns and were simultaneous
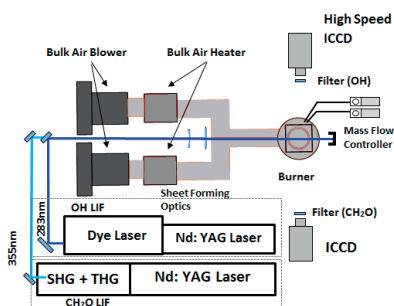

FIGURE 2: Measurement arrangement used in laboratory.

TABLE 1: System parameters used during testing.

Residence Time	Equivalence Ratio	Throat Velocity	Coflow Velocity	Burner Preheat	Coflow Preheat
ms	ϕ	m/s	m/s	K	K
55	0.8-1.5	17.4	20.4	650	300, 600
45	0.8-1.5	21.2	25.0	650	300, 600
35	0.8-1.5	27.3	32.1	650	300, 600
27.5	0.8-1.5	34.7	40.8	650	300, 600

with the OH LIF images. A schematic of the measurement setup is seen in figure (2).

The total flame emission was collected using the previously mentioned phantom camera; however, in this instance, the camera was operated at 3000 frames/second with $100\mu s$ exposure per frame.

Experimental Parameters

A series of experiments were undertaken to investigate variation in combustion characteristics while changing the equivalence ratio, burner residence time and wall cooling. A detailed array of experimental settings are found in table 1. The burner was operated at equivalence ratios from ϕ=0.8 to 1.8 in 0.1 increments, though presented results are limited to save space. The flow rates of the air and fuel in the burner were changed to create non-reacting residence times of 27.5, 35, 45 and 55 ms. Finally, each combination of equivalence ratio and residence time was tested with the coflow temperature at 300 K and 600 K. It was decided that the flow rate between the coflow and non-reacting burner exit velocity should be held at a constant ratio. This required changing the bulk airflow rate with changing experimental parameters.

Upon changing the experimental variables, measurements were taken after the emissions levels and thermocouple values had stabilized. After this, for each test 1000 OH-LIF and CH_2O-LIF images were collected simultaneously with combustion emissions and temperature values. After these values were collected, high speed images of the flame luminescence were recorded.

RESULTS

Global exhaust emission levels of CO and NOx are shown in figure 3. NOx values have been corrected for moisture content and normalized to 15% oxygen. No corrections were made to the CO measurements.

Temperature profiles recorded are shown in figure 4 All equivalence ratios are included. Positions are named in convention with figure 1

Single shot OH-LIF signal and average OH-LIF signal for the series of measurements with coflow at 300 Kelvin are shown

in figure 5. Single shot and average OH-LIF signal for measurements with 600 Kelvin coflow are shown in figure 6.

Formaldehyde LIF image sets were not included with the results as there was insufficient information in the images to warrant inclusion.

DISCUSSION

Before evaluating the data it is useful to consider the flow paths outside and inside of the burner. The most important point is that the coflow mass flow rate was not held constant, thus burner heat loss is not constant for all experiments. This was done in order to minimize the effect of burner-coflow velocity differences on the post burner OH-LIF distribution. Changes in equivalence ratio for a single residence time and coflow temperature did not feature a change in the coflow mass flow rate. Decreasing the residence time in the burner included a higher mass flow in the coflow. Increasing the temperature of the coflow required reducing the mass flow of the coflow due to thermal expansion. Being on the outer skin of the burner, the thermocouples are influenced by the temperature of the coflow.

Inside the burner, preheated air is blended with room temperature fuel at the base of the burner. The swirling mixture expands along the inner surface of the burner where it slows and a portion falls back into the center of the burner creating the central recirculation zone [12]. The burner flame stabilizes according to the balance between the flow speed and flame speed as effected by heat loss to the walls.

Emission Measurements

The CO concentrations showed some variation with changing residence time in the burner, the general trend being that shorter residence times give greater concentrations than longer. This is logical as the burner protects the flame from quenching by the coflow. Also, increasing the coflow flow rate results in greater cooling of the burner which will quench combustion near the walls. If we were to include the effect of dilution by the increase in coflow flow rate with decreasing residence time, the effect would be even less.
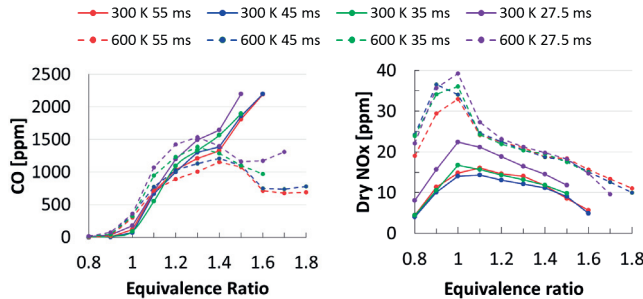
3

FIGURE 3: Emission collected at various operating conditions. CO shown to the left, NOx emissions at right. NOx values have been corrected for water content and normalized to 15% oxygen.

Coflow temperature did not seem to have a large effect on the CO concentration other than at high equivalence ratios where the heated coflow allowed for more complete combustion of products that were not consumed in the burner. As the dilution factor for the heated coflow case is almost half for that of the cool coflow case, actual CO levels between the two are not directly comparable. Also, combustion occurs both in and out of the burner especially for the heated coflow condition. This makes it problematic to calculate back to a "real" CO concentration.

CO levels as a function of equivalence ratio can be sectioned into several similar regions. The first region is from ϕ = 0.8-1.0 where, as expected, the CO level is very low. At these equivalence ratios combustion takes place largely within the body of the burner. The CO levels between ϕ = 1.1 and 1.3 show a sharp increase in the CO concentration which then plateaus. It is likely that this has to do with the combustibility of burner effluent, meaning at the richer equivalence ratios there is partially improved residual combustion. Above ϕ=1.4 the CO concentration deviates; the cool coflow cases continue to increase in CO concentration, while the heated coflow case show a drop in CO as combustion of the fuel rich burner exhaust is more efficient.

NOx levels in exhaust are mostly produced by high temperature combustion regions which occur at near stoichiometric combustion ratios. Thus, the NOx level is highest when the burner is operated near stoichiometry, as seen in figure 3, right. At lean equivalence ratios, the NOx level rises in accordance with the expected flame temperature. A rapid fall off is not seen at rich equivalence ratios, as the fuel that isn't burnt inside the burner body is at least partially burned outside the burner under more diffusion like conditions. There is very little apparent influence of residence time on the NOx level with the exception of the 27.5 ms, cool coflow experiments. Higher coflow temperatures show an increase in the NOx concentration which is as expected.

Temperature Distribution

The two rows of charts in figure 4 show the average temperature at measurement points along the burner body for the various measurement conditions. The temperatures at the Neck, Low 1, Low 2, and Mid 2 thermocouples follow the expected flame temperature for the equivalence ratio, with ϕ = 1.1 having the highest temperature in most circumstances. This temperature trend with equivalence ratio is consistent for all residence times and both coflow temperatures. Top 1 and Top 2 behave in a similar fashion with the exception of the cool coflow condition, where residence times of 55 and 45 ms have higher temperatures for equivalence ratios ϕ = 1.2, 1.3 and 1.4 than for ϕ=1.1. It is possible that for these settings, air is being recirculated back into burner, allowing residual gases to combust there leading to the elevated temperatures seen at Top 1 and Top 2.

Examining the cool coflow temperature traces at different residence times, what is most clear is the effect of cooling from the coflow. As the coflow increases the Neck, Low 1 and Low 2 temperatures decrease steadily. There are also changes to the flame distribution in the burner as well, where equivalence ratios with lower flame speeds exhibit less penetration towards the burner wall. Again, it is the Top thermocouples that show a contrary nature, as these temperatures increase somewhat when the residence times get shorter. Many of the quenching effects that are seen with the cool coflow are not found with the heated coflow. While the neck thermocouple does decrease in temperature by almost 100 degrees in the most extreme case, there is no appreciable change seen in the other thermocouples among the different residence times.

An interesting inversion is apparent between the Low 1 and Low 2 positions at all of the combinations of residence time and coflow temperature. At lean equivalence ratios there is an increase in temperature between the Low 2 and Low 1, but as the
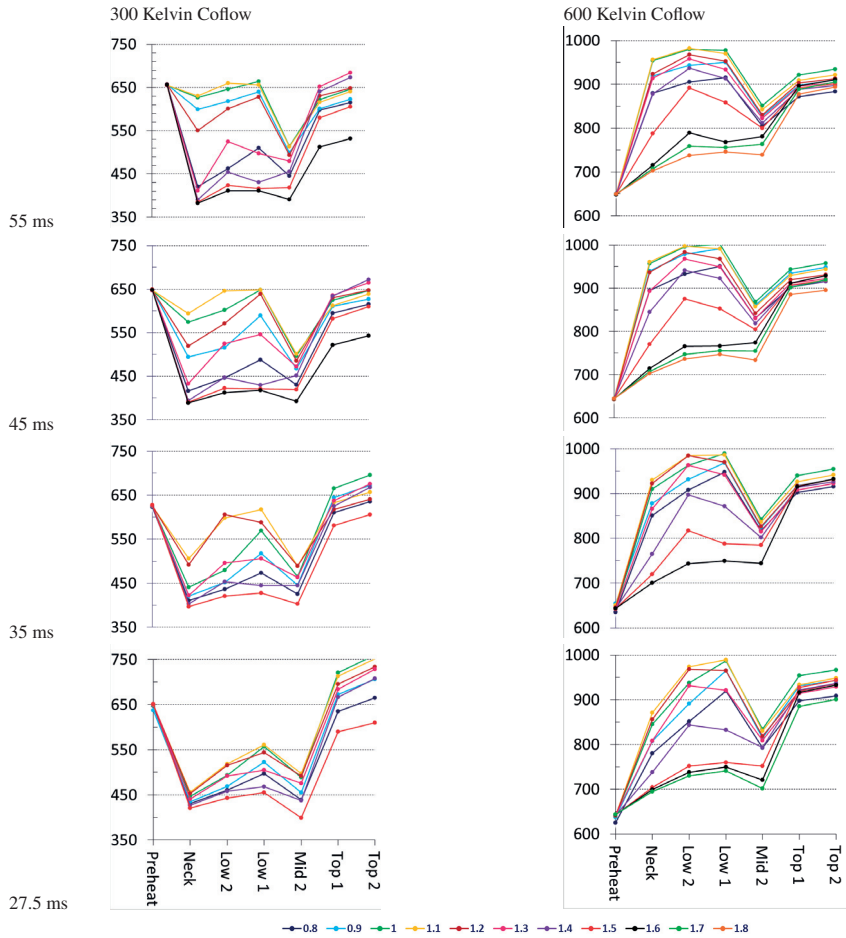
4

FIGURE 4: Average thermocouple values for four burner residence times. Left column shows unheated coflow tests while right column shows heated coflow test.

equivalence ratio increases, the temperature difference becomes slighter, eventually reversing at high equivalence ratios with Low 2 showing higher temperatures than Low 1. It would seem that higher equivalence ratios are able to penetrate closer to the wall at the upstream position, contrary to what would be expected from
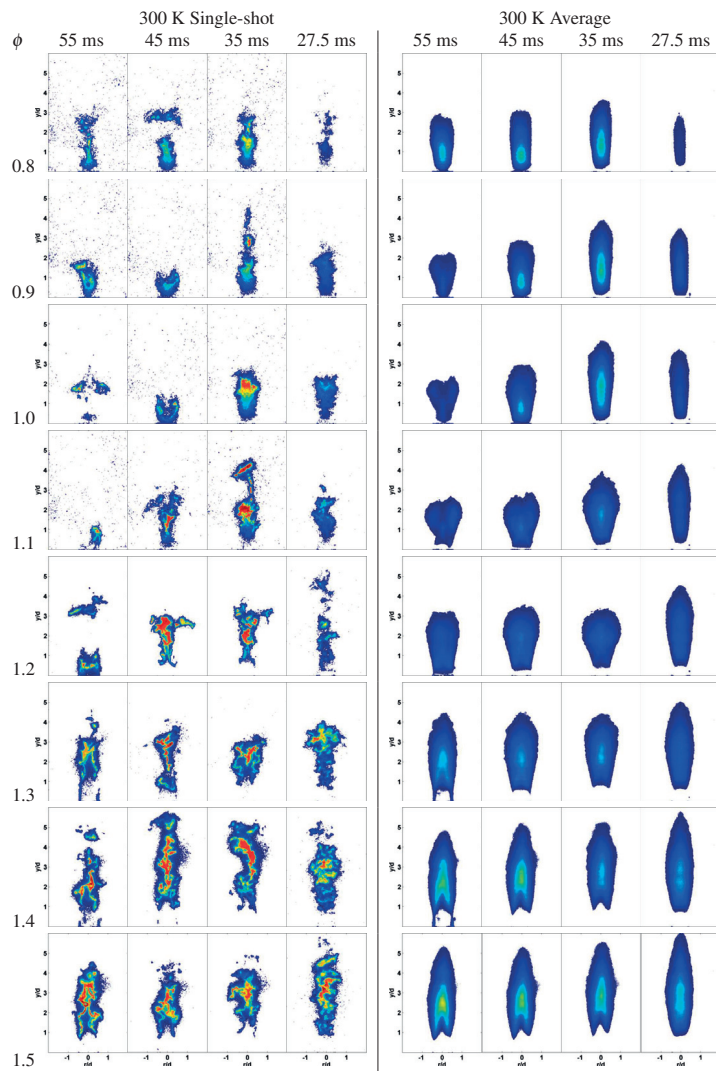
flame speeds or flame temperatures.

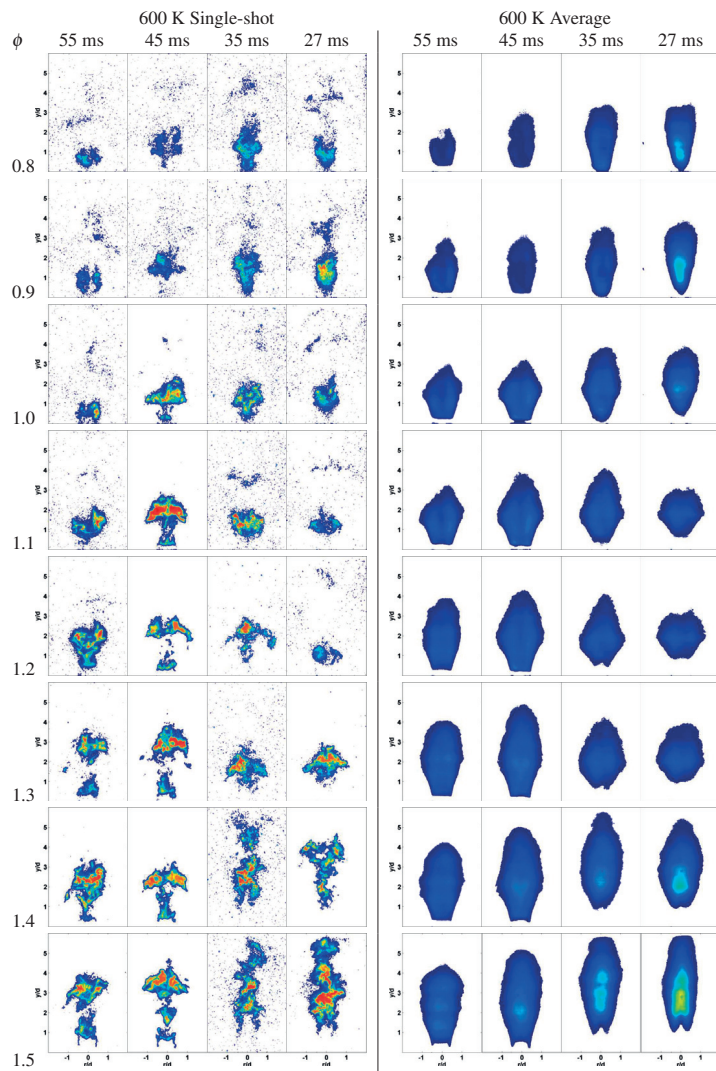**FIGURE 5**: Single shot and average images for non preheated coflow.

6

FIGURE 6: Single shot and average images for preheated coflow.

7

Imaging studies

Formaldehyde is a intermediate that is formed in the preheat region of the flame and it is one of the initial steps in fuel oxidation [13–15] Measurements of formaldehyde distribution were not included in this paper as the images did not contain significant data. For all conditions with equivalence ratio less than 1.5, there was no signal found for the formaldehyde molecule. Above ϕ= 1.5 signal was present, but at barely distinguishable levels. It is likely that any measurable formaldehyde, which is formed as the hydrocarbon fuels first begin to oxidize, is created and consumed inside the burner. By extension, this would suggest that the combustion that is seen outside of the burner is not largely methane.

OH-LIF images are a commonly used means of determining the post combustion regions in a flame [16]. Average images of OH-LIF are shown in figures 5 and 6 for various combinations of operating conditions alongside the single shot OH-LIF images for the same. While the average flame luminescence images are not shown, it was found that for lean equivalence ratios, 0.8 to 1.0 at both coflow temperatures and residence times, there is little or no visible flame luminescence outside of the burner. Once the flame luminescence becomes visible, it is similar in size and shape to the OH-LIF signal.

In a previous paper it was found that when burning methane at elevated pressure in this burner there were two OH-LIF conformations: attached diffuse and attached hollow [11]. The attached diffuse distribution was considered to be caused by fairly complete combustion inside the body of the burner which was evenly distributed in the burner exit gas. The attached hollow configuration was found under rich conditions where combustion from the center of the burner could not penetrate the cool wall regions leaving the outer edges with air and fuel that would combust once it was slowed and diluted outside the burner.

The 55ms, cool coflow OH-LIF images will be considered first. This set of experimental parameters were created from extrapolating values for residence time and coflow velocity from the elevated pressure experiments [11]. For this basis set, the attached diffuse shape can be seen at the equivalence ratio ϕ 0.8, and the hollow attached case appears at ϕ = 1.3 and richer. A third conformation can be seen which was not noticed in the previous elevated pressure test. The equivalence ratios from ϕ=0.9 to 1.2 show an expanding-cone OH signal distribution. During experiments at these equivalence ratios, combustion would fluctuate between quasi-stable positions indicated by a change in combustion signal, flame luminescence and temperature at the Top thermocouples. This fluctuation would occur over the course of a few minutes. From this it was conceived that combustion was occurring near the burner exit. Due to the proximity of the flame to the burner exit, combustion products rapidly expand causing the gases to "spray" out of the burner. Consulting the temperature traces, these equivalence ratios that exhibit the expanding cone distribution are seen to have high temperatures at all points along the burner.

Moving to the lower residence times exposes the burner walls to greater cooling which will cause some changes in the combustion inside the burner. As well, increased gas flow to the burner will change the mixing and fluid motion inside the burner. It can be seen that for the cold coflow conditions, decreasing the residence time changes the lower equivalence ratio onset of the expanding-cone shape, but not the the upper limit. That is, the transition from attached diffuse conformation to the expanding cone occurs at ϕ=1.0 for 45 ms residence time and ϕ = 1.1 for 35 ms residence time. In both these cases, the transition from expanding cone to attached hollow conformation occurs near ϕ=1.3. Later we will see that the heated coflow case does not follow this tendency, so the process must be related to the increased cooling flow, though it is not immediately clear why the transition between expanding-cone and attached-hollow conformations is unaffected. The 27.5 ms residence time, cool coflow images differ significantly from the other three cool coflow cases in that only the attached-diffuse appears. It is likely that the burner is operating in a much different way than the other cases due to the higher cooling effect of the coflow on the burner.

When the coflow is heated, there is a vastly reduced heat loss through the walls of the burner. This results in a shift of OH-LIF distributions as compared to the cool coflow experiments. The images become much more homogeneous with the expanding cone conformation dominating. The attached diffuse distribution is still found at lean equivalence ratios, all residence times exhibit it at ϕ=0.8 and 35 and 27.5 ms residence times show this at ϕ = 0.9 as well. The attached-hollow shape is only seen for equivalence ratios of ϕ=1.4 and above for the 35 ms and 27.5 ms residence time experiments. This heated coflow case is most like what will be encountered in a real world application. The wide range of operating points that yield similar OH-LIF distributions may indicate that the burner will have similar stabilizing characteristics for those points. Indeed, earlier studies found that changing this burner's equivalence ratio, when operated as a pilot/stabilizer for a larger burner, did not drastically alter the lean stability limit of the larger burner [17].

Conclusions

A burner was operated at a variety of equivalence ratios, residence times and two cooling temperatures in order to examine how the physical distribution of flame, OH-LIF, temperature and emission would respond. The goal of providing a thorough set of measurements with well known boundary conditions was achieved. Emissions measurements for CO and NOx were as expected in respect to equivalence ratio and temperature, with the caveat that combustion outside of the burner changed the rich condition response. This was further affected by the coflow temperature which allowed more complete combustion of the rich exhaust when diluted with the coflow. Temperature measure-

ments were useful in providing insight to the OH-LIF images when a cool coflow was present; however, in the heated coflow case the relationships were not so apparent. The OH-LIF shape showed three conformations of which one was dominant when moving to the heated coflow condition.

ACKNOWLEDGMENT

REFERENCES

[1] Apt, J., 2007. "The spectrum of power from wind turbines". *Journal of Power Sources,* **169**(2), pp. 369 – 374.

[2] Bayod-Rjula, A. A., 2009. "Future development of the electricity systems with distributed generation". *Energy,* **34**(3), pp. 377 – 383. WESC 2006 6th World Energy System Conference Advances in Energy Studies 5th workshop on Advances, Innovation and Visions in Energy and Energy-related Environmental and Socio-Economic Issues.

[3] Lynd, L. R., Larson, E., Greene, N., Laser, M., Sheehan, J., Dale, B. E., McLaughlin, S., and Wang, M., 2009. "The role of biomass in america's energy future: framing the analysis". *Biofuels, Bioproducts and Biorefining,* **3**(2), pp. 113–123.

[4] Lefebvre, A., 1998. *Gas Turbine Combustion, Second Edition*. Combustion: An International Series. Taylor & Francis.

[5] , 2010. "Directive 2010/75/eu of the european parliament and of the council of 24 november 2010 on industrial emissions". *Official Journal of the European Union*.

[6] Warnatz, J., Maas, U., and Dibble, R. W., 2006. "Formation of nitric oxides". In *Combustion*. Springer Berlin Heidelberg, pp. 259–270.

[7] Michaud, M. G., Westmoreland, P. R., and Feitelberg, A. S., 1992. "Chemical mechanisms of nox formation for gas turbine conditions". *Symposium (International) on Combustion,* **24**(1), pp. 879 – 887. Twenty-Fourth Symposium on Combustion.

[8] Zeldovich, Y. B., 1946. "The oxidation of nitrogen in combustion and explosions". *Acta Physiscochimica USSR,* **21**(4), pp. 577 – 628.

[9] Schildmacher, K.-U., Koch, R., and Bauer, H.-J., 2006. "Experimental characterization of premixed flame instabilities of a model gas turbine burner". *Flow, Turbulence and Combustion,* **76**(2), pp. 177–197.

[10] Sigfrid, I. R., Whiddon, R., Alden, M., and Klingmann, J., 2011. "Parametric study of emissions from low calorific value syn-gas combustion, with variation of fuel distribu-tion, in a prototype three sector burner". *ASME Conference Proceedings,* **GT2011**(45689), pp. 643–649.

[11] Whiddon, R., Sigfrid, I., Collin, R., and Klingmann, J., 2013. "Investigation of a premixed gas turbine combuston central body burner using oh planar laser induced fluorescence at elevated pressures.". *ASME Conference Proceedings,* **GT2013**(94443).

[12] Grosshans, H., Szasz, R., and Fuchs, L., 2010. "Sensitivity analysis of spray dispersion and mixing for varying fuel parameters". In 7th International Conference on Multiphase Flow - ICMF 2010 Proceedings, ICMF.

[13] Tolocka, M. P., and Miller, J. H., 1998. "Measurements of formaldehyde concentrations and formation rates in a methane-air, non-premixed flame and their implications for heat-release rate". *Symposium (International) on Combustion,* **27**(1), pp. 633 – 640. Twenty-Seventh Sysposium (International) on Combustion Volume One.

[14] Buerle, B., Hoffmann, F., Behrendt, F., and Warnatz, J., 1994. "Detection of hot spots in the end gas of an internal combustion engine using two-dimensional lif of formaldehyde.". *Symposium (International) on Combustion,* **25**(1), pp. 135 – 141. Twenty-Fifth Symposium (International) on Combustion.

[15] Bckle, S., Kazenwadel, J., Kunzelmann, T., Shin, D.-I., and Schulz, C., 2000. "Single-shot laser-induced fluorescence imaging of formaldehyde with xef excimer excitation". *Applied Physics B,* **70**(5), pp. 733–735.

[16] Suntz, R., Becker, H., Monkhouse, P., and Wolfrum, J., 1988. "Two-dimensional visualization of the flame front in an internal combustion engine by laser-induced fluorescence of oh radicals". *Applied Physics B,* **47**(4), pp. 287–293.

[17] Sigfrid, I. R., Whiddon, R., Alden, M., and Klingmann, J., 2011. "Experimental investigations of lean stability limits of a prototype syngas burner for low calorific value gases". *ASME Conference Proceedings,* **GT2011**(45694), pp. 651–658.

9